OPERANDO SYNCHROTRON X-RAY STUDIES OF ELECTROCHEMICAL ENERGY CONVERSION AND STORAGE SYSTEMS

A Dissertation

Presented to the Faculty of the Graduate School

of Cornell University

In Partial Fulfillment of the Requirements for the Degree of

Doctor of Philosophy

by

Xin Huang

Aug 2017

OPERANDO SYNCHROTRON X-RAY STUDIES OF ELECTROCHEMICAL ENERGY CONVERSION AND STORAGE SYSTEMS

Xin Huang, Ph. D.

Cornell University 2017

Developing clean energy alternatives to meet civilization's needs is one of the critical challenges facing humankind in the twenty first century. And, overcoming the limitations of current state-of-the-art energy conversion and storage systems is the central issue to solving the energy challenge. To advance the state-of-the-art, a complete understanding of the chemical reaction mechanisms and fundamental properties of the active materials in energy conversion and storage systems is required. *Operando* synchrotron X-ray techniques are ideally suited to characterize the structure of active materials under operating conditions on length scales ranging from atomic to macroscopic. This thesis consists of four projects in which two *operando* synchrotron X-ray techniques are applied to energy systems, revealing novel properties of the active materials under operating conditions. The two techniques are crystal truncation rod (CTR) analysis and X-ray imaging. The background of the techniques is introduced in Chapter 1. In Chapters 2 and 3, I applied *operando* CTR measurements to study the surface and bulk structures of the catalysts for photoelectrochemical cells ($SrTiO_3$) and fuel cells ($Pb_2Ru_2O_{6.5}$), respectively, under catalytically relevant conditions. In Chapters 4 and 5, *operando* X-ray imaging was applied to investigate the microstructure evolution in the two essential components in the "beyond lithium ion" batteries: sulfur cathode and lithium metal electrode. In Chapter 6, I summarize my work and provide a future outlook.

This thesis presents the following original contributions to scholarship:

1. Measure the atomic-scale surface structure of $SrTiO_3$ in an irreversible surface reconstruction driven by the applied potential. The reconstructed surface exhibits a three-fold increase in photocatalytic activity.
2. Develop a Fourier space fitting method to calculate the real space structure from CTR. Characterize the structure of $Pb_2Ru_2O_{6.5}$ thin film catalysts and the reversible surface reconstruction at applied potentials associated with the oxygen reduction reaction (ORR).
3. Observe the morphological evolution of sulfur particles in a sulfur electrode in Li-S batteries and characterize the growth and dissolution of lithium dendrites in a lithium symmetric cell during battery operation, and find the critical operating conditions (current density, electrolyte and temperature) that control the microstructure of the active material.

BIOGRAPHICAL SKETCH

Xin Huang was born in Jiamusi, Heilongjiang province in China. When he was 3 years old, he moved with his parents to Yantai, Shandong province, where they started their career from scratch. As a child, he witnessed the perseverance and hard work of his parents, which deeply influenced him, together with their Christianity faith. In 2006, he entered the University of Science and Technology of China, Hefei, China, and received the B.S. in 2010. From then on, he decided to move on "the road of science", and was admitted to the School of Applied and Engineering Physics in Cornell University for doctoral study. In Cornell, he joined Professor Joel Brock's research group and focused on the application of synchrotron X-ray techniques into electrochemical system. On his journey of science, he benefits a lot from the knowledge and the passion of his advisors and collaborators. Besides his role as a researcher, he enjoys the simple and fruitful life in Ithaca. He and his wife Moyao were married in 2015, and became parents of their son Jayden in 2016.

This dissertation is dedicated to my wife, Moyao, and my son, Jayden, for the greatest joy and hope they bring to my life.

ACKNOWLEDGMENTS

First of all, I would like to express my sincere gratitude to my supervisor Prof. Joel D. Brock for his encouragement, guidance and support through my Ph. D. study. It is his enthusiasm, his treasure-house of knowledge and his kindness that lead me through all my confusions and shape me from an "infant" to be a mature scientist. He also gave me a lot of freedoms to carry out my idea and find my own interest. Thank you for giving me such a wonderful opportunity to walk with you through this journey. I also want to thank Susan, Joel's wife, for her kindness in helping me and my wife to get used to the role of parents and treating us in their house. They are models for me and my wife to follow.

I owe a deep debt of gratitude to Prof. Héctor Abruña. I didn't imagine that I would have worked on electrochemistry before entering Cornell. But now I do enjoy this interesting field, and this could not happen without the help from Prof. Abruña. His knowledge in electrochemistry is beyond measurable. His enthusiasm and intuition to research is highly contagious.

I would like to thank the alumni and current members of Brock group for forming such an amazing research team, including Manuel Plaza, J. Y. Peter Ko, Yongsam Kim, Rohit Garg, Arthur Woll, Howard Joress and David Agyeman-Budu. Among them, I would like to show my special gratitude to Manuel. He leads me through my first research project, and gave me the first lesson to be a researcher. I also want to thank Prof. David Muller for being my committee member, and giving me very helpful advices. The applied solid state physics he taught is one of my favorite courses.

In Cornell, I also had the opportunity to know many outstanding collaborators and join many interesting projects. From projects to projects, I was continuously learning from them. Among them, there are Joaquin Rodríguez-López, Seung-Ho Yu, Hanjong

Paik, Prof. Darrell Schlom, Prof. Tomás Arias, Kendra Lechworth-Weaver, Nicole L. Ritzert, Yin Xiong, Ryo H. Wakabayashi, Celesta Chang and Megan Holtz. I would like to give special thanks to Seung-Ho for his patience to answer all my naive questions in electrochemistry and lead me into the battery studies.

I would like to thank my wife, Moyao. It is her love and kindness that turn our apartment to a sweet and warm home. She is my greatest supporter both in my family life and in my work.

Finally, I am very grateful for God's guidance and blessings throughout my Ph. D. life. Every accomplishment I ever achieved both in my research and in my personal life is from the abundant grace of God.

TABLE OF CONTENTS

LIST OF FIGURES

LIST OF TABLES

CHAPTER 1
INTRODUCTION

1.1 Motivation

When reading a sci-fi book, we frequently find some content about future energy sources that people use to power their technology, such as the famous matter-antimatter reaction in Star Trek. Although many of those ideas are not realistic (at least for now), it shows in awareness that energy is a critical issue that influences the advance of the society. To satisfy the increasing needs, explorations on inexpensive and environmental friendly materials for energy conversion and storage devices, such as fuel cells,[1-4] solar cells,[5,6] and batteries,[7-9] are popular. Although the chemical reactions involved in energy conversion and storage devices follow the basic principles of transporting and transferring electrons, holes or ions, the detailed mechanisms happening in the reactions are complex, and strongly related to the structure of active materials.[10,11] To reveal the link between the electrochemical properties and the structure of active materials, characterizing the structure under the working conditions (*operando*) is ideal.[12-14] However, this poses strict requirements for characterization probes. It should: (1) cause no interference with a material's functionality during the measurement and (2) be sensitive enough to provide structure information through the reaction environment at desired time and length scales. Synchrotron X-ray techniques reach these requirements and have become extensively used in electrochemical studies since the first application in 1983.[15,16]

However, the term "synchrotron X-ray techniques" covers many critical techniques, such as extended x-ray absorption fine structure (EXAFS), X-ray emission spectroscopy (XES), X-ray diffraction (XRD), X-ray reflectivity (XRR), and X-ray computed axial tomography (CAT). The goal of this thesis is not to cover all these

techniques, nor is it to give a complete review how these techniques have been applied to study energy materials. In this thesis, I introduce four projects as examples demonstrating how *operando* synchrotron X-ray techniques are applied to energy conversion and storage systems to study the structure of active materials at various scales. In chapter 1, I briefly introduce two X-ray techniques that were used in the projects: crystal truncation rod (CTR) measurements and X-ray microscopy (XRM) and how these techniques address certain energy systems. Chapter 2 discusses how *operando* CTR characterization of the surface structure of a photocatalyst ($SrTiO_3$) and how the reconstruction of the surface structure affects the photocatalytic activity. Chapter 3 uses *operando* CTR measurements to demonstrate a reversible structure reconstruction happening at the oxygen reduction reaction (ORR) condition in a metal oxide catalyst ($Pb_2Ru_2O_{6.5}$) for fuel cells. Chapter 4 uses *operando* X-ray microscopy (XRM) and XRD to study the phase change in the Li-S battery. Chapter 5 uses *operando* XRM to investigate lithium dendrite growth in the lithium metal electrode, showing how the operating condition of a battery influences the morphology. Chapter 6 is the summary and outlook of this thesis.

1.2 Synchrotron radiation

Synchrotrons, the circular accelerators where charged particles travel at relativistic speed in a curved path under a magnetic field, were first constructed for high energy physics experiments. For quite a period of time, synchrotron radiation was considered to be an undesired energy loss.[17] It was not until the pioneering work by Diran Tomboulian and Paul Hartman with the 300 MeV Cornell synchrotron, the predescessor of Cornell High Energy Synchrotron Source (CHESS), demonstrated the potential of synchrotron radiation using as X-ray source,[18] that synchrotron radiation

started to be considered as an X-ray source providing much higher brightness and tunable energy, areas where lab-based X-ray tubes could not compete. Following that trend, nowadays the primary application of most synchrotron facilities is as dedicated X-ray sources. Figure 1.1 compares the brilliance of X-rays from X-ray tubes, synchrotrons, and X-ray Free Electron Lasers.[19] Synchrotron produce more than 10^{10} times the spectral brightness of an X-ray tube, enabling a large number of X-ray experiments that simply could never be conducted using lab-based X-ray source. Next, we will introduce two synchrotron X-ray techniques, which are the main focus of this thesis.

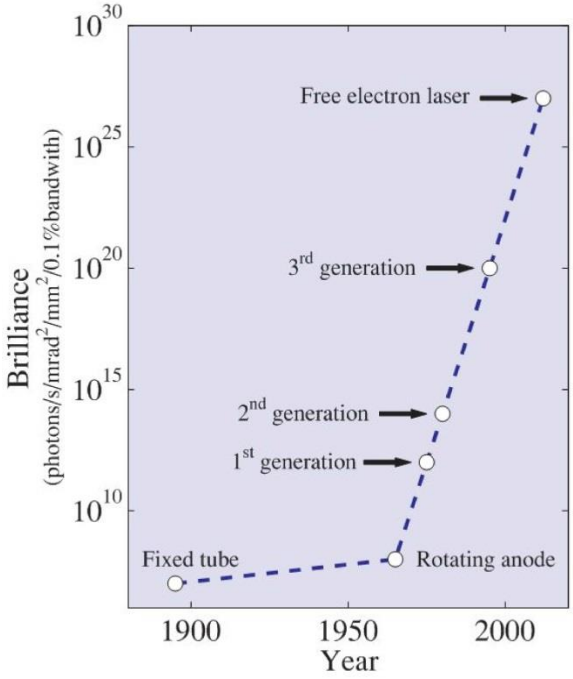

Figure 1.1. Spectral Brightness (Brilliance) of X-ray sources vs. time.[19]

1.3 Crystal truncation rod

1.3.1 Single crystal electrode

For practical applications, the ideal material for a catalyst should be in the form of a nanoparticle, because of the large surface area to volume ratio.[1] However, to fully understand the relationship between reaction mechanisms and the atomic-scale structure of nanoparticles is not straightforward, due to the variance in size and shape of individual nanoparticles, contributions from multiple surface planes, and defects.[20] Therefore, ever since the earliest wok in 1980s on high quality single crystal Pt electrodes,[21,22] the single crystal electrode has become one of most important experimental systems studied to understand the relationship between catalytic properties and atomic-scale structure.[23,24] With a single crystal, one can generate a perfectly flat electrode surface exposing only one low index plane, such as Pt (111).[25] Alternatively, one could also generate a high index plane surface ("miscut surface"), introducing and controlling the number of steps and kinks by the miscut angle, allowing the effects of steps and kinks on the catalytic activity to be investigated.[26,27] To build the relationship between activity and structure, characterizing the atomic structure of the single crystal electrode, both surface and bulk, is absolutely critical. Although the characterization could be carried out under *ex situ* conditions, this creates a question whether the structure of the catalyst under operating conditions is the same as at *ex situ* conditions, such as ultra-high vacuum. This is especially important for the structure at the interphase between the electrolyte and surface of the electrode in an electrochemical system. As a result, it is important to characterize the structure under *operando* conditions, which requires that the characterization methods should have high enough resolution to resolve the interphase structure at the single crystal electrode (less than 1 nm), and the ability to penetrate through the electrolyte.

1.3.2 Crystal truncation rod measurement

The XRD pattern of an ideal crystal (infinitely large) consists of a periodic array of sharp diffraction spots, the so called "Bragg peaks". However, when the infinite crystal is truncated to generate a flat surface, the XRD pattern changes. Rather than the sharp peaks, the width of "peaks" extends along the surface normal direction, turning into rods of scattering, the so-called crystal truncation rod (CTR). Figure 1.2 shows the reciprocal space map around the specular direction of a sample with a flat surface ($BaRuO_3/SrTiO_3(100)$). A rod of scattering (the specular 00L CTR) connecting Bragg peaks from (001) to (004) can be clearly seen. By measuring the intensity profile of the CTR, one characterizes the average surface structure of the crystal with high resolution (sub-Angstrom). CTR measurements are well-matched to the requirements posed earlier for *operando* structural characterization of single crystal electrodes: 1. The CTR signal is sensitive to sub-Angstrom structure changes; 2. CTR measurements can be conducted using high energy X-rays, which decreases absorption in the electrolyte. Figure 1.3 shows the attenuation length (the intensity of X-ray decreases by $1/e$ at this length) of X-rays in water as a function of X-ray energy. Thus, CTR measurements are a powerful tool to study the structure of single crystal electrodes in *operando* conditions[28].

Now we will briefly review the basic theory for the CTR and provide the background information that is essential for the derivation of the formulae. The reader should refer to the references[19,29] for a more comprehensive discussion on X-ray diffraction theory.

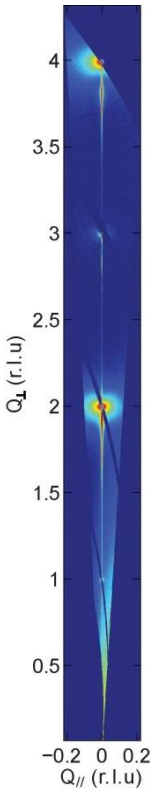

Figure 1.2. Reciprocal space map of a $BaRuO_3$ thin film grown on a $SrTiO_3$ (100) substrate.

In scattering, the important parameter to quantify the scattering amplitude is the scattering length. For a free electron, the X-ray scattering length is $r_0 = \frac{e^2}{4\pi\varepsilon mc^2} = 2.82 \times 10^{-5}$Å. r_0 is referred as the Thomson scattering length, which is also considered as the classical radius of an electron. Since the fundamental element for X-ray scattering from material is the electron (because the mass of proton is about 1800 times larger than that of electron, the scattering length is inversely proportional to the mass.), the most frequently and convenient used term is the scattering length normalized by Thomson scattering length, which is referred as the form factor (F). Under this definition, the form factor for a free electron is one. Secondly, we work in the kinematic approximation, assuming that X-ray is only scattered once (the scattered

X-ray is not scattered again in the material). This approximation is based on the fact that X-ray interacts with materials weakly (r_0 is only the order of 10^{-5}Å). However, the approximation will break down in the Bragg condition.

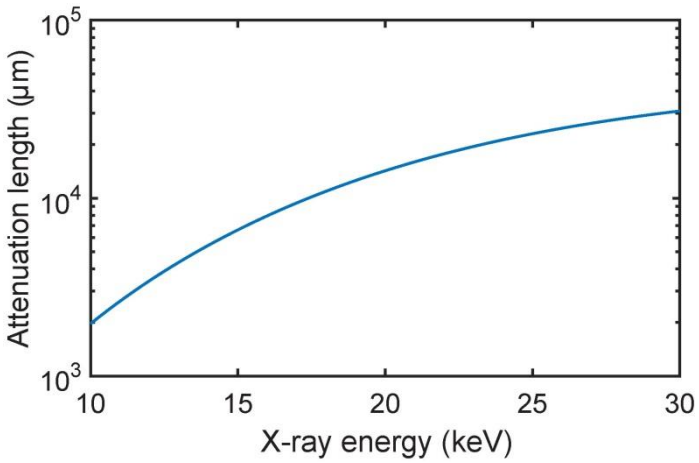

Figure 1.3. The attenuation length of X-rays in water as a function of photon energy.

In the kinematic approximation, the form factor is simply the Fourier transform of the electron density.[19] This is true when the energy of the X-ray is far away from any intrinsic energy level of the material (otherwise, a dispersion correction is necessary).

Since the form factor is the Fourier transform of the electron density, it will be helpful to know that the Fourier transform of the convolution operation between two functions becomes the products of the two Fourier transforms of the functions. The crystal structure could be subdivided into basis and lattice. The basis is a pattern of atoms. The lattice is the framework of points where the basis is periodically placed. From mathematic view, this could be treated as the convolution of the basis and the lattice. For simplification, Figure 1.4 shows, in one dimension, how the electron density of a crystal can be obtained by convolving the basis and the lattice: $\rho_{cr}(z) = \rho_{uc}(z) * S_{lattice}(z)$. Thus, the form factor of the crystal can be expressed as the multiplication of the form factor of the unit cell and the Fourier transform of lattice

function: $F_{cr}(Q) = F_{uc}(Q) \times \mathcal{F}(S_{lattice}(z))$. The lattice function is summation of a series of Delta functions: $S_{lattice}(z) = \sum_{n=1}^{N} \delta(z - na)$. After Fourier transform, the lattice function becomes:

$$\mathcal{F}(S_{lattice}) = \sum_{n=1}^{N} exp(inQa) = exp(i\frac{(N-1)Qa}{2})\frac{sin(\frac{NQa}{2})}{sin(\frac{Qa}{2})}$$

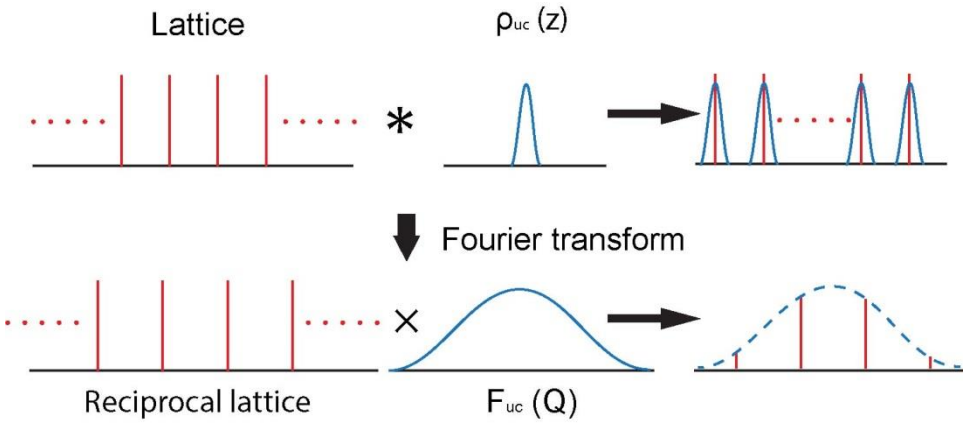

Figure 1.4. Illustration of the relationship between the electron density in real space and the form factor in reciprocal space for an infinitely large single crystal.

The function of $|\mathcal{F}(S_{lattice})|$ will get peaks, when $Q = 2\pi/a$. The peak value equals to N, and the full width at half maximum of peak is approximately $1/N$. With N becomes significantly large, $|\mathcal{F}(S_{lattice})|$ is ended up to become a summation of a series of Delta functions, $\sum_n \delta(Q - n2\pi/a)$, which is similar to the lattice sum and brings up the conception of reciprocal lattice.

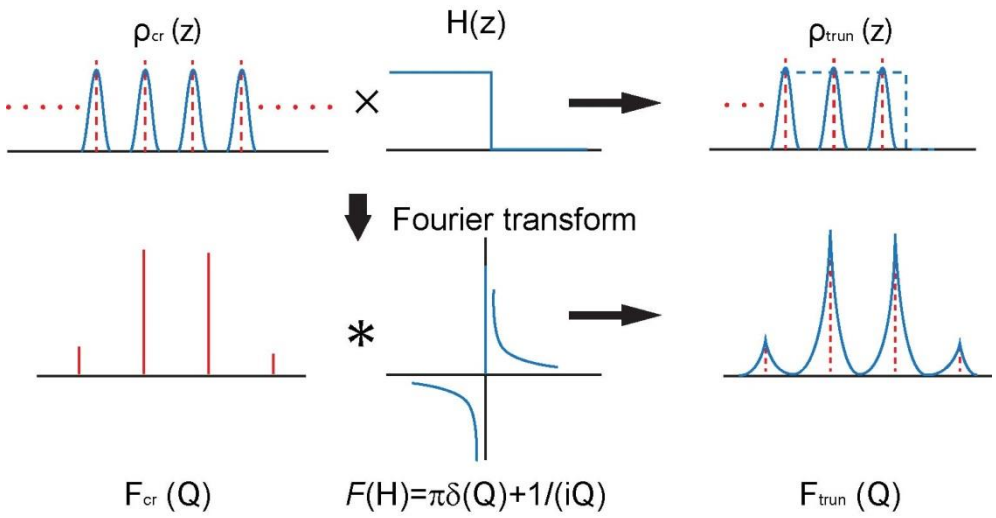

Figure 1.5. The electron density and form factor for truncated single crystal

Now imagine that the infinite crystal is cleaved to form a flat surface. Mathematically, the truncated sample can be considered to be the convolution of an infinite crystal with a step function: $\rho_{trun}(z) = \rho_{cr}(z) \times H(z)$. After Fourier transform, the $F_{trun}(Q) = F_{cr}(Q) * \mathcal{F}(H(z))$. The Fourier transform of the step function $H(z)$ is: $\mathcal{F}(H(z)) = \pi\delta(Q) + 1/(iQ)$. As shown in Figure 1.5, the result of the convolution between $F_{cr}(Q)$ and $\mathcal{F}(H)$ is the expansion of the width of the Bragg peak along the surface normal direction, forming a rod, as mentioned earlier in Figure 1.2. Another frequently used way to calculate $F_{trun}(Q)$ is to modify the summation of lattice by adding the absorption coefficient β:

$$\mathcal{F}(S_{lattice}) = \sum_{n=1}^{\infty} e^{inQa} e^{-n\beta} = \frac{1}{1 - e^{iQa} e^{-\beta}}$$

Then we could obtain the form factor of truncated crystal:

$$F_{trun}(Q) = F_{uc}(Q) \times \mathcal{F}(S_{lattice})$$

Now let us add complexity into the system by allowing the topmost structure to be different from the rest of the layers (for example, surface reconstruction). The electron

density and the position for the topmost unit cell is $\rho_{sur}(z)$ and a_1, then the electron density of this model could be written as:

$$\rho_{tot}(z) = \rho_{trun}(z) + \rho_{sur}(z - a_1)$$

After Fourier transform, the form factor of the model becomes:

$$F_{tot}(Q) = F_{trun}(Q) + f_{sur}(Q)\exp(iQa_1)$$

To demonstrate the sensitivity of CTR the surface structure change, we model the CTR from graphite, and allow the topmost atomic layer to have 3% lattice expansion /compression. The corresponding CTR profiles are shown in Figure 1.6.

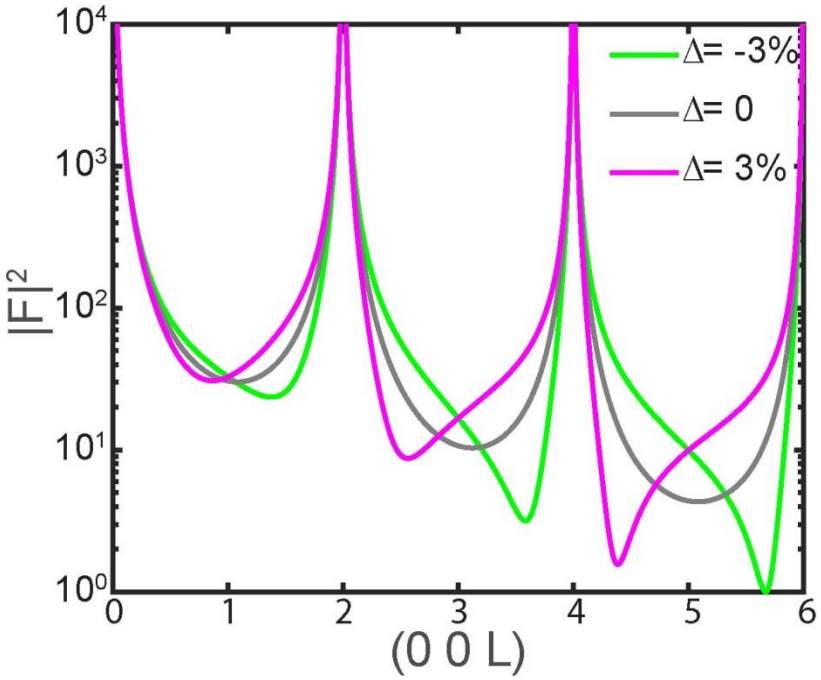

Figure 1.6. Simulated CTR from graphite, allowing the first layer to have ± 3% interplanar distance change.

1.3.3 Measure the CTR

CTR measurements are typically conducted in two ways. One way is to fix the X-ray incident angle at a very small angle (below the critical angle), and rotate the sample around the surface normal direction[30,31]. The second way uses the same experimental setup with an X-ray reflectivity (XRR) measurement, and collect over large Q range (So it is also referred as high-resolution X-ray reflectivity). In our experiments, we use the second geometry. For X-ray intensity collection, we used a large area detector (41cm × 41cm General Electric area detector, DXR250RT, GE Inspection Technologies). Each pixel is 200 μm × 200 μm. The advantages of using this detector is that it is optimized for high energy x-rays and it's large size enabled us to measure multiple CTRs simultaneously. Figure 1.7a shows how several CTRs are measured simultaneously. The (00L) (specular) and (10L) (off-specular) CTRs are shown in the diagram. The intersection of a CTR with the Ewald sphere produces a small spot on the detector. Small regions of interest on the detector containing the CTR signals are selected: ROI_1 (for (00L) CTR) and ROI_2 (for (10L) CTR), as an example. Figure 1.7b shows one of the ROI_1 images, containing the (00L) CTR spot when L=1.75. The ROI_1 image was separated into two regions. Region 1 was used to calculate the integrated intensity of the reflected signal: I_{sig} while region 2 was used to calculate the scattering background per pixel: i_{back}. Then the integrated intensity of the CTR is given by: $I_{ctr} = \left(I_{sig} - i_{back}N_{sig}\right)C_{norm}$, where N_{sig} is the number of pixels in region 1. C_{norm} is a normalization term containing the attenuation of the solution, and the efficiency of GE area detector at 30 keV. Considering the divergence of the beam, the intensity is written as $I_0 = \int i_0 d\theta_{div}$, where $i_0$is the distribution of x-ray intensity in angular space. Then the conversion between I_{sig} and $|F|^2$ is expressed as:

$$I_{CTR} = \int \lambda^2 i_0 {r_0}^2 P|F|^2 Q_z dQ_z/[(Q_z A_{uc})^2 cos\,\theta]]$$

Where $dQ_z = 2k\cos\theta d\theta_{div}$.

λ is the wavelength of the X-ray, A_{uc} is the surface area of the unit cell, P is the polarization term, Q_z is the scattering vector along the surface normal and θ is the incident angle. The integral is taken over the angular divergence range. Since all the terms except i_0 vary little within the angular divergence of beam ($\sim 10^{-3}$), those terms can be taken out of the integral, so that the equation becomes:

$$|F|^2 = \frac{I_{CTR} {A_{uc}}^2 sin\theta}{\lambda^2 I_0 {r_0}^2 P}$$

The 10L CTRs, before and after an electrochemical training (discuss later in Chapter 2), are shown in Figure 1.7c, whereas the 00L CTRs are shown later in Figure 2.2a in Chapter 2.

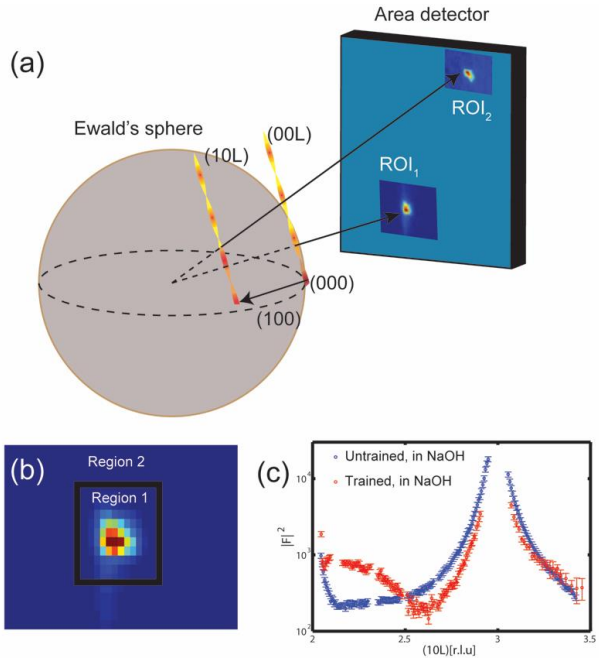

Figure 1.7. (a) Schematic diagram showing how multiple CTRs are measured simultaneously with the large area detector. (b) Diffraction image of (00L) CTR spot.

L value for this particular CTR spot is 1.75. (c) $|F|^2$ vs. (10L) for STO before and after an electrochemical training.

1.3.4 CTR interpretation

There are several methods to calculate the potential real space structure from CTR. Here we mainly introduce the three methods we applied in our projects, while the other methods could be found the reference[30]:

Model fitting: Among methods to obtain the real space structure from the experimental $|F|^2$, the earliest method is model fitting. The CTR data are fitted to an atomic model by non–linear least square fitting. The atomic positions, Debye-Waller factors, and site occupancy were all relaxed. The reduced chi squared (χ^2) was used as the goodness of fit parameter: $\chi^2 = \frac{1}{N-n-1}\sum_{i=1}^{N}\frac{(y_i - f(x_i))^2}{\sigma_i^2}$. Here, N is the total number of data points; n is the number of adjustable parameters; σ_i is the experimental error at x_i, mainly from the stochastic noise; y_i is the measured experimental data at x_i; and, $f(x_i)$ is the calculated value at x_i.

JDFT guided model fitting: Although the model fitting method could provide a good suggestion for the surface structure, the structure we obtain is usually not unique, and is not guaranteed to be favored in terms of the free energy. Here, we applied Joint Density Functional Theory calculations, which calculate and minimize the free energy of a quantum-mechanical system in contact with a liquid environment, ensure that the fitted surface structure is physically realizable. However, JDFT by itself could not consider the thermal disorder, partial occupancy or other disorder in the system. We applied the JDFT guided model fitting procedure by allowing the atoms to move away from their JDFT minimum energy positions to consider the effect of non-equilibrium

processes and the resulting partial occupancies and Debye-Waller factors account for defects and disorder. We may ensure the physicality of these fits by minimizing a residual R^2 which includes both $\chi^2$and a penalty function to prevent the fit positions $\{\zeta_I\}$ from varying significantly from the JDFT predicted positions $\{z_i\}$

$$R^2 = \chi^2 + \frac{1}{2}\gamma \sum_{i=1} (\zeta_i - z_i)^2.$$

The constant γ determines the relative weight of the penalty function compared to χ^2. The structure factor for this fit is calculated from tabulated form factors for the explicit atoms located at fit positions $\{\zeta_I\}$ and the electron density from JDFT.

Fourier space fitting: One limitation of both model fitting and JDFT guided model fitting (in fact it is true for most CTR analysis methods, such as COBRA) is that they could not effectively calculate the structure for a more complicated system. For example, in Chapter 3, we will collect the CTR for the sample of 10 nm $Pb_2Ru_2O_{6.5}$ grown on $Sm_2Ti_2O_7$ (111), containing 17.5 unit cells, and every unit cell contains 84 atoms. Although the crystal quality of $Pb_2Ru_2O_{6.5}$ is good, it still contains more disordering than that in the bulk structure. It is impossible to free every parameter for model fitting or JDFT calculation. The situation leads to the solution of the Fourier space fitting. In Fourier space fitting, rather than relaxing certain the atom in the starting model, we add a function to the calculated form factor of the starting model:

$$f(Q) = A_p \times exp(-\frac{\left(Q - Q_p\right)^2}{2{\sigma_p}^2}) \times \exp(i(B_p Q + C_p))$$

$f(Q)$ contains the magnitude of Gaussian function and a linear phase. By changing σ_p, A_p, B_p and C_p, it affects the form factor locally around Q_p. Then conduct the Fourier transform of the form factor to obtain the real space structure, and apply the "physical constrains", setting the negative electron density to zero, and set the electron value outside the film region to zero. By changing the relaxing parameters and applying the "physical constrains", we could obtain the best fitting structure. Repeat this procedure for the other Q_p, we could eventually obtain a real space structure that agree with the CTR data.

1.4 X-ray imaging

1.4.1 The microstructure changes in electrochemical system

In the previous section, we have discussed about the X-ray method that could be applied to measure the surface structure of the single crystal electrode. The length scale of the measurement is usually within nanometer (a few atomic layers). However, the structure change could happen in a much larger scale, such as micrometers[32]. The influence of the microstructure changes to the performance of the catalyst is as critical as, in many cases more strongly than, nanostructural changes. For example, in the anode materials for lithium-ion batteries, silicon has shown highest theoretical gravimetric capacity (4200 mA h/g), more than 10 times than the graphite (372 mA h/g), which is the state-of-art anode material.[33,34] However, the high performance of Si comes together with strong limitations. The volume of silicon expands about 400% during lithiation. By continuous cycling, the significant volume change poses a strong strain in the materials and forms cracks and void space in the bulk silicon particles, as shown in Figure 1.8.[33,35] This process finally leads to a rapid capacity fade in battery tests. To observe morphology evolution and understand the kinetics of crack forming

during the battery operating, observing the structure change in nanoscale is not enough. For situations like this, an *operando* method with the resolution of microns is strongly needed.

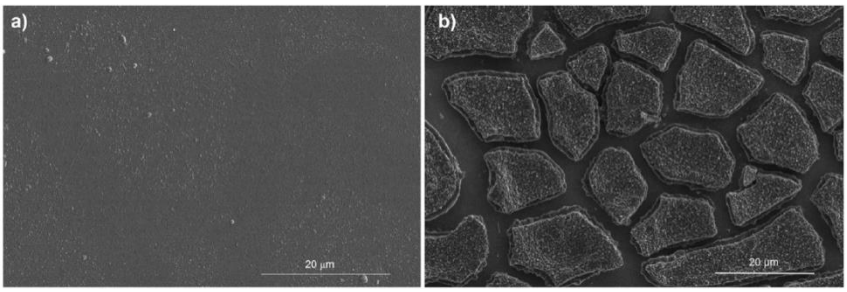

Figure 1.8. *Ex situ* SEM image of a silicon film (a) before battery test and (b) after battery test (5 cycles).[35]

1.4.2 Transmission X-ray imaging

Transmission X-ray imaging is the earliest application of X-rays, since they were discovered in 1895. Nowadays transmission X-ray imaging and the associated X-ray 3D-imaging technique, computed tomography, are widely used in medical studies. With synchrotron X-ray sources, X-ray imaging can reach higher resolution, ranging from microns to several nanometers (with the help of X-ray optics), and requires much shorter exposure time, which makes X-ray imaging a powerful method for *operando* studies of microstructure changes in energy conversion and storage devices[36].

Transmission X-ray imaging is related to two factors: the absorption and refraction of X-ray. How absorption affects imaging is easier to understand. Assume an X-ray

propagates along the z-axis and illuminates an inhomogeneous object. The intensity of transmitted X-ray can be expressed as:

$$I(x,y) = I_0 exp(-\int \mu(x,y,z)dz)$$

I_0 is the incident X-ray intensity and $\mu(x,y,z)$ is the absorption coefficient of the object. By measuring $I(x,y)$, we can obtain the line integral of the absorption coefficient over the X-ray propagation direction.

$$\int \mu(x,y,z)dz = \log(\mathrm{I}_0/\mathrm{I}(\mathrm{x},\mathrm{y}))$$

The absorption coefficient μ reflects photoelectric absorption, and is directly related to the atomic number of the material (proportional to Z^4).

1.4.3 Phase enhanced X-ray imaging

Transmitted X-ray intensity is also related to the refraction of X-rays, not just absorption. The refraction index could be written as: $n = (1-\delta) + i\beta$. β is associated with the absorption coefficient by $\beta = \mu/2k$, whereas δ is related with the classical refraction. The transmission of X-ray amplitude could be rewritten as:

$$E(x,y) = E_0 exp(i\int n(x,y,z)kdz)$$

$$E(x,y) = E_0 exp(ikz) exp(i\int \delta(x,y,z)dz) exp(-\int \beta(x,y,z)dz)$$

The value of δ is typically more than 1000 times stronger than that of β in low Z materials. Figure 1.9 compares the value of δ and β in water[19]. Although X-ray absorption is sufficient to distinguish between objects with large Z difference, like bones versus soft tissues, it is difficult to distinguish between objects that only contain

low Z elements. It brings up the question whether we could make use of the refraction of X-ray to obtain much higher sensitivity than with just absorption contrast.

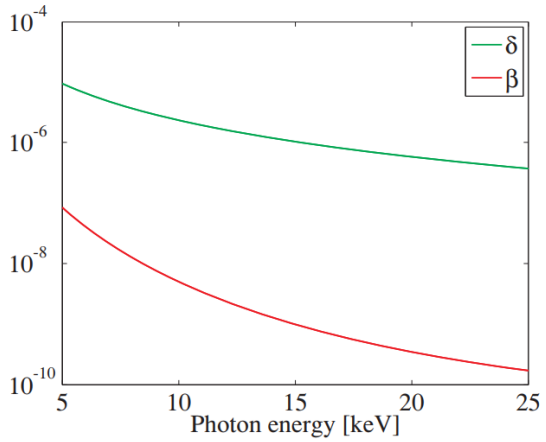

Figure 1.9. The energy dependence of δ and β for water.[19]

To answer this question, it is interesting to first talk about a phenomenon that could be found with a visible light source (collimated and monochromated, such as a laser). We observed the emitted beam with a screen. When an object with a sharp edge (such as a blade) cuts partially the beam in its path, we observe a series of interference fringes parallel to the edges showing up at the position where the beam is cut on the screen. This phenomenon is called Fresnel edge diffraction. In transmission X-ray imaging, the same phenomenon occurs and interference fringes can be observed at the edge of the projection of object on a detector. For the purpose of imaging an object, we should optimize these fringes: both clearly observe the first fringe that enhance the contrast around the edge of the object and still maintain the detailed feature of the shape of object. These two requirements can be satisfied by simply adjusting the distance between object and detector in the Fresnel region: $D \sim a^2/\lambda$, where a is the scale of the feature we need to resolve and λ is the wavelength of X-ray. Figure 1.10 shows clearly the effect of the distance to the resolution of the object. This edge enhancement was referred as phase contrast.

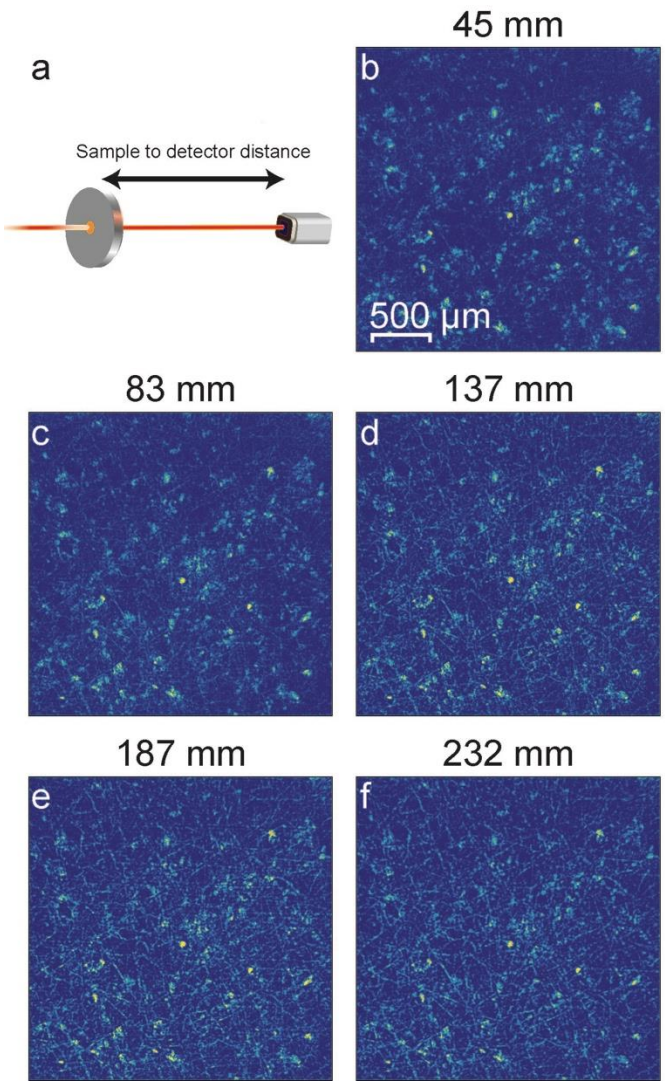

Figure 1.10. X-ray image of sulfur electrode at different distances between the sample and detector.

The refraction and absorption of the object change the phase and magnitude of the transmitted X-ray, so that the wavefield is deformed from a planar wavefield. By calculating the wavefield at the position of detector, we can simulate the intensity of both absorption contrast and phase contrast. Now consider a monochromatic beam propagating along z direction. At $z = 0$, the beam penetrates an object, and the wavefield at $z = 0$ is $\psi_0(x, y)$. We calculate the wavefield after propagating to the

detector at position z. Since it is easier to calculate the propagation in Fourier space, we conduct Fourier transform on $\psi_0(x, y)$.

$$\phi_0(k_x, k_y) = \int \psi_0(x, y) exp(ik_x x + ik_y y) dx dy$$

The wavefield at z could be expressed as:

$$\phi_z(k_x, k_y) = exp(ik_z z)\phi_0(k_x, k_y)$$

Where k_z is the component of k along z direction. k_z could be expressed as $k_z = \sqrt{k^2 - {k_x}^2 - {k_y}^2}$. Considering k_z is along the wave propagation direction, $k_z \gg k_x$ or k_y, k_z could be approximated as:

$$k_z = k - {k_x}^2/2k - {k_y}^2/2k$$

Then, we obtain $\phi_z(k_x, k_y)$ as:

$$\phi_z(k_x, k_y) = exp(ikz) exp(-ik_x z/(2k)) exp(-ik_y z/(2k)) \phi_0(k_x, k_y)$$

By inverse Fourier transform, we obtain the wavefield at z:

$$\psi_z(x, y) = \frac{1}{4\pi^2} \int \phi_z(k_x, k_y) \exp(-ik_x x - ik_y y)\, dk_x dk_x$$

$$= \frac{\exp(ikz)}{4\pi^2} \int \exp\left(-\frac{ik_x z}{2k}\right) \exp\left(-\frac{ik_y z}{2k}\right) \phi_0(k_x, k_y) \exp(-ik_x x - ik_y y) dk_x dk_x$$

With this method, we can calculate how the wavefront changes with the distance between object and detector. Here, we offer an example. We define an object that both absorbs and refracts X-rays, which changes both the magnitude and phase of $\psi_0(x, y)$. The images at multiple distances are shown in Figure 1.11.

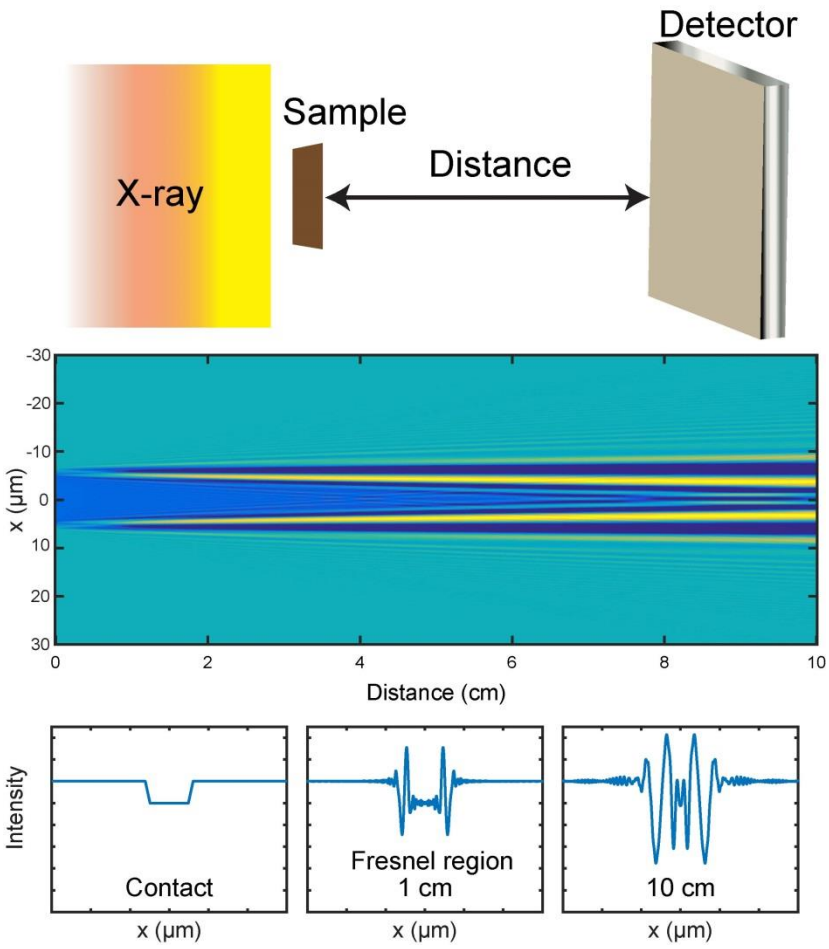

Figure 1.11. Simulated X-ray intensity changing with the distance between sample and detector.

1.4.4 Computed tomography

One of the main restrictions of the imaging in the transmission geometry is that we obtain the projection of a 3-dimensional structure of the object onto 2-dimensional plane. However, computed tomography (CT) overcomes this restriction by collecting the projections over a large angle range. In this way, the 3-dimensional structure could be constructed.

To understand how the CT works, it is important to introduce the Fourier slice theorem. $p(x, y)$ is the projection of $f(x, y, z)$ at xy plane.

$$p(x, y) = \int f(x, y, z)dz$$

The Fourier transform of $p(x, y)$ is:

$$P(k_x, k_y) = \int f(x, y, z)exp(ik_x x)exp(ik_y y)dxdydz$$

Next, we compare this with the Fourier transform of $f(x, y, z)$:

$$\mathcal{F}(k_x, k_y, k_z) = \int f(x, y, z)\exp(ik_x x)\exp(ik_y y)\exp(ik_z z)dxdydz$$

We could conclude that

$$\mathrm{P}(k_x, k_y) = \mathcal{F}(k_x, k_y, 0)$$

The Fourier transform of a projection of function along a direction is equal to the slice of Fourier transform of the function on the plane containing the origin and perpendicular to that direction. Thus, in CT, the projections from different angle are collected and Fourier transformed. In the Fourier space, the three-dimensional structure of the object could be constructed based on the slices at different angles, and then the reconstructed structure is inverse Fourier transformed to get the structure of the object in the real space.

REFERENCES

1 Arico, A. S., Bruce, P., Scrosati, B., Tarascon, J. M. & Van Schalkwijk, W. Nanostructured Materials for Advanced Energy Cnversion and Storage Devices. *Nat. Mater*. **4**, 366-377, (2005).

2 Debe, M. K. Electrocatalyst Approaches and Challenges for Automotive Fuel Cells. *Nature* **486**, 43-51, (2012).

3 Steele, B. C. & Heinzel, A. Materials for Fuel-Cell Technologies. *Nature* **414**, 345-352, (2001).

4 Dai, L. M., Xue, Y. H., Qu, L. T., Choi, H. J. & Baek, J. B. Metal-Free Catalysts for Oxygen Reduction Reaction. *Chem. Rev.* **115**, 4823-4892, (2015).

5 Ma, Y. *et al.* Titanium Dioxide-Based Nanomaterials for Photocatalytic Fuel Generations. *Chem. Rev.* **114**, 9987-10043, (2014).

6 Yang, J. H., Wang, D. G., Han, H. X. & Li, C. Roles of Cocatalysts in Photocatalysis and Photoelectrocatalysis. *Acc. Chem. Res.* **46**, 1900-1909, (2013).

7 Etacheri, V., Marom, R., Elazari, R., Salitra, G. & Aurbach, D. Challenges in the Development of Advanced Li-ion Batteries: a Review. *Energy Environ. Sci.* **4**, 3243-3262, (2011).

8 Dunn, B., Kamath, H. & Tarascon, J. M. Electrical Energy Storage for the Grid: A Battery of Choices. *Science* **334**, 928-935, (2011).

9 Tarascon, J. M. & Armand, M. Issues and Challenges Facing Rechargeable Lithium Batteries. *Nature* **414**, 359-367, (2001).

10 Parvulescu, V. I. & Kemnitz, E. *New Materials for Catalytic Applications*. (Elsevier Science, 2016).

11 Park, J. Y. *Current Trends of Surface Science and Catalysis*. (Springer New York, 2013).

12 Tada, M. *et al.* In Situ Time-Resolved Dynamic Surface Events on the Pt/C Cathode in a Fuel Cell under Operando Conditions. *Angew. Chem. Int. Ed.* **46**, 4310-4315, (2007).

13 Gu, M. *et al.* Demonstration of an Electrochemical Liquid Cell for Operando Transmission Electron Microscopy Observation of the Lithiation/Delithiation Behavior of Si Nanowire Battery Anodes. *Nano Letters* **13**, 6106-6112, (2013).

14 Leriche, J. B. *et al.* An Electrochemical Cell for Operando Study of Lithium Batteries Using Synchrotron Radiation. *J. Electrochem. Soc.* **157**, A606-A610, (2010).

15 Hoffman, R. W. Study of Passivity of Iron By in situ Methods: Mossbauer and Exafs, in *Passivity of Metals and Semiconductors* 147-162 (Elsevier, 1983).

16 Kruger, J., Long, G. G., Kuriyama, M. & Goldman, A. I. Structural Studies of Passive Films Using Surface, in *Passivity of Metals and Semiconductors* 163-168 (Elsevier, 1983).

17 Elder, F. R., Langmuir, R. V. & Pollock, H. C. Radiation from Electrons Accelerated in a Synchrotron. *Phys. Rev.* **74**, 52-56, (1948).

18 Tomboulian, D. H. & Hartman, P. L. Spectral and Angular Distribution of Ultraviolet Radiation from the 300-Mev Cornell Synchrotron. *Phys. Rev.* **102**, 1423-1447, (1956).

19 Als-Nielsen, J. & McMorrow, D. *Elements of Modern X-ray Physics*. (Wiley, 2011).

20 O'Mullane, A. P. From Single Crystal Surfaces to Single Atoms: Investigating Active Sites in Electrocatalysis. *Nanoscale* **6**, 4012-4026, (2014).

21 Clavilier, J. Role of Anion on the Electrochemical-Behavior of a (111) Platinum Surface - Unusual Splitting of the Voltammogram in the Hydrogen Region. *J. Electroanal. Chem.* **107**, 211-216, (1980).

22 Clavilier, J., Faure, R., Guinet, G. & Durand, R. Preparation of Monocrystalline Pt Microelectrodes and Electrochemical Study of the Plane Surfaces Cut in the Direction Oof the {111} And {110} Planes. *J. Electroanal. Chem. Interfacial Electrochem.* **107**, 205-209, (1980).

23 Markovic, N. M., Schmidt, T. J., Stamenkovic, V. & Ross, P. N. Oxygen Reduction Reaction on Pt and Pt Bimetallic Surfaces: A Selective Review. *Fuel Cells* **1**, 105-116, (2001).

24 Katsounaros, I., Cherevko, S., Zeradjanin, A. R. & Mayrhofer, K. J. J. Oxygen Electrochemistry as a Cornerstone for Sustainable Energy Conversion. *Angew. Chem.-Int. Edit.* **53**, 102-121, (2014).

25 Herrero, E., Franaszczuk, K. & Wieckowski, A. Electrochemistry of Methanol at Low-Index Crystal Planes of Platinum - an Integrated Voltammetric and Chronoamperometric Study. *J. Phys. Chem.* **98**, 5074-5083, (1994).

26 Korzeniewski, C., Climent, V. & Feliu, J. Electrochemistry at Platinum Single Crystal Electrodes, in *Electroanalytical Chemistry Electroanalytical Chemistry: A Series of Advances* 75-170 (CRC Press, 2011).

27 Gomez-Marin, A. M., Rizo, R. & Feliu, J. M. Some Reflections on the Understanding of the Oxygen Reduction Reaction at Pt(111). *Beilstein Journal of Nanotechnology* **4**, 956-967, (2013).

28 Robinson, I. K. & Tweet, D. J. Surface X-ray Diffraction. *Rep. Prog. Phys.* **55**, 599, (1992).

29 Warren, B. E. *X-Ray Diffraction*. (Dover Publications, 2012).

30 Schlepütz, C. M. *Systematic Structure Investigation of YBCO Thin Films with Direct Methods and Surface X-ray Diffraction* Ph.D. thesis, University of Zurich, (2009).

31 Plaza, M. *et al.* Structure of the Photo-catalytically Active Surface of SrTiO3. *J. Am. Chem. Soc.* **138**, 7816-7819, (2016).

32 Braun, A. *X-ray Studies on Electrochemical Systems: Synchrotron Methods for Energy Materials*. (De Gruyter, 2017).

33 Su, X. *et al.* Silicon-Based Nanomaterials for Lithium-Ion Batteries: A Review. *Adv. Energy Mater.* **4**, (2014).

34 Szczech, J. R. & Jin, S. Nanostructured Silicon for High Capacity Lithium Battery Anodes. *Energy Environ. Sci.* **4**, 56-72, (2011).

35 Li, J. C., Dozier, A. K., Li, Y. C., Yang, F. Q. & Cheng, Y. T. Crack Pattern Formation in Thin Film Lithium-Ion Battery Electrodes. *J. Electrochem. Soc.* **158**, A689-A694, (2011).

36 Nelson, G. J., van Zandt, Z. K. & Jibhakate, P. D. Direct X-Ray Imaging as a Tool for Understanding Multiphysics Phenomena in Energy Storage. *J. Electrochem. En. Conv. Stor.* **13**, 030802-030802-030805, (2016).

CHAPTER 2

STRUCTURE OF THE PHOTO-CATALYTICALLY ACTIVE SURFACE OF $SRTIO_3$

2.1 Introduction

Wide bandgap, n-type, metal oxide semiconductors such as $SrTiO_3$, TiO_2 and WO_3 absorb UV light to form photo-generated (electrons and holes) charge carriers, capable of driving redox reactions at the interface with an electrolyte.[1-3] $SrTiO_3$ is a prototypic perovskite structure metal oxide (Figure 2.1a). The perovskites exhibit a vast range of attractive physico-chemical properties including promising energy conversion activity.[4] Since the initial reports of the ultraviolet (UV) activity of n-TiO_2 and n-$SrTiO_3$ in the 1970's, researchers have pursued a fundamental understanding of the mechanistic and molecular-level phenomena involved in photo-catalysis.[5-11] In particular, $SrTiO_3$ has very attractive photocatalytic properties. It is highly stable in base, displays high quantum efficiency for the electro-oxidation of water under UV illumination, and performs the light-driven water splitting reaction (i.e., photo-generation of both O_2 and H_2 from H_2O) under an applied bias,[6,12] at open circuit aided by an auxiliary metal electrode,[6,12] and on free-standing crystals.[7,8,12-15]

The fundamental mechanisms underlying surface photoelectrochemical reactions, however, remain unclear. While the bulk d-band structure can correlate with activity,[4] surface defects and surface structure are critically important, and it is generally difficult to decouple the bulk and surface contributions to observed changes in reactivity.[16-18] Here, we illustrate the critical role that surface structure plays by demonstrating, under *operando* conditions, that the electrochemical activation ("training") of n-doped $SrTiO_3$(001) in basic media, by biasing at 0.8 V vs. Ag/AgCl

for 40 min, induces an irreversible surface reordering that enhances (by 260%) its activity for photocatalytic water splitting.

2.2 Methods and materials

Chemicals. All chemicals for electrochemical measurements were used as received. Sodium hydroxide (NaOH, semiconductor grade, 99.99%) was from Aldrich Chemical Co. (Milwaukee, WI). Potassium hexacyanoferrate(III) (ferricyanide, $[Fe(CN)_6]^{3-}$) (ACS grade) was obtained from Fisher Scientific (Fairlawn, NJ). Mallinckrodt-Baker (Phillipsburg, NJ) was the source of potassium nitrate. Water (18 MΩ•cm) from a Millipore (Billerica, MA) Milli-Q system was used to prepare all aqueous solutions. The acid- compatible parts (glass dome, Kel-F cell, Pt wire,) were cleaned by soaking in 3 M nitric acid solutions overnight then rinsed thoroughly with water, and left resting in Milli-Q water overnight (when possible) before use. Cesium hydroxide (CsOH) solutions were prepared from a 50% wt. solution in water (99.9%, Sigma-Aldrich, St. Louis, MO). Sulfuric acid (H_2SO_4) solutions were prepared from a 99.9999% solution (92% min, Alfa Aesar, Ward Hill, MA). Strontium titanate (STO) samples were purchased from MTI Corp. Acetone (from Macron Chemicals), Isopropyl Alcohol (from Mallinckrodt Chemicals) and 7:1 NH_4F-HF buffered oxide etchant solution (from J. T. Baker, VLSI grade) was used in STO surface etching process.

Strontium titanate electrodes. As-received STO (100) samples were first cleaned with acetone and isopropyl alcohol and then sonicated in deionized water for 15 min. After cleaning, the samples were etched with 7:1 NH_4F-HF buffered oxide etching (BOE) solvent for 30 s, and then rinsed with abundant deionized water. Finally, the samples were annealed at 1000 ˚C for 2.5 hr in oxygen atmosphere, and then slowly

cooled to room temperature. The next step in the preparation was generating oxygen vacancies by annealing the samples at 10^{-7} Torr at 1000 ˚C for 1 hr.

Sample characterization. The doping level of the samples was estimated by Hall effect measurements using a cryogenic superconducting quantum interference device (SQUID) magnetometer MPMS-XL by Quantum Design in a 4 K He environment. Indium contacts to the sample ensured ohmic contacts. Electrochemical impedance analysis using a Model SI 1280B Electrochemical Measurement Unit (Solartron Analytical, Farnborough, Hampshire, UK) via Mott-Schottky analysis was performed in dark conditions in 0.1 M NaOH. Atomic force microscopy (Scanning Probe Microscope D3100, Veeco), and X-ray photoelectron spectroscopy (SSX-100, Surface Science Instrument) were measured on the sample before and after applying potential to the STO.

Operando **CTR measurement**. *Operando* CTR measurement were conducted at the Cornell High Energy Synchrotron Source (CHESS) A2 station. The X-ray energy was 30 keV, since x-ray damage to the sample is reduced by using higher energy x-ray. The flux of X-rays was 10^{11} $\mathrm{ph}/(\mathrm{s}\cdot\mathrm{mm}^2)$. X-ray intensities were collected by a 41 cm×41 cm area detector (DXR250RT, GE Inspection Technologies). Each pixel is 200 ×200 μm. The distance between the sample and the detector is 927 mm. Each exposure takes 50 seconds.

(Photo-)electrochemical measurements. The photoelectrochemical response of the STO (100) samples was characterized and con-trolled using a monochromated UV light source. We used a model 6291 200 W Hg(Xe) Lamp (Oriel Instruments, Stratford, CT) in a Spectra-Physics (Santa Clara, CA) Model 66902 Lamp Housing powered by a Spectra-Physics Model 69911 Power Supply operated at 200 W. A two-meter long Oriel Model 78278 VIS-NIR Single Fiber Cable (core diameter of 1000 μm), connected using a Model 77776 Fiber Bundle Focusing Assembly, was used to

irradiate the top of the sample through the electrolyte solution. An Oriel Model 7240 monochromator with a resolution of ± 20 nm (±0.1eV approx.) was used to select the wavelength. Scanning electrochemical microscopy experiments were performed using either an SECM 900 or SECM 920D electrochemical workstation (CH Instruments, Austin, TX). Au and Pt tips for SECM were fabricated using established methods by sealing metal microwires (either Pt 15 m, Pt 25 m or Au 25 m from Goodfellow Corporation, Oakdale, PA) in capillary tubing and sharpening the resulting microelectrodes. _ENREF_27 For cyclic voltammetric, impedance spectroscopy, and SECM measurements, STO samples were placed in a homemade Teflon cell with an o-ring exposing an area of 0.5 cm^2 to the electrolyte. Electrical contact to the STO was made using indium wire with copper tape on top of the STO surface outside of the o-ring. Surface interrogation SECM (SI-SECM) measurements were performed in a solution of 120 μM $K_3[Fe(CN)_6]$ in 0.1 M NaOH thoroughly deoxygenated with high purity nitrogen. Before the chronoamperometric SI-SECM experiment, a Pt tip was positioned to a height of ~2 μm above the STO surface as judged from the negative feedback approach curve obtained at the unbiased semiconductor in dark conditions (*i.e.*, no UV irradiation). The SECM tip was poised at 0.05 V vs. Ag/AgCl to reduce ferricyanide $[Fe(CN)_6]^{3-}$ to ferrocyanide, $[Fe(CN)_6]^{4-}$, and the same electrode reaction was used for SI-SECM transients.

2.3 Results and discussion

The *operando* structural characterization of $SrTiO_3$ before and after training was performed using high-energy X-ray reflectivity to measure the specular crystal truncation rod (CTR) during photocatalytic water splitting.[19,20] Taking advantage of the penetrating power of high energy (30 keV) X-rays, a novel photo-electrochemical

cell (Figure 2.1b), and a large format area detector optimized for hard X-rays, we measured absolute X-ray structure factors. The sub-Ångstrom sensitivity of CTR to average surface/interface structure allows us to characterize the $SrTiO_3$(001)/electrolyte interface and the bulk-like layers beneath, while maintaining strict control of the electrochemical reaction conditions. Scanning Electrochemical Microscopy (SECM)[21] was used to follow sequential functional changes (e.g., O_2 evolved or adsorbed oxygen-containing intermediates)[22,23] at the surface. Joint density-functional theory (JDFT)[24,25] was employed to calculate the electronic structure, geometry, and X-ray structure factors of the $SrTiO_3$ surface in the presence of a liquid description with atomic-scale structure.

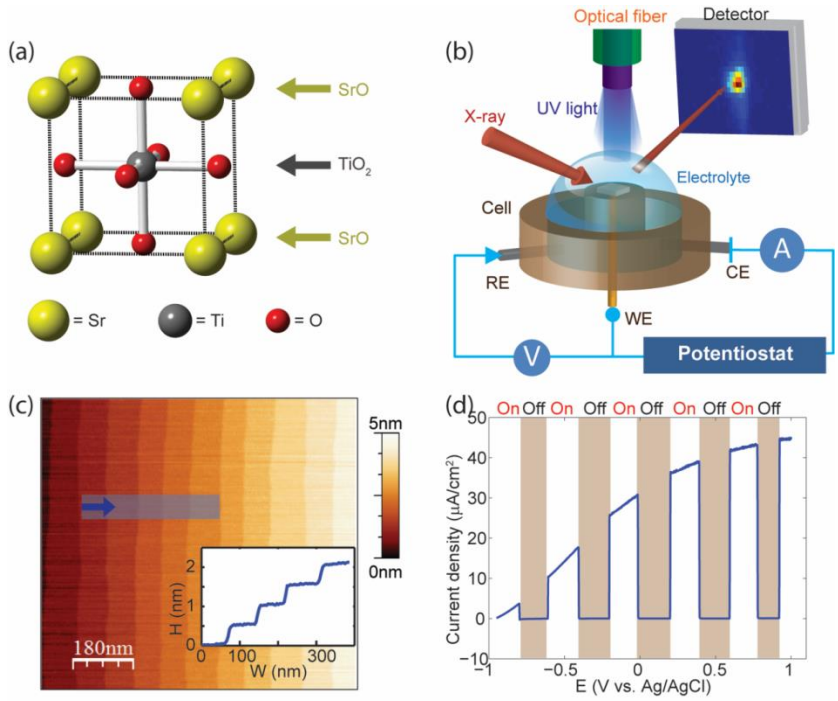

Figure 2.1 (a) $SrTiO_3$ unit cell. Crystal structure alternates SrO and TiO_2 layers along [001] (b) Schematic of the experimental set-up for *operando* X-ray reflectivity of $SrTiO_3$ during photoassisted (elec-tro)chemistry. (c) Tapping mode AFM image of

$SrTiO_3$ after surface preparation. The inset shows the height profile of the shadowed area of the AFM image. Atomic terraces are about 0.5 nm in height and 90 nm in width. (d) Light-chopped linear sweep voltammogram of $SrTiO_3$ in 0.1 M NaOH. The power of light illumination directly on the sample was 15 mW /cm^2; scan rate was 20 mV/s.

We carefully prepared the n-$SrTiO_3$ electrode to ensure an atomically smooth surface with well-defined doping and benchmarked its UV light-induced water-splitting activity to optimize our experimental design. As shown in Figure 2.1c, chemical etching produced atomically flat terraces on the $SrTiO_3$(001) surface. Precisely controlled vacuum annealing, followed by a thermal quench, fixed the bulk oxygen vacancy concentration and concomitant carrier density to $n_D \sim 1 \times 10^{17}$ cm^{-3}, producing samples with a clear photocurrent signal in 0.1 M NaOH electrolyte under illumination with a 200 W Hg/Xe lamp. Figure 2.1d shows a typical photocurrent vs. applied potential profile under chopped illumination, where the anodic photocurrent corresponds to the electrochemical oxidation of water to form O_2. Large photocurrents occur only under UV irradiation. Monochromatic UV light, centered at $\lambda = 390 \pm 20$ nm (~3.2 eV), was used in subsequent experiments to control the illumination conditions precisely.

Figure 2.2a shows the measured X-ray structure factors, $|F|^2$, of n-doped $SrTiO_3$(001) in air and in electrolyte (both before and after training). The data from samples in air are consistent with previous reports in the literature,[26] and the line-shape is the same for doped and undoped samples. Non-linear least squares fits of $|F|^2$ to atomic models (solid blue line in Figure 2.2a) suggest that the structure represents a relaxation of the well-known TiO_2 double-layer model.[27,28] Immersing the doped substrates in 0.1 M NaOH, however, dramatically alters $|F|^2$ and the resulting

(untrained) surface structure is stable in electrolyte under UV illumination. The same structural evolution also occurs in 0.1 M CsOH, suggesting that the counter cation does not play a role in these structural changes. This structural evolution does not occur for undoped samples in either 0.1 M NaOH or 0.1 M H_2SO_4. Reports in the literature previously established that photoassisted water splitting, at open circuit, is negligible for n-$SrTiO_3$ in H_2SO_4, but readily observed in basic medium.[13] Figure 2.2b schematically illustrates the dependence of the structural evolution upon doping and choice of electrolyte.

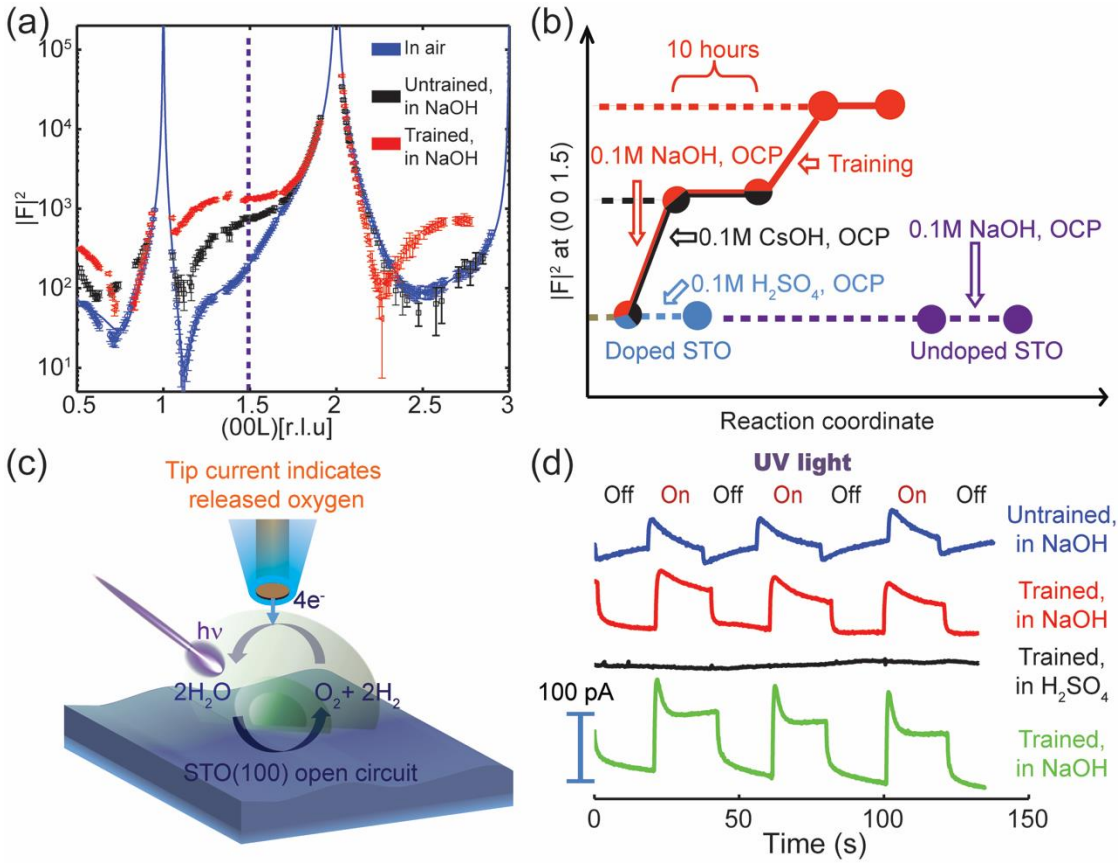

Figure 2.2 (a) Structure factor of 00L CTR of $SrTiO_3$ in air (blue), in 0.1 M NaOH at open circuit before (black) and after (red) training. r.l.u stands for reciprocal lattice units. Blue solid line is the best non-linear least squares fits to the CTR of $SrTiO_3$ in

air, using the TiO_2 double-layer model. (b) Map to the evolution of $|F|^2$ at (0 0 1.5) of samples in different electrolytes: Red, doped $SrTiO_3$ in 0.1 M NaOH; Black, doped $SrTiO_3$ in 0.1 M CsOH; Blue, doped $SrTiO_3$ in 0.1 M H_2SO_4; Purple, undoped $SrTiO_3$ in 0.1 M NaOH. (c) SECM in O_2 substrate collection mode. The Hg/Au amalgam tip detects the oxygen produced by the water splitting reaction at the $SrTiO_3$ electrode at open circuit. (d) SECM collection with UV light on/off: (blue) in 0.1 M NaOH before training, (red) after training (biasing to 0.8 V vs. Ag/AgCl for 40 min). (black) upon immersion in 0.1 M H_2SO_4 and (green) after returning to 0.1 M NaOH. The oxygen generation rate is proportional to the current, 100 pA ~ 200 mol $h^{-1}m^{-2}$.

These experimental studies of the stoichiometry and atomic structure of the untrained surface offer an excellent starting point for interpretation by JDFT calculations. Other state-of-the-art *ab initio* techniques for the study of electrochemical interfaces either require computationally prohibitive molecular dynamics to sample the liquid structure, or they consider the surface in vacuum or with only a single frozen layer of water. Our JDFT calculations efficiently include the atomically-detailed structure of a thermodynamically-sampled liquid by construction.[25] Because JDFT provides full access to the electron density of both the solid surface and the contacting liquid, we calculate $|F|^2$ and compare it directly with experiment. Figure 2.3b displays the best JDFT candidate structure for untrained $SrTiO_3$ immersed in 0.1 M NaOH, a relaxed 1×1 double-TiO_2-terminated structure. The black curve in Figure 2.3a shows that the JDFT calculated $|F|^2$ agrees extremely well with experiment with no adjustable parameters, thereby demonstrating the power of the JDFT approach. Table 2.1 shows the atomic structure of the JDFT model. The JDFT structure describes the X-ray data much more accurately than the 2×1

reconstruction that has the minimum free energy in air or an *ab initio* calculation with a single layer of water molecules adsorbed on the surface.

atom	z/a_0
Ti	0.00000
O	0.00000
O	0.00000
Sr	0.50000
O	0.50000
O	0.99069
Ti	0.99874
O	1.00812
O	1.49831
Sr	1.49964
O	1.93530
Ti	1.99698
O	2.06580
O	2.49304
Ti	2.55719
O	2.65270

Table 2.1 JDFT-calculated atomic positions for the immersed sample in the *z*-direction (normal to the surface) in units of lattice constant a_0.

As shown in Figure 2.2a, when an electrode is trained (biased to +0.8 V vs. Ag/AgCl) during UV illumination, the surface evolves to a new stable structure. Trained electrodes exhibit a significant enhancement of $|F|^2$ between the 001 and 002 peaks that is independent of the electrode potential. This enhancement of $|F|^2$ may be characterized by defining a reaction coordinate midway between the two peaks (dotted line in Figure 2.2a). Figure 2.2b summarizes the dependence of this enhancement upon doping, choice of electrolyte, and history of applied bias. SECM measurements (Figure 2.2c) using a selective O_2 microelectrode, under thoroughly de-oxygenated

conditions and UV light chop-ping, demonstrate a large increase in the photocatalytic activity on trained substrates.[21] SECM can measure the minute changes in O_2 evolution with sufficiently high temporal resolution to characterize, operando, the reactivity of the open circuit $SrTiO_3$ surface just before and after training. Although the activity at open circuit represents only a small fraction of the activity at 0.8 V vs. Ag/AgCl, the impact of the subtle surface change on the activity at open circuit is profound. The activity of the trained $SrTiO_3$ surface is 2.6 ± 0.9 times larger than that of the untrained surface.[30] (Figure 2.2d) The same substrates, even after training, were not active towards photocatalytic water splitting in acidic medium, but recovered the enhanced activity if returned back to 0.1 M NaOH (Figure 2.2d). The training-induced structural change survives removal from the electrochemical cell and thorough rinsing with water. Because, at open circuit, transport is not aided by an external field, bulk carrier recombination limits the quantum efficiency. Nevertheless, our results clearly demonstrate the correlation between the structural change, in only the topmost atomic layers, and the enhanced reactivity.

We explored two possible explanations for the training-induced structural change: (1) the formation of a photogenerated surface intermediate O(H) ad-layer; and, (2) a change in crystal structure of the surface. Pursuing the ad-layer hypothesis, we performed surface interrogation SECM,[22,23] which demonstrated that a limiting coverage, consistent with one equivalent of reactive O (or two OH) per unit cell of $SrTiO_3$, is reached at positive potentials, as shown in Figure 2.4. However, non-linear least squares fits of the X-ray data to atomic models indicated that the addition of an O(H) ad-layer alone cannot explain the observed change of $|F|^2$, particularly between the 001 and 002 peaks.

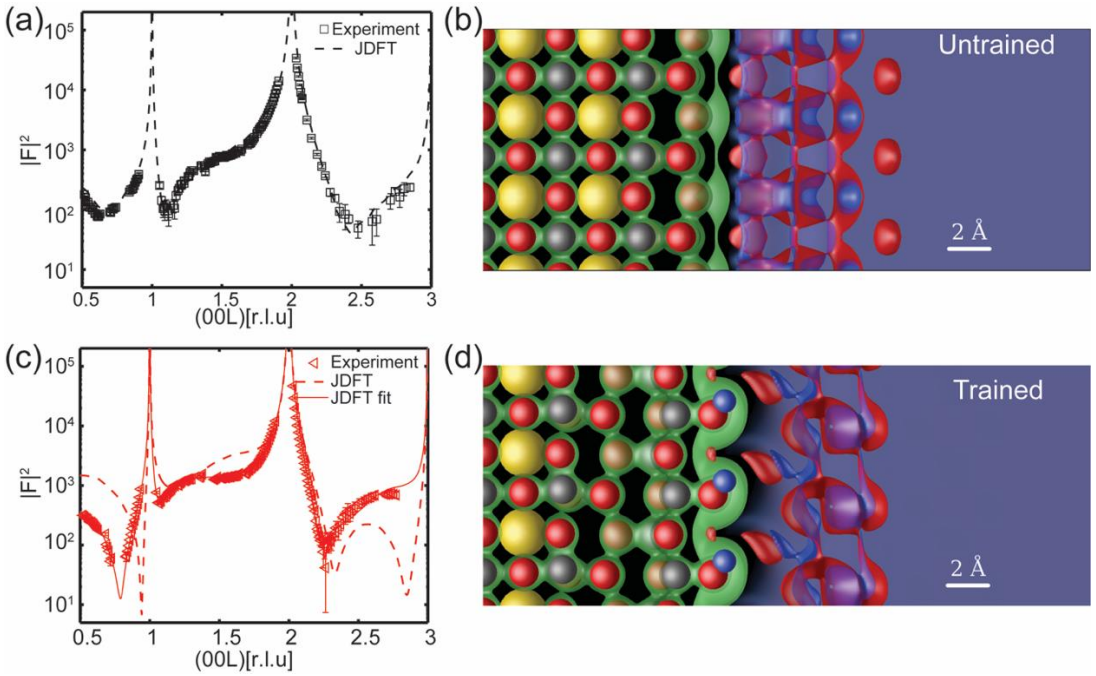

Figure 2.3 (a) Structure factor of 00L CTR of untrained $SrTiO_3$ in 0.1 M NaOH. Black squares are experimental data. Black dashed line is the structure factor calculated from the JDFT structure, with no adjustable parameters. (b) The JDFT structure for the untrained $SrTiO_3$ surface. (c) Structure factor of 00L CTR of trained $SrTiO_3$ in 0.1 M NaOH. Red triangles are experimental data. Red dashed line is from JDFT structure, with no adjustable parameters. Red solid line is a guided fit constrained to the JDFT structure with a penalty function. (d) The JDFT structure for the trained $SrTiO_3$ surface before fitting. Yellow spheres are strontium, red are oxygen, blue are hydrogen, and silver are titanium atoms. Green, red, and blue density contours represent electron, oxygen, and hydrogen density respectively.

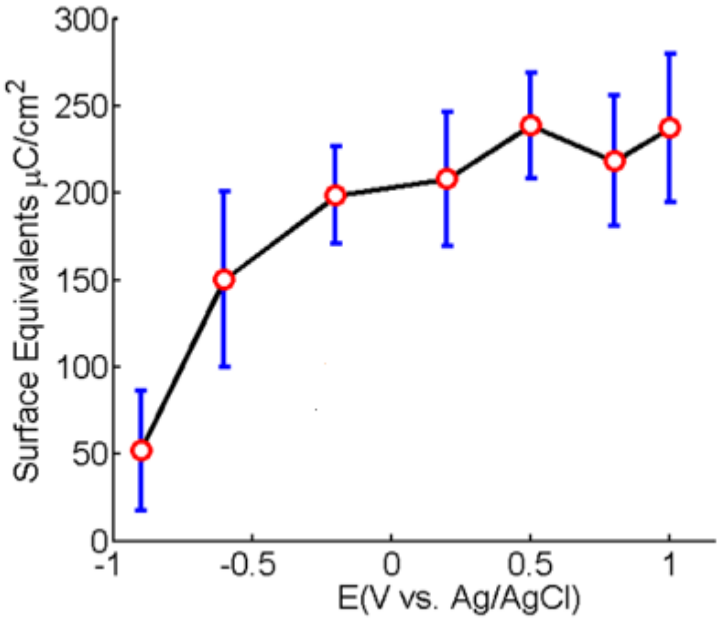

Figure 2.4. Equivalent charge for photogenerated oxygen on $SrTiO_3$ electrodes after illumination in NaOH using SI-SECM.

To explore the structure change hypothesis, we relaxed multiple (~100) surface stoichiometries and geometries within JDFT and found that the only likely candidate for the trained surface is an oxygen-deficient, biaxially strained, anatase-like structure, as shown in Figure 2.3d. Since anatase is also a catalyst for photoassisted water splitting, it is perhaps not surprising that the trained surface is associated with enhanced reactivity. At least one layer of Sr atoms has been removed, leaving a triple TiO_2 termination and explaining the observed irreversibility of the training. This predicted reduction in surface concentration of Sr is in good agreement with the XPS ex situ experiment we performed. This candidate for the trained structure has the Ti-stacking of anatase rather than $SrTiO_3$, and it is oxygen deficient at the surface. In fact, a similarly stacked triple-layer TiO_2 terminated surface has been previously observed after UHV annealing by combined XPS-STM studies[29]. This similar *ex situ* structure

has been shown to exhibit a mid-band-gap state which could provide further explanation for the observed increased activity for photoelectrochemical water-splitting.

Atom	z/a_0	$(z - z_{DFT})/a_0$	occupancy	Debye-Waller σ/a_0
Ti	0.00000	0.000	1	0.004
O	0.00000	0.000	1	0.005
O	0.00000	0.000	1	0.005
Sr	0.50000	0.000	1	0.004
O	0.50000	0.000	1	0.005
Ti	1.00719	0.014	1	0.004
O	0.94512	0.057	1	0.086
O	0.99236	0.018	1	0.005
Sr	1.51373	0.017	1	0.004
O	1.51281	0.003	1	0.169
O	1.96606	0.002	1	0.026
Ti	1.99768	0.004	1	0.071
O	2.07735	0.022	1	0.190
O	2.56112	0.040	1	0.005
Ti	2.58703	0.046	1	0.004
O	2.64567	0.037	1	0.005
Ti	3.12121	0.025	1	0.228
O	3.22553	0.011	1	0.028
O	3.31986	0.002	1	0.059
Ti	3.42910	0.018	0.4761	0.004
O	3.91892	0.047	0.9999	0.095
H	4.01449	0.000	1	0.000

Table 2.2. Best fit for the activated sample: atomic positions *z* and discrepancy from DFT positions $z - z_{DFT}$ (normal to the surface), best fit occupancies, and best fit Debye-Waller rms displacements. All positions are in units of lattice constant a_0.

The JDFT calculation which agrees best with the X-ray data for the trained surface has the stoichiometry of Ti_2O_2 at the surface with a capping hydroxide layer. However, there is still significant discrepancy between the JDFT calculation with no adjustable parameters and the experimental structure factor. (See the dotted line in Figure 2.3c)

A JDFT-guided nonlinear least squares fit to the experimental structure factor allows the atoms to move away from their minimum energy positions to consider the effect of non-equilibrium or thermal processes, and to develop partial occupancies to account for missing surface atoms and other disorder. Adding a generalized penalty function to the traditional chi-squared fit, allows exploration of other surface configurations with energies within approximately kT (room temperature) per atom of the JDFT minimum energy. The solid red curve in Figure 3c applies this JDFT-guided fit procedure to the above-described, minimum energy structure. This particular fit prevents atoms from moving more than 0.22 Å from their JDFT positions and has the excitation energy of less than 2 kT per fit atom. The partial occupancy of Ti atoms in this fit suggests a (still O-deficient) surface stoichiometry between Ti_2O_2 and TiO_2. Table 2.2 shows the atomic structure. The agreement between the JDFT-guided and experimental structure factors is now excellent, providing convincing evidence that the trained $SrTiO_3$ surface must exhibit an anatase-related structure (as in Figure 2.3d).

2.4 Conclusions

The identification of a highly reactive, anatase-related termination for the $SrTiO_3$ surface after training could have significant impact upon the field of photocatalysis. Going forward, establishing the structural and photocatalytic differences between anatase and the anatase-related surface of $SrTiO_3$(001) may provide insights into ways

to engineer improved photocatalysts. Unlike $SrTiO_3$, anatase has the disadvantage of requiring an applied bias to photo-generate both O_2 and H_2 from H_2O. However, anatase has a smaller band gap than $SrTiO_3$, enabling it to capture more of the solar spectrum. The similarity in the active surface of these established photocatalysts suggests a separation of roles between the surface and the bulk of a designer photocatalyst. For example, combining an anatase-related surface (to provide chemical stability and high catalytic activity) with an underlying host that is better matched to the solar spectrum and can impose optimal biaxial strain on the surface ($SrTiO_3$ imposes a 3.2% biaxial tensile strain) is a clear strategy for the future.

This work illustrates the critical role that history-dependent surface structure plays in the photo-catalytic water-splitting activity of $SrTiO_3$. Combining and integrating information from *operando* X-ray surface-sensitive techniques, electrochemical and functional characterization methods, and JDFT calculations, we demonstrate that training the $SrTiO_3$ electrode changes the surface structure from a double layer TiO_2 termination to an oxygen-deficient biaxially strained anatase-like structure, and concurrently triples the photoactivity. The profound dependence of electrode structure and reactivity upon the training by an applied bias has broad implications beyond just photocatalysis. The insights gained in this work are highly relevant to the design of surface chemical modifications for applications such as pollutant remediation and functional coatings, where surface reactivity under zero applied bias is key. Furthermore, the synergistic combination of *operando* measurement techniques with theory opens a promising path towards fundamental mechanistic understanding of surface reactivity in electrolyte media.

e

REFERENCES

1 Nozik, A. J. & Memming, R. Physical Chemistry of Semiconductor-Liquid Interfaces. *J. Phys. Chem.* **100**, 13061-13078, (1996).

2 Bard, A. J. Photoelectrochemistry. *Science* **207**, 139-144, (1980).

3 Tan, M. X. *et al.* Principles and Applications of Semiconductor Photoelectrochemistry. *Prog. Inorg. Chem.* **41**, 21-144, (1994).

4 Suntivich, J., May, K. J., Gasteiger, H. A., Goodenough, J. B. & Shao-Horn, Y. A Perovskite Oxide Optimized for Oxygen Evolution Catalysis from Molecular Orbital Principles. *Science* **334**, 1383-1385, (2011).

5 Fujishima, A. & Honda, K. Electrochemical Photolysis of Water at a Semiconductor Electrode. *Nature* **238**, 37-38, (1972).

6 Wrighton, M. S. *et al.* Strontium-Titanate Photoelectrodes - Efficient Photoassisted Electrolysis of Water at Zero Applied Potential. *J. Am. Chem. Soc.* **98**, 2774-2779, (1976).

7 Wagner, F. T. & Somorjai, G. A. Photocatalytic Hydrogen-Production from Water on Pt-Free SrTiO3 in Alkali Hydroxide Solutions. *Nature* **285**, 559-560, (1980).

8 Carr, R. G. & Somorjai, G. A. Hydrogen-Production from Photolysis of Steam Adsorbed onto Platinized SrTiO3. *Nature* **290**, 576-577, (1981).

9 Gratzel, M. Photoelectrochemical Cells. *Nature* **414**, 338-344, (2001).

10 Khaselev, O. & Turner, J. A. A Monolithic Photovoltaic-Photoelectrochemical Device for Hydrogen Production via Water Splitting. *Science* **280**, 425-427, (1998).

11 Bolton, J. R., Strickler, S. J. & Connolly, J. S. Limiting and Realizable Efficiencies of Solar Photolysis of Water. *Nature* **316**, 495-500, (1985).

12 Mavroides, J. G., Kafalas, J. A. & Kolesar, D. F. Photoelectrolysis of Water in Cells with Srtio3 Anodes. *Appl. Phys. Lett.* **28**, 241-243, (1976).

13 Wagner, F. T., Ferrer, S. & Somorjai, G. A. Surface Aspects of Hydrogen Photogeneration on Titanium Oxides. *ACS Symp. Ser.* **146**, 159-178, (1981).

14 Domen, K., Naito, S., Onishi, T. & Tamaru, K. Photocatalytic Decomposition of Liquid Water on a NiO $SrTiO_3$ Catalyst. *Chem. Phys. Lett.* **92**, 433-434, (1982).

15 Kraeutler, B. & Bard, A. J. Heterogeneous Photocatalytic Decomposition of Saturated Carboxylic-Acids on TiO_2 Powder - Decarboxylative Route to Alkanes. *J. Am. Chem. Soc.* **100**, 5985-5992, (1978).

16 Gerischer, H. in *Photoeffects at Semiconductor-Electrolyte Interfaces ACS Symposium series*. 16 (American Chemical Society, 1981).

17 Ong, W. J., Tan, L. L., Chai, S.-P., Yong, S. T. & Mohamed, A. R. Facet-Dependent Photocatalytic Properties of TiO_2-Based Composites for Energy Conversion and Environmental Remediation. *Chem. Sus. Chem.* **7**, 690-719, (2014).

18 Nakamura, R. *et al.* Crystal-Face Dependences of Surface Band Edges and Hole Reactivity, Revealed by Preparation of Essentially Atomically Smooth and Stable (110) and (100) n-TiO_2 (Rutile) Surfaces. *J. Phys. Chem. B* **109**, 1648-1651, (2005).

19 Robinson, I. K. Crystal Truncation Rods and Surface Roughness. *Phys. Rev. B* **33**, 3830-3836, (1986).

20 Robinson, I. K. & Tweet, D. J. Surface X-Ray-Diffraction. *Rep. Prog. Phys.* **55**, 599-651, (1992).

21 Rodr ́guez-L ́opez, J., Zoski, C. G. & Bard, A. J. in *Scanning Electrochemical Microscopy* (eds A.J. Bard & M.V. Mirkin) Ch. 16, (CRC Press, 2012).

22 Rodriguez-Lopez, J., Minguzzi, A. & Bard, A. J. Reaction of Various Reductants with Oxide Films on Pt Electrodes As Studied by the Surface Interrogation Mode of Scanning Electrochemical Microscopy (SI-SECM): Possible Validity of a Marcus Relationship. *J. Phys. Chem. C* **114**, 18645-18655, (2010).

23 Zigah, D., Rodriguez-Lopez, J. & Bard, A. J. Quantification of Photoelectrogenerated Hydroxyl Radical on TiO2 by Surface Interrogation Scanning Electrochemical Microscopy. *Phys. Chem. Chem. Phys.* **14**, 12764-12772, (2012).

24 Petrosyan, S. A., Briere, J. F., Roundy, D. & Arias, T. A. Joint Density-Functional Theory for Electronic Structure of Solvated Systems. *Phys. Rev. B* **75**, (2007).

25 Sundararaman, R. & Arias, T. A. Efficient Classical Density-Functional Theories of Rigid-Molecular Fluids and A Simplified Free Energy Functional for Liquid Water. *Comput. Phys. Commun.* **185**, 818-825, (2014).

26 Kazimirov, A., Goodner, D., Bedzyk, M., Bai, J. & Hubbard, C. X-ray Surface Diffraction Analysis of Structural Transformations on The (001) Surface of Oxidized $SrTiO_3$. *Surf. Sci.* **492**, L711-L716 (2001).

27 Herger, R. *et al.* Surface of Strontium Titanate. *Phys. Rev. Lett.* **98**, 076102 (2007).

28 Erdman, N. *et al.* The Structure and Chemistry of the TiO_2-rich Surface of $SrTiO_3$(001). *Nature* **419**, 55-58, (2002).

29 Marshall, M. S. J. *et al.* Structure and Composition of Linear TiO_x Nanostructures on $SrTiO_3$. *Phys. Rev. B* **86**, 125416 (2012).

30. Training increases the relative quantum efficiency (ratio of the efficiency at open circuit to the efficiency at 0.8V vs. Ag/AgCl) from 0.8% to 2.1%. These numbers are from measurements on five samples and at least two sites on each.

CHAPTER 3

OXYGEN REDUCTION REACTION CONDITION DRIVES REVERSIBLE STRUCTURE RECONSTRUCTION ON THE EPITAXIAL (111) $PB_2RU_2O_{6.5}$ PYROCHLORE CATALYST FILM

3.1 Introduction

Metal oxides, such as perovskites,[1,2] spinels[3,4] and pyrochlores,[5-7] have played a major role in the development of cost effective, high efficiency and stable catalysts for oxygen electrocatalysis, aiming at replacing noble metal catalysts, such as Pt. One critical issue in the study of metal oxide catalysts is to understand the link between the catalytic functionality and their structure.[8-15] However, structural information is usually based on either a pristine structure or in the *ex situ* measurement on powdered samples,[12,14] which brings the ambiguousness of (1) whether the pristine structure can represent the structure under the functioning conditions; (2) what is the role of crystal facet on the catalytic activity. To understand the structure and catalytic activity of the catalyst, the important concept of single crystal electrode was adopted,[16] because it constrains the reaction happening only on the desired crystallographic plane with well-defined surface area. Moreover, it generates the crystal truncation rod (CTR) signal that could be measured from SXRD measurement to obtain atomically precise structure in *operando* condition,[17] either of which could not be obtained with powdered sample. Although single crystal electrodes have been extensively applied into metallic electrode systems,[18,19] there are only few examples where the single crystal electrodes of metal oxide catalyst in oxygen eletrocatalysis were successfully applied.[10]

Defect pyrochlore lead ruthenate ($Pb_2Ru_2O_{6.5}$, space group $F\bar{4}3m$) has attracted significant interest as potential catalyst for oxygen electrocatalysis, because it exhibits

unique oxygen vacancy ordering of O' site in general pyrochlore formula $Pb_2Ru_2O_6O'_{1-\delta}$, where the half of O' site is absent (i.e. $\delta = 0.5$),[20] causing the metallic conductivity.[21] It shows high catalytic activity and electrical conductivity and bi-functionality for both oxygen reduction reaction (ORR) and oxygen evolution reaction (OER).[11,22-24] Figure 3.1a (left) illustrates the unreconstructed pristine atomic structure of $Pb_2Ru_2O_{6.5}$ viewed along the $[1\bar{1}0]$ zone-axis (RuO_6 octahedral is red, Pb is blue, and O' is blue). The corner shared RuO_6 octahedral framework provides the electron conduction path.[21] In Figure 3.1a (right), the position of $PbRu_3$ layer was marked as black dash, Pb_3Ru layer as grey, O from RuO_6 octahedral as green, and O' as blue. Along the (111) direction, the $Pb_2Ru_2O_{6.5}$ pyrochlore unit cell can be simplified as $PbRu_3$ Pb_3Ru, O and O' layer repeating structure. The black dashed diamond motif draws the smallest repeating unit on (110) plane.

In this paper, we measure the atomic-precision structure of the (111)-oriented epitaxial $Pb_2Ru_2O_{6.5}$ thin film catalyst under the *operando* condition of oxygen electrocatalysis with surface X-ray diffraction. We discover that, for the first time, the oxygen reduction reaction condition could drive the reconstruction of $Pb_2Ru_2O_{6.5}$ pyrochlore unit cell, causing the formation of RuO_6 octahedral and, moreover, this structure reconstruction is reversible with the applied potential.

3.2 Methods and materials

Thin film growth. $Pb_2Ru_2O_{6.5}$ thin films are grown on (111) $Sm_2Ti_2O_7$ substrates by adsorption-controlled molecular-beam epitaxy (MBE) technique. The Veeco Gen 10 MBE system used in this study is described in detail elsewhere. We use the 10x10 mm (111) $Sm_2Ti_2O_7$ substrates grown by Czochralski technique, (Institute of Crystal Growth, Max-Born-Str. 2, D-12489 Berlin, Germany.). The atomically smooth surface

of $Sm_2Ti_2O_7$ substrate was achieved by mechanically polishing with silica powder (Crystec, Germany). Effusion cell generated the elemental Pb-flux, and e-beam evaporator generated the Ru-flux. The flux value was determined using a quartz crystal microbalance (QCM) prior to growth. 1.0×10^{6} Torr of the 10% O_3+O_2 gas mixture was used as oxidant during growth. All components of lead, ruthenium, and 10% O_3+O_2 gas were supplied simultaneously. We utilized an over-pressure of Ru-flux (2.0×10^{13} atoms/cm^2·sec) to use adsorption controlled growth technique, which was about 3 times higher than the Pb-flux (0.6×10^{13} atoms/cm^2·sec). The growth temperature for single phase $Pb_2Ru_2O_{6.5}$ was maintained at 480-500 ℃, which is monitored by optical pyrometer. The single-phase $Pb_2Ru_2O_{6.5}$ growth was observed by *in situ* reflection high-energy electron diffraction (RHEED). Overall $Pb_2Ru_2O_{6.5}$ growth rate was about 0.05 Å/sec, limited by Pb-flux supply. Finally, film growth was terminated by closing Pb and Ru shutter, and the sample was cooled under the same 1.0×10^{6} Torr of the 10% O_3+O_2 background pressure. By following these conditions, the epitaxial (111) $Pb_2Ru_2O_{6.5}$ single crystal thin film was achieved.

Electrochemical characterization. Electrochemical measurements were performed in 0.1M NaOH on Solartron electrochemical analyzer at room temperature. The $Pb_2Ru_2O_{6.5}$ thin film sample was mounted into a homemade Teflon rotating disc electrode. The graphite felt was tightly pressed inside the electrode allowing the electric contact from the back of the sample to a stainless-steel rotating shaft. After assembly, the entire electrode was rinsed and then transferred to a standard three-compartment electrochemical cell containing N_2-saturated 0.1M NaOH solution. A Pt wire was used as the counter electrode and a Ag/AgCl in saturated KCl as the reference electrode. All reference potential in this work was converted into reversible hydrogen electrode (RHE) scale. Cyclic voltammetry curves were obtained under N_2

atmosphere at 50 mV/s. Rotating disk electrode (RDE) measurement was performed in O_2-saturated 0.1M NaOH at 10mV/s, with rotation rate from 10 to 1600 rpm.

***Operando* CTR measurement.** The *operando* CTR measurements were conducted in A-2 station at Cornell High Energy Synchrotron Source (CHESS), with a homemade electrochemical cell designed for the *operando* X-ray diffraction measurement. The main parts of the cell are made from polyether ether ketone (PEEK). There are four threaded holes on the cap, through which the counter electrode, the reference electrode, gas-in (O_2 or N_2) and gas-out are connected to the electrolyte. A graphite rod (Sigma Aldrich) and a saturated Ag/AgCl electrode were used as the counter electrode and the reference electrode, respectively. A copper wire is connected to the back of the sample through a hole in the bottom part of the cell. Because the $Sm_2Ti_2O_7$ substrate is electrical insulating, conductive carbon paint (SPI supplies) was used to electrically connect from the edge of the film to back face of the sample along the side, and then connected with a copper wire on the bottom part of the cell. The middle part of the cell is to avoid the exposure of the carbon paint and copper wire in the electrolyte. The electrodes are connected to a potentiostat (Princeton Applied Research). To obtain both high penetration of X-ray through the chemical cell and high angular resolution on the detector, the energy of X-ray is adjusted to 26.9 keV. The flux of X-ray beam is 1.51×10^{11} ph $s^{-1}mm^{-2}$. The diffraction signal was collected with a 2D detector (PILATUS 300K, Dectris) with the pixel size of 172 $\times$172 μm^2. The CTR was measured while performing chronoamperometry at a series of potentials: 0.11, 0.36, 0.66, 0.91 V vs. RHE.

***Ex situ* characterization AFM and TEM.** Cross-sectional atomic-resolution high-angle dark field scanning transmission electron microscopy (HAADF-STEM) in conjunction with electron energy loss spectroscopy (EELS) was conducted across the film/substrate interface (100 keV NION EELS-SI ultraSTEM). The elemental EELS

mapping was constructed by Pb M4,5, Ru M4,5, Ti L2,3 and Sm M4,5 absorption edge, respectively. The surface morphology was characterized by atomic force microscopy (AFM).

3.3 Results and discussion

The 10 nm thick epitaxial $Pb_2Ru_2O_{6.5}$ thin film was grown on $Sm_2Ti_2O_7$ (111) substrate by reactive molecular-beam epitaxy (MBE, see Methods). The adsorption-controlled growth by MBE provides the excellent stoichiometry control and highest crystalline quality. We used the non-commercial substrate pyrochlore $Sm_2Ti_2O_7$ (111), because the lattice mismatch is less than 0.2 %, the coherent $Pb_2Ru_2O_{6.5}$ thin film growth is obtained. Figure 3.1b shows the atomic-precision cross-sectional image of $Pb_2Ru_2O_{6.5}/Sm_2Ti_2O_7$ (111) interface viewed along the $[1\bar{1}0]$ zone-axis with (111) surface normal direction in vertical, taken by the high-angle annular dark field scanning transmission electron microscopy (HAADF-STEM). The electron density difference in between the $Pb_2Ru_2O_{6.5}$ film and $Sm_2Ti_2O_7$ substrate could distinguish the atomically abrupt interface. Inset of Figure 3.1b shows a zoom-in atomic resolution HAADF-STEM image of the $Pb_2Ru_2O_{6.5}$ film. The black dashed diamond shape motif indicates the same repeating unit with that of Figure 3.1a. Figure 3.1c and 1d show the cross-sectional elemental mappings utilizing electron energy loss spectroscopy (EELS) at the film/substrate interface, which is marked as a red box in Figure 3.1b. The repeating unit of the film was also marked with black dashed diamond motif. Although the signal to noise ratio of $Pb_2Ru_2O_{6.5}$ is lower than that of the $Sm_2Ti_2O_7$ substrate, due to the high edge energy selected for mapping Pb and Ru, the composition at the interface could still be clearly observed, formed by Ru-rich termination of $Pb_2Ru_2O_{6.5}$ and Ti-rich termination of $Sm_2Ti_2O_7$. The grown $Pb_2Ru_2O_{6.5}$ film also shows atomically smooth surface (Figure 3.1e, Atomic force

microscope, AFM, image). The inset shows the height profile in the shadowed area of AFM image. The $Pb_2Ru_2O_{6.5}$ surface develops clear propagated terraces, with terrace width of 800 nm on average. The height of terraces is about 0.6 nm, which corresponds to (111) d-spacing in $Pb_2Ru_2O_{6.5}$. Some parts of the film surface exhibited triangular shaped nucleation sites. It comes from the step flow growth nature of $Pb_2Ru_2O_{6.5}$ thin film after forming some nuclei on the (111) $Sm_2Ti_2O_7$ substrate,[25] as consistent with the RHEED intensity saturation. The streaky RHEED patterns during the growth confirmed the atomically smooth surface of $Pb_2Ru_2O_{6.5}$ film.

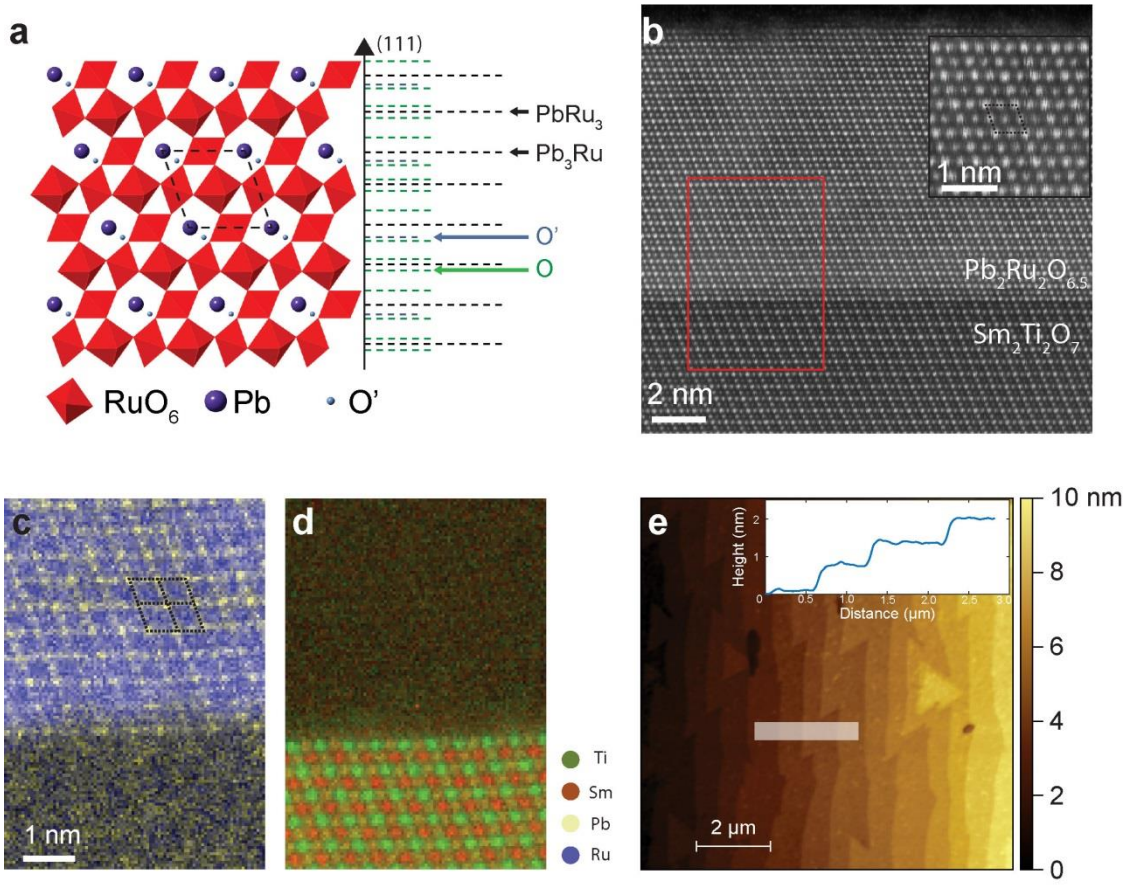

Figure 3.1 Structure characterization for the grown $Pb_2Ru_2O_{6.5}$ thin film. (a) The structure of $Pb_2Ru_2O_{6.5}$ viewed along the [110] zone-axis. The dashed lines mark the atomic position projected along (111) direction. (b) The high-angle annular dark field

scanning transmission electron microscopy image of the $Pb_2Ru_2O_{6.5}/Sm_2Ti_2O_7$ sample viewed along the $[1\bar{1}0]$ zone-axis. The red box highlights the interfacial region. The inset is a zoom-in image, with the dashed diamond motif showing the repeating units. (c)-(d), The cross-sectional elemental mappings with electron energy loss spectroscopy of the red box region in (b). (e) The atomic force microscopy (AFM) image of the $Pb_2Ru_2O_{6.5}/Sm_2Ti_2O_7$ sample. The inset is the height profile of the shadowed area in AFM image.

The catalytic activity of the $Pb_2Ru_2O_{6.5}$ film was characterized by cyclic voltammetry (CV) and rotating disk electrode (RDE) techniques. As shown in Figure 3.2a, the CV curve of the (111) $Pb_2Ru_2O_{6.5}$ thin film was obtained in N_2-saturated 0.1 M NaOH solution from 0.05 V to 1.0 V vs. RHE at 50 mV/s. In the scanned region, a pair of weak redox peaks appears, with the positions similar to that from the $Pb_2Ru_2O_{6.5}$ powder samples as reported in the literature.[5] The anodic peak at around 0.44V was assigned to the oxidation of Ru from Ru^{2+} to Ru^{3+}, and in the reversible direction, the weak reduction peak at around 0.33 V was attributed to the reduction process of Ru^{3+} to Ru^{2+}. The ORR activity was further measured by RDE with a custom-made rotating disk electrode, as shown in Figure 3.2b. The polarization curves were obtained at 10 mV/s scanning rate from positive to negative direction, at a variety of rotating speed, from 10 to 1600 rpm. At low rotating rate (10 rpm) which was chosen to examine its ORR activity, the current increases exponentially with decreasing potential, which is characteristic of kinetic control. At more-negative potentials, the current becomes increasingly controlled by mass transport. The electron transfer number calculated from limiting current density at 0.2V was around 2.55, which indicated that two-electron pathway should be dominant. Although the

magnitude of the catalytic activity of epitaxial (111) $Pb_2Ru_2O_{6.5}$ film is lower than that from powdered sample, mainly due to the low number of active sites (or even possibly the surface defects) only at the top surface of the film and incapability to bind with carbon to decrease the resistance, it exhibits quite similar catalytic behavior as the reported results from powdered samples.

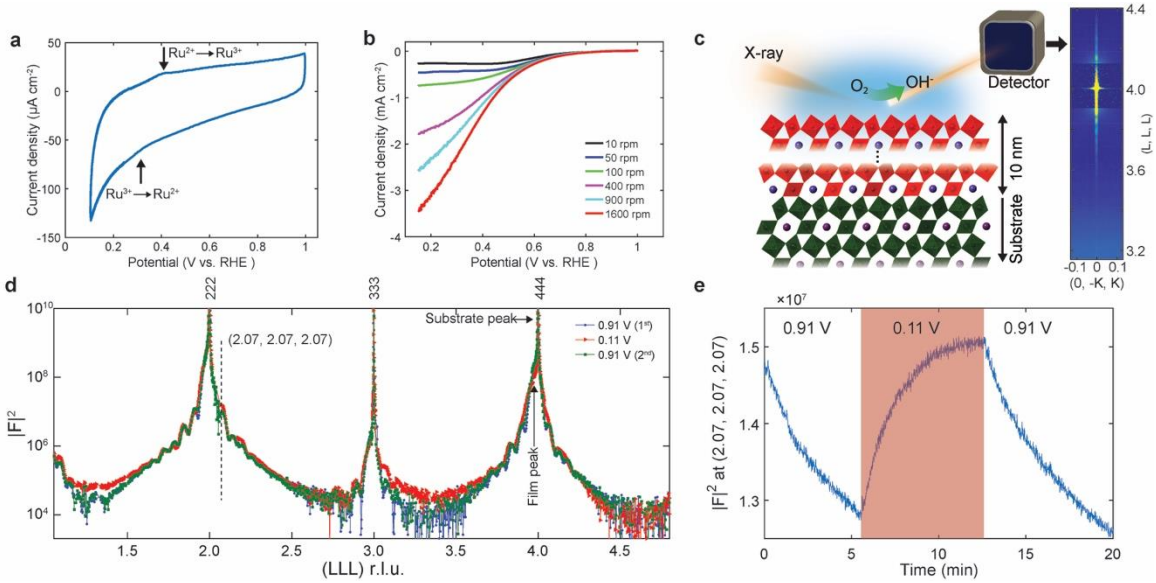

Figure 3.2. The electrochemical characterization and *operando* CTR measurement of the $Pb_2Ru_2O_{6.5}$ thin film. (a) The cyclic voltammetry of $Pb_2Ru_2O_{6.5}/Sm_2Ti_2O_7$ in N_2-saturated 0.1 M NaOH at the rate of 50 mV/s. (b) The polarization curve for oxygen reduction reaction on $Pb_2Ru_2O_{6.5}/Sm_2Ti_2O_7$ at 10 mV/s with various rotating rates. (c) The illustration of the *operando* surface X-ray diffraction experiment while performing oxygen reduction reaction. (d) The 111 crystal truncation rod (CTR) of $Pb_2Ru_2O_{6.5}/Sm_2Ti_2O_7$ measured at 0.91 V (blue), at 0.11 V (red) and returning back to 0.91 V (green). (e) The intensity transient of one point on CTR (2.07, 2.07, 2.07) while stepping potential between 0.91 V and 0.11 V.

To investigate the influence of the oxygen electrocatalysis condition to the structure of the $Pb_2Ru_2O_{6.5}$, the specular LLL CTR of the sample was measured while performing chronoamperometry on the sample with continuous O_2 bubbling, as illustrated in Figure 3.2c. Figure 3.2d presents the LLL CTR measured on the same sample at different conditions. The blue dotted curve was measured at potential 0.91 V vs. RHE, which is around the open circuit potential, naming $\mathbf{CTR_{ocp}}$. As shown in $\mathbf{CTR_{ocp}}$, the positions of Bragg peaks of $Pb_2Ru_2O_{6.5}$ thin film overlap with those of the $Sm_2Ti_2O_7$ substrate, indicating lattice between the film and the substrate is highly matched. The clear fringe, called Kiessig fringe, aroused from the contrast of electron density between the film and substrate, could be clearly observed. Based on the periodicity of the Kiessig fringes, the $Pb_2Ru_2O_{6.5}$ film thickness was confirmed to be 10.4 nm. When biasing the sample into ORR region and below 0.21 V which slightly passes the reduction peak of Ru, the CTR intensity starts to change, indicating the structure of $Pb_2Ru_2O_{6.5}$ start to be reconstructed. The red dotted curve was CTR measured at 0.11 V, naming $\mathbf{CTR_{bias}}$. The $\mathbf{CTR_{bias}}$ shows clear difference with the $\mathbf{CTR_{ocp}}$, not only between Bragg peaks, such as (3.30, 3.30, 3.30) where the intensity is increased by 4 times, but also around the Bragg peaks, such as (2.07, 2.07, 2.07) where the intensity is increased by 70%. This indicates this structural reconstruction of $Pb_2Ru_2O_{6.5}$ film does not merely occur in the topmost surface layer, but happens deeply through the whole film. It should be noted that the periodicity of Kiessig fringes and the position of Bragg peaks of the film remain unchanged, whereas the contrast of Kiessig fringes around Bragg peaks is significantly decreased. This means neither the whole thickness nor the lattice structure of the $Pb_2Ru_2O_{6.5}$ film alters during the reconstruction, and the main reason causing the CTR change is the reconstruction of unit cell of $Pb_2Ru_2O_{6.5}$. Surprisingly, this reconstructed structure

could change back to the pristine structure when returning to OCP. Figure 3.2e plots the X-ray intensity transient at (2.07, 2.07, 2.07) while performing chronoamperometry, stepping potential between 0.91 V and 0.11V, indicating that the observed structure reconstruction in the unit cell of $Pb_2Ru_2O_{6.5}$ is reversible with the applied potential. The CTR was taken at OCP after holding at 0.91 V vs. RHE for one hour, as shown the green squared curve in Figure 3.2d referred as $\mathbf{CTR_{ocp\text{-}return}}$, where we could observe clearly that the $\mathbf{CTR_{ocp\text{-}return}}$ overlapped to the initial $\mathbf{CTR_{ocp}}$, confirming the reversibility of the structure reconstruction. In contrast, in OER condition, the structure does not show any reconstruction. On account of the fact that the structure change is reversible with the potential, it could not be detected with *ex situ* methods. With the combination of single crystal $Pb_2Ru_2O_{6.5}$ catalyst thin film and extremely high structure sensitive characterization like CTR measurement, we observed, for the first time, this reversible structure reconstruction of $Pb_2Ru_2O_{6.5}$ in the ORR condition.

In order to understand the structure of reconstruction that drives the change in CTR, we developed a CTR analysis method, Fourier space fitting, calculating the real space structure model that agrees with CTR profile. Figure 3.3a displays the CTR plots calculated from the best agreed models for $\mathbf{CTR_{ocp}}$ (top) and $\mathbf{CTR_{bias}}$ (bottom), overlaid with the experimental data. The corresponding electron density along (111) direction of the models, $\boldsymbol{\rho_{ocp}}$ and $\boldsymbol{\rho_{bias}}$, is shown in Figure 3.3b. Figure 3.3e overlays the atomic position from pristine $Pb_2Ru_2O_{6.5}$ (as shown in Figure 3.1a) with $\boldsymbol{\rho_{ocp}}$. The profile of $\boldsymbol{\rho_{ocp}}$ perfectly agrees with the atomic position in pristine $Pb_2Ru_2O_{6.5}$. The film contains 18 pairs of bilayers, with the thickness of 10.4 nm. The interfacial layer, Pb_3Ru, becomes slightly broader than others, suggesting the less ordering at the interface, and is only partial occupied (about 90%), both of which agree with results from elemental map in the film in Figure 3.1c. The topmost atomic layer is partial

occupied (about 70%), which could be due to the re-evaporation in the sample post-growth cooling. Figure 3.3b and 3.3f (bottom) compare ρ_{ocp} and ρ_{bias}, showing that neither the occupancy nor the position of Pb and Ru atoms were altered in the structure reconstruction. In the topmost layer, the electron number is increased by about 10 per unit cell on the surface. This number corresponds to adding one more OH^- per unit cell. More importantly, the oxygen atoms, especially those on the right shoulder of the Pb_3Ru layer (O_{right}), move during the reconstruction. The movement of oxygen atoms happens almost through the whole film, and is especially clear in the middle region of the film, as illustrated in Figure 3.3g. In the middle region of the film, the movement of O_{right} is around 0.4 Å, which suggests the RuO_6 is deformed in the reconstruction.

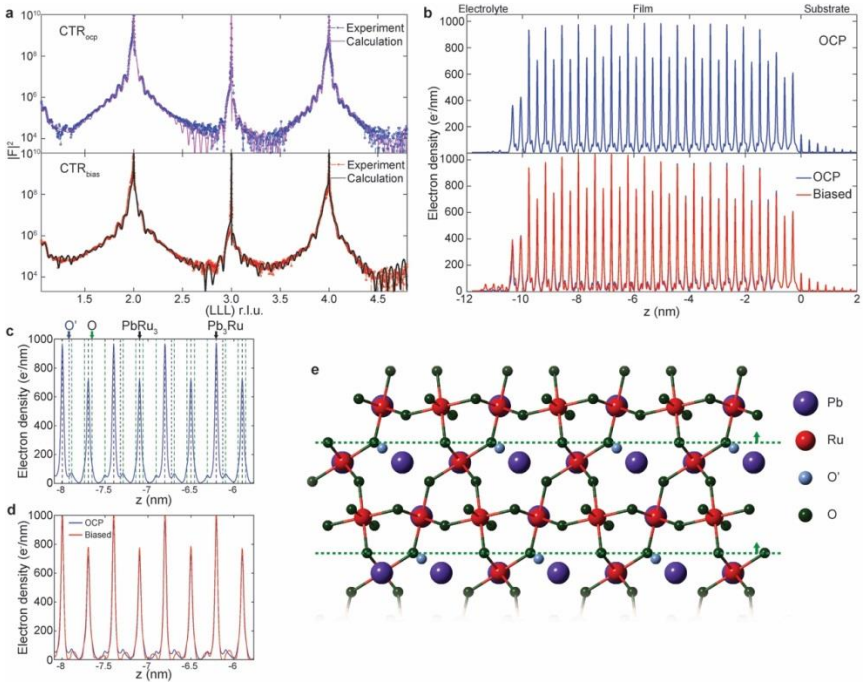

Figure 3.3 The electron density calculated from CTR profile and the structure reconstruction in the oxygen reduction reaction condition. (a) The calculated LLL crystal truncation rod (CTR) from best fitted model, compared with experimental data

for **CTR_{ocp}** (top) and **CTR_{bias}** (bottom). (b) The real space electron density along (111) for best fitted model for **CTR_{ocp}** (ρ_{ocp}) and **CTR_{bias}** (ρ_{bias}). (c) A selected region from ρ_{ocp} with the position calculated from bulk unit cell structure of $Pb_2Ru_2O_{6.5}$. (d) The same selected region with (c) from both ρ_{ocp} and ρ_{bias}. (e) The illustration of the structure reconstruction in the oxygen reduction reaction.

3.4 Conclusions

By conducting *operando* CTR measurement on $Pb_2Ru_2O_{6.5}$ (111) thin film at oxygen electrocatalysis condition, we revealed, for the first time, that the oxygen reduction reaction could drive a reversible structure reconstruction of $Pb_2Ru_2O_{6.5}$ unit cell, which causes deformation of the RuO_6 octahedral. Along (111) direction, the bond distance between Ru and O increases by about 0.4 Å. This structure reconstruction does not merely happen at the topmost layers, but happens almost through the film. Epitaxial single crystal thin film, when combined with *operando* surface probe: CTR measurement, turns to be an ideal platform to measure the structure of catalyst under its functioning environment and discover the link between functionality and catalyst structure. We hope this work could provide a framework for the fuel cell study and, more broadly, catalytic materials.

REFERENCES

1 Savinell, R. F. Oxygen-Reduction Catalysts Picking Perovskites. *Nat. Chem.* **3**, 501-502, (2011).

2 Suntivich, J. *et al.* Design Principles for Oxygen-Reduction Aactivity on Perovskite Oxide Catalysts for Fuel Cells and Metal-Air Batteries. *Nat. Chem.* **3**, 546-550, (2011).

3 Han, X. P., Zhang, T. R., Du, J., Cheng, F. Y. & Chen, J. Porous Calcium-Manganese Oxide Microspheres for Electrocatalytic Oxygen Reduction with High Activity. *Chem. Sci*. **4**, 368-376, (2013).

4 Maiyalagan, T., Jarvis, K. A., Therese, S., Ferreira, P. J. & Manthiram, A. Spinel-type Lithium Cobalt Oxide as a Bifunctional Electrocatalyst for the Oxygen Evolution and Oxygen Reduction Reactions. *Nat. Commun.* **5**, (2014).

5 Goodenough, J. B., Manoharan, R. & Paranthaman, M. Surface Protonation and Electrochemical Activity of Oxides in Aqueous-Solution. *J. Am. Chem. Soc.* **112**, 2076-2082, (1990).

6 Modeshia, D. R. & Walton, R. I. Solvothermal Synthesis of Perovskites and Pyrochlores: Crystallisation of Functional Oxides under Mild Conditions. *Chem. Soc. Rev.* **39**, 4303-4325, (2010).

7 Gökağaç, G. & Kennedy, B. J. Oxidative Stability of Bismuth-Ruthenium Pyrochlore $Bi_2Ru_2O_{7-y}$. *J. Electrochem. Soc.* **368**, 235-239, (1994).

8 Suntivich, J., May, K. J., Gasteiger, H. A., Goodenough, J. B. & Shao-Horn, Y. A Perovskite Oxide Optimized for Oxygen Evolution Catalysis from Molecular Orbital Principles. *Science* **334**, 1383-1385, (2011).

9 Han, B. H. *et al.* Nanoscale Structural Oscillations in Perovskite Oxides Induced by Oxygen Evolution. *Nat. Mater.* **16**, 121-126, (2017).

10 Chang, S. H. *et al.* Functional Links between Stability and Reactivity of Strontium Ruthenate Single Crystals during Oxygen Evolution. *Nat. Commun.* **5**, 4191, (2014).

11 Prakash, J., Tryk, D., Aldred, W. & Yeager, E. Investigations of Ruthenium Pyrochlores as Bifunctional Oxygen Electrodes. *J. Appl. Electrochem.* **29**, 1463-1469, (1999).

12 Fujii, K., Sato, Y., Takase, S. & Shimizu, Y. Effects of Oxygen Vacancies and Reaction Conditions on Oxygen Reduction Reaction on Pyrochlore-Type Lead-Ruthenium Oxide. *J. Electrochem. Soc.* **162**, F129-F135, (2015).

13 Beck, N., Steiger, B., Scherer, G. & Wokaun, A. Methanol Tolerant Oxygen Reduction Catalysts Derived from Electrochemically Pre-treated $Bi_2Pt_{2-y}Ir_yO_7$ Pyrochlores. *Fuel cells* **6**, 26-30, (2006).

14 Dawood, F., Leonard, B. M. & Schaak, R. E. Oxidative transformation of intermetallic nanoparticles: An Alternative Pathway to Metal/oxide Nanocomposites, Textured Ceramics, and Nanocrystalline Multimetal Oxides. *Chem. Mater.***19**, 4545-4550, (2007).

15 Saito, M. *et al.* Electrocatalytic O2 Reduction Properties of Pyrochlore-Type Oxides for Alkaline DAFCs. *ECS Transactions* **16**, 891-900, (2008).

16 O'Mullane, A. P. From Single Crystal Surfaces to Single Atoms: Investigating Active Sites in Electrocatalysis. *Nanoscale* **6**, 4012-4026, (2014).

17 Braun, A. *X-ray Studies on Electrochemical Systems: Synchrotron Methods for Energy Materials*. (De Gruyter, 2017).

18 Korzeniewski, C., Climent, V. & Feliu, J. Electrochemistry at Platinum Single Crystal Electrodes, in *Electroanalytical Chemistry Electroanalytical Chemistry: A Series of Advances* 75-170 (CRC Press, 2011).

19 Stamenkovic, V. R. *et al.* Improved Oxygen Reduction Activity on Pt_3/Ni(111) via Increased Surface Site Availability. *Science* **315**, 493-497, (2007).

20 Beyerlein, R. A. *et al.* Neutron Diffraction Investigation of Ordered Oxygen Vacancies in the Defect Pyrochlores, $Pb_2Ru_2O_{6.5}$ and $PbT1Nb_2O_{6.5}$. *J. Solid State Chem.* **51**, 253-265, (1984).

21 Cox, P. A., Egdell, R. G., Goodenough, J. B., Hamnett, A. & Naish, C. C. The Metal-to-semiconductor Transition in Ternary Ruthenium (IV) Oxides: a Study by Electron Spectroscopy. *J. Phys.C* **16**, 6221, (1983).

22 Park, J. *et al.* Single Crystalline Pyrochlore Nanoparticles with Metallic Conduction as Efficient Bi-Functional Oxygen Electrocatalysts for Zn-air Batteries. *Energy Environ. Sci.***10**, 129-136, (2017).

23 Zen, J. M., Kumar, A. S. & Chen, J. C. Electrochemical Behavior of Lead–Ruthenium Oxide Pyrochlore Catalyst: Redox Characteristics in Comparison with that of Ruthenium Dioxide. *J. Mol. Catal. A: Chem.***165**, 177-188, (2001).

24 Oh, S. H., Black, R., Pomerantseva, E., Lee, J.-H. & Nazar, L. F. Synthesis of a Metallic Mesoporous Pyrochlore as a Catalyst for Lithium–O_2 Batteries. *Nat. Chem.* **4**, 1004-1010, (2012).

25 Voigtländer, B., Weber, T., Šmilauer, P. & Wolf, D. E. Transition from Island Growth to Step-Flow Growth for Si/Si(100) Epitaxy. *Phys. Rev. Lett.* **78**, 2164-2167, (1997).

CHAPTER 4

DIRECT VISUALIZATION OF SULFUR CATHODES: NEW INSIGHTS INTO LI-S BATTERIES VIA *OPERANDO* X-RAY BASED METHODS

4.1 Introduction

The development of novel high performance electrical energy storage systems (EES) with energy densities surpassing those of state-of-the-art lithium ion batteries (LIBs) has become increasingly important, due to the dramatic increase in their applications, especially in transportation.[1-4] Lithium sulfur (Li-S) batteries are an especially promising option because elemental sulfur has a high theoretical capacity of 1,672 mAh g^{-1}, is abundant, inexpensive and environmentally benign.[5-9] However, there are several road blocks hindering the practical deployment of Li-S batteries including the formation of highly soluble, as well as insoluble, species during cycling, and the fact that both sulfur and lithium sulfide (Li_2S) are electrical insulators. In addition, some of the long-chain polysulfide intermediates are soluble in the electrolyte (*vide supra*), causing the loss of active material and leading to rapid capacity fade. Moreover, dissolved polysulfides can be reduced and re-oxidized between the anode and cathode, resulting in the self-discharge process known as the "shuttle mechanism".

Since Nazar group's initial work on the preparation of sulfur electrodes by infiltrating sulfur into mesoporous carbons, which yielded cycling stability enhancements,[10] significant efforts have been made to develop other alternatives for high performance sulfur-based cathode materials.[11-14] These efforts have resulted in significant improvements in overall performance. Concurrently, numerous experimental probes have been developed and employed in an effort to unravel the reaction mechanism, while the battery is under operation ("*operando* methods").[15-23] Despite these efforts, there is still no consensus on the mechanistic details. For

example, recent work by Waluś et al. using *operando* X-ray diffraction (XRD) found that the diffraction signal from sulfur completely disappeared at the end of the upper plateau during the discharge, and that monoclinic sulfur (β-S_8) formed during the recharge step.[15] Contrary to that, using *operando* X-ray microscopy (XRM), Johanna et al. found that the sulfur particles did not dissolve significantly in the discharge and they did not observe changes in the morphology during the re-charge process.[16]

In an effort to obtain a more complete understanding of the reaction mechanism, we have carried out both *operando* XRD and XRM during battery operation along with X-ray tomography. In our case, we obtain excellent agreement from all three techniques. By characterizing the battery over its entire (discharge/recharge) cycle, we have observed, in real time, significant changes in both morphology and diffraction features (structure). Additionally, we demonstrate, for the first time, the role that current density and temperature play in determining the size of sulfur clusters and Li_2S particles.

4.2 Methods and materials

Electrochemical characterization. Sulfur electrodes were prepared by coating a homogeneous slurry onto carbon paper (AvCarb EP40, Fuelcell Store). The slurry was made of sulfur (Aldrich), super P carbon, and polyvinylidene fluoride (60:25:15 wt%) dissolved in N-methyl-2-pyrrolidinone (NMP) solvent. A 3 mm diameter hole was made in the center of a 2032-type coin cell and sealed with Kapton tape and Torr Seal epoxy to serve as an X-ray transmissive window. The electrolyte consisted of 1.0 M lithium bis(trifluoromethanesulfonyl)imide (LiTFSI) in 1,3-dioxolane (DOL)/ 1,2-dimethoxyethane (DME) solvent with 0.2 M $LiNO_3$ additive. The coin cells, with affixed X-ray windows, were assembled in an argon-filled glove box. Lithium metal

was used as both reference and counter electrodes, while the sulfur electrode was used as the working electrode. Unless otherwise noted, the cells were cycled at a rate of 0.1 C (1 C =1672 mAh g^{-1}) at room temperature, with a potentiostat (Biologic SP-200).

In the lithium/polysulfide battery experiment, a polysulfide (0.5 M Li_2S_8) catholyte with carbon paper was used. Stoichiometric amounts of Li_2S and sulfur were added to the electrolyte mentioned above and mixed by stirring at 60 ℃ overnight in the glove box. For cycling, the current density was fixed at 0.1 mA for discharging and variable, between 0.05 and 0.5 mA, for charging during 5 cycles.

***Operando* XRD.** *Operando* XRD experiments were performed at the A-1 station of the Cornell High Energy Synchrotron Sources (CHESS) at an X-ray energy of 19.8 keV. The diffraction signal was collected using an area detector (Dexela 2923) with a pixel size of 74.8 μm and a total area of 290 × 230 mm^2. The distance between sample and detector was 66 cm. The diffraction signal was collected every 4 min. For temperature controlled experiments, the cells were mounted in a home-made coin cell holder, with coolant liquid running through the holder to maintain constant temperature. The temperature was controlled and monitored with a water bath circulator (Thermo Scientific NESLAB).

***Operando* XRM.** *Operando* XRM was performed at the F-3 station of CHESS using an incident X-ray energy of 10.0 keV. Images were collected using a Scintillator-coupled Andor camera (Neo 5.5 sCMOS), with a resolution of about 2 μm. The distance between the sample and detector was between 2.0 and 23.2 cm. For absorption contrast imaging without phase enhancement, a distance of about 2 cm was chosen. For phase contrast imaging, the distance chosen was 23.2 cm.

X-ray tomography. Tomography was performed at the F-3 station of CHESS. A setup similar to that used for *operando* XRM was employed, except the sample stage was on an air bearing rotation stage enabling the acquisition of projected images of the

sample at different angles. In total, 900 projected images were taken within 180 degrees, with acquisition time of 15 seconds for each image.

Computational details. Density Functional Theory calculations were carried out using the JDFTx code, with the generalized-gradient approximation PBE,[38] GBRV ultrasoft pseudopotentials with the recommended wavefunction and charge-density kinetic energy cutoffs (20 Eh and 100 Eh, respectively). A set of sulfur anions (and neutral S_8) were geometrically relaxed in a 20 Bohr square box, in the presence of the continuum fluid "glyme",[40] with a 1.2 M concentration of ions. The anionic species considered were: S^{1-}, S^{2-}, S_2^{2-}, S_3^{1-}, S_3^{2-}, S_4^{1-}, S_4^{2-}, S_5^{1-}, S_5^{2-}, S_6^{1-}, S_6^{2-}, S_7^{1-}, S_7^{2-}, S_8, S_8^{1-}, S_8^{2-}, S_9^{2-}, S_9^{3-}, S_{10}^{2-}. The sulfur species were solvated by a linear continuum fluid with a dielectric constant of 7.2, closely approximating the dielectric of the 1,3-dioxolane (DOL)/1,2-dimethoxyethane (DME).

Solution free energies from these calculations were combined with a statistical mechanics calculation to predict the equilibrium concentration of each sulfur anion or molecule, at a given amount of excess negative charge, (or equivalently, the number of lithium cations needed to screen the negative charges). These statistical mechanics calculations were performed for 1 mM sulfur solutions, with variable lithium ion concentrations. Within the grand canonical ensemble, we determined the chemical potentials, at given net sulfur and lithium concentrations, and subsequently used those to find the concentration of each sulfur anion/molecule.

4.3 Results and discussion

Evolution in morphology and crystal structure during cell discharge. Figure 4.1a presents a combined schematic of the experimental set-ups for *operando* XRD and XRM. Both XRD and XRM were performed in real time, with the battery under

operation (*operando*). The morphology of the sulfur electrode was measured via XRM. For XRD, the diffraction signals from the electrode were collected with a large area detector in a transmission geometry. A CR-2032 coin cell, with X-ray transparent windows (Kapton), was galvanostatically charged and discharged. 1.0 M LiTFSI bis(trifluoromethanesulfonyl)imide in 1,3-dioxolane (DOL)/1,2-dimethoxyethane (DME) solvent with 0.2 M $LiNO_3$ additive was used as the supporting electrolyte. The voltage profile during the first discharge, at a rate of 0.1 C (1 C = 1,672 mAh g^{-1}, the initial discharge capacity was 1,311 mAh g^{-1}), is shown in Figure 4.1b. Two distinct voltage plateaus were observed at about 2.4 and 2.1 V, which is consistent with the reported initial discharge profiles of the Li/S system in ether-based electrolytes.[21-24]

Figure 4.1c presents the powder diffraction patterns of the sulfur electrode at different depths of discharge (DODs). The initial structure of sulfur is orthorhombic α-S_8 (see Figure 4.2a for the crystal structure of α-S_8). The intensity of the α-S_8 diffraction peaks decreased rapidly until about 13% DOD, with only 6% of the initial intensity remaining. The α-S_8 diffraction peak intensity continued to slowly decrease, disappearing completely near end of the upper voltage plateau. The Li_2S diffraction peaks appeared at the start of the lower voltage plateau, and increased, asymptotically approaching their maximum value at the end of the discharge, as can be clearly observed in Figure 4.1d. Figure 4.1d presents the integrated intensities of both the α-S_8 (222) and the Li_2S (111) diffraction peaks, shown as yellow and red circles, respectively. There have been conflicting reports as to when the Li_2S peaks appear in the discharge. Some reports have claimed that Li_2S is not observed until the middle of the lower voltage plateau,[20] while others suggest that the formation of Li_2S starts at the beginning of the lower plateau.[15,19] Our results clearly agree with the latter.

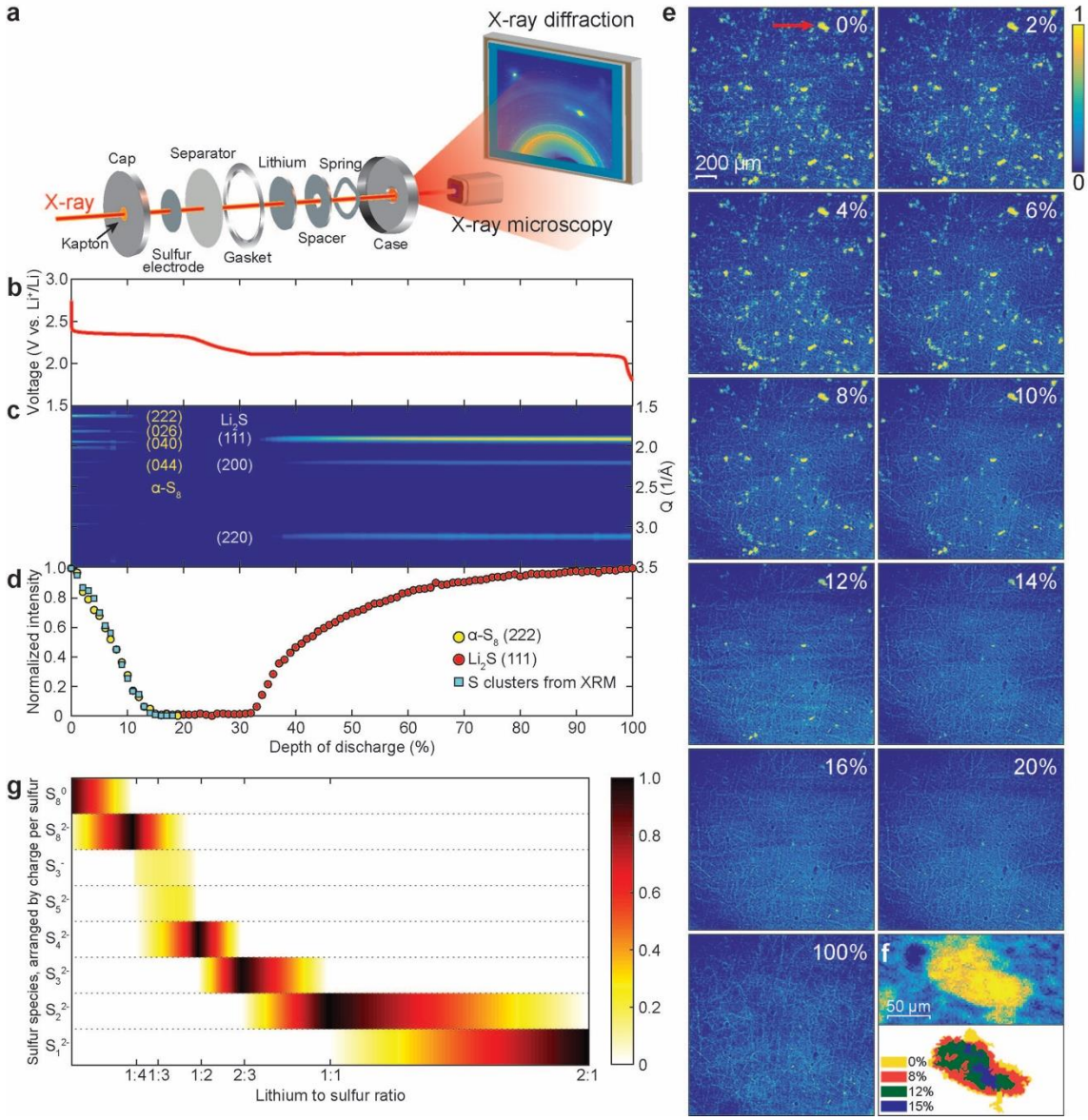

Figure 4.1 *Operando* X-ray microscopy and diffraction for Li-S batteries during the initial discharge. (a) Combined schematic illustration of the experimental set-ups for X-ray microscopy and diffraction. (b) Voltage profile, (c) *operando* X-ray diffraction pattern and (d) normalized intensity of α-S_8 and Li_2S of the sulfur electrode at a rate of 0.1 C (1C = 1672 mAh g^{-1}) during discharge. Yellow and red circles in (d) indicate normalized X-ray diffraction intensities of α-S_8 (222) and Li_2S (111), respectively. The sky blue squares are the normalized amount of all sulfur clusters calculated based

on the total integrated signal from X-ray microscopy. (e) *Operando* X-ray microscopy images of a sulfur electrode at different depths of discharge (DODs) indicated as a %. (f) Enlarged image of a single sulfur cluster in the region indicated by a red arrow at 0% DOD (top) and area changes of the same cluster at different DODs (bottom). (g) Computed equilibrium fraction of total sulfur for a given sulfur species, with varying lithium concentration, from statistical mechanics calculations using DFT energies of solvated sulfur species.

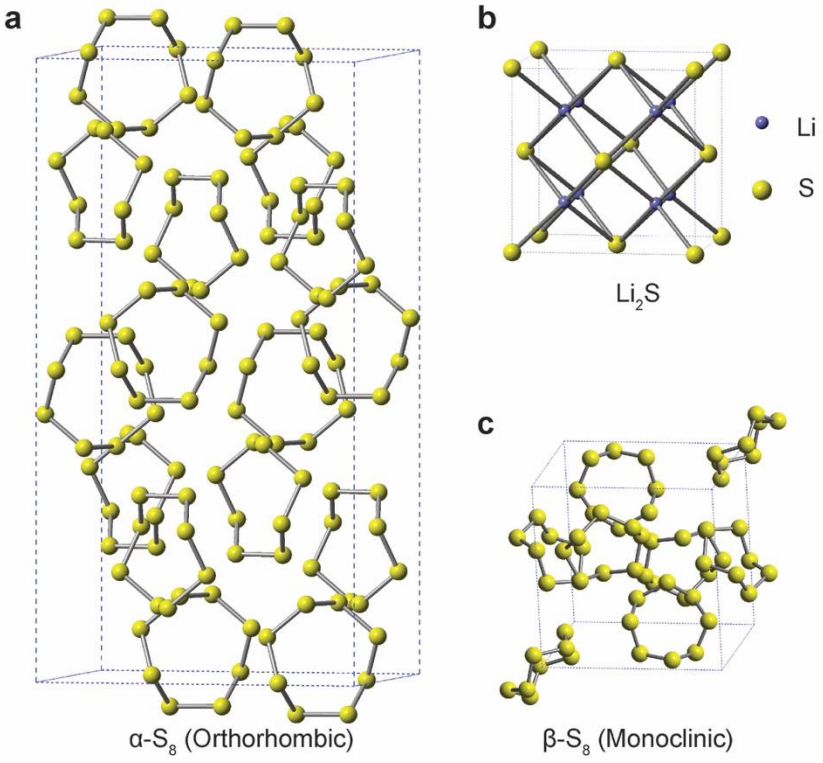

Figure 4.2 Unit cell structure of (a) α-S_8, (b) Li_2S and (c)β-S_8.

In XRM, two types of contrast information are available, absorption and phase. Phase contrast sharpens the edges of objects. Experimentally, the distance between the sample and the detector modulates the level of phase contrast. In the XRM images

(Figure 4.1e and Figure 4.3), the bright yellow clusters are sulfur, while the thread-like features arise from the carbon fibers, used as the current collector. While the sulfur particles can be readily observed using only absorption contrast (Figure 4.3b), the carbon fibers are difficult to resolve. However, by increasing the phase contrast (Figure 4.3d-f), the carbon fibers become clearly visible. Figure 4.1e shows the XRM of a sulfur electrode at different DODs, and clearly illustrates the formation of sulfur clusters. In order to identify the location and morphology of both the sulfur and carbon fibers simultaneously, we employed the enhanced phase contrast experimental configuration. From Figure 4.1e, one can surmise that the initial sulfur clusters are randomly distributed on the carbon current collector and that their size distribution is inhomogeneous with some clusters having a projected area as large as 4000 μm^2. The sulfur clusters begin to dissolve concomitantly with the start of the cell discharge. At 20% DOD, all the sulfur clusters have disappeared, and no other resolvable features emerge during the rest of the discharge. This indicates that the size of the Li_2S formed, which will be discussed in Figure 4.4, is below the resolution limit of XRM. Figure 4.1f (top panel) shows a single sulfur cluster, which is marked by a red arrow, at 0% DOD (top left panel) in Figure 4.1e. Figure 4.1f (bottom panel) shows the change in area, of the same cluster, at different DODs. It is evident that the dissolution of the cluster is from the edges to the center.

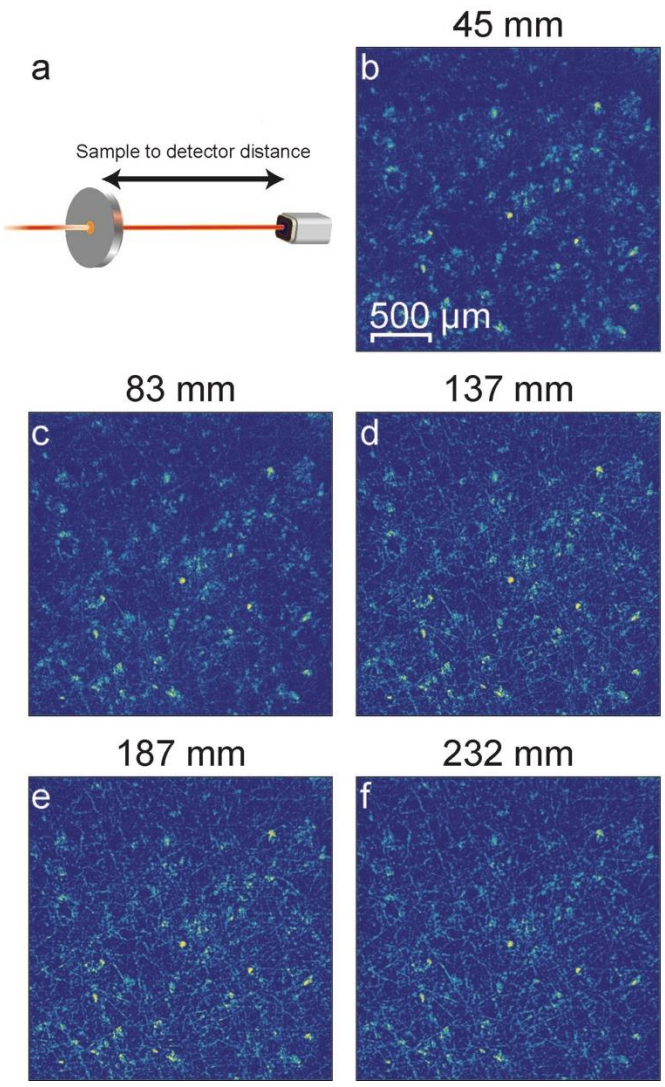

Figure 4.3 X-ray microscopy of sulfur electrode at different distances between the sample and detector.

In order to obtain a more detailed understanding of sulfur dissolution, the change in area of all of the observed sulfur clusters was further analyzed. The integrated intensity of all of the sulfur clusters in the XRM image is plotted as blue squares in Figure 4.1d. The XRM data closely track the integrated intensity of the diffraction peak from α-S_8 (222), strongly supporting the identification of these XRM features as sulfur in the crystalline alpha phase (α-S_8). Figure 4.1g presents results from DFT

calculations of the equilibrium state among various sulfur species at different lithium to sulfur ratios. For S_8, the calculated DFT profile decreases linearly as the lithium level increases, matching our XRD and XRM results (see Figure 4.1d) in which signals from crystalline sulfur decrease linearly. However, it is worth noting that the calculated profile for Li_2S increases linearly with lithium, starting at a ratio of 1:1 between lithium and sulfur, which does not match the XRD results. In Figure 4.1d, the increase in diffraction intensity from Li_2S slows down during the discharge, which might be due to the increasing coverage of Li_2S (an insulator) on the surface of the carbon fiber current collector.[15,25]

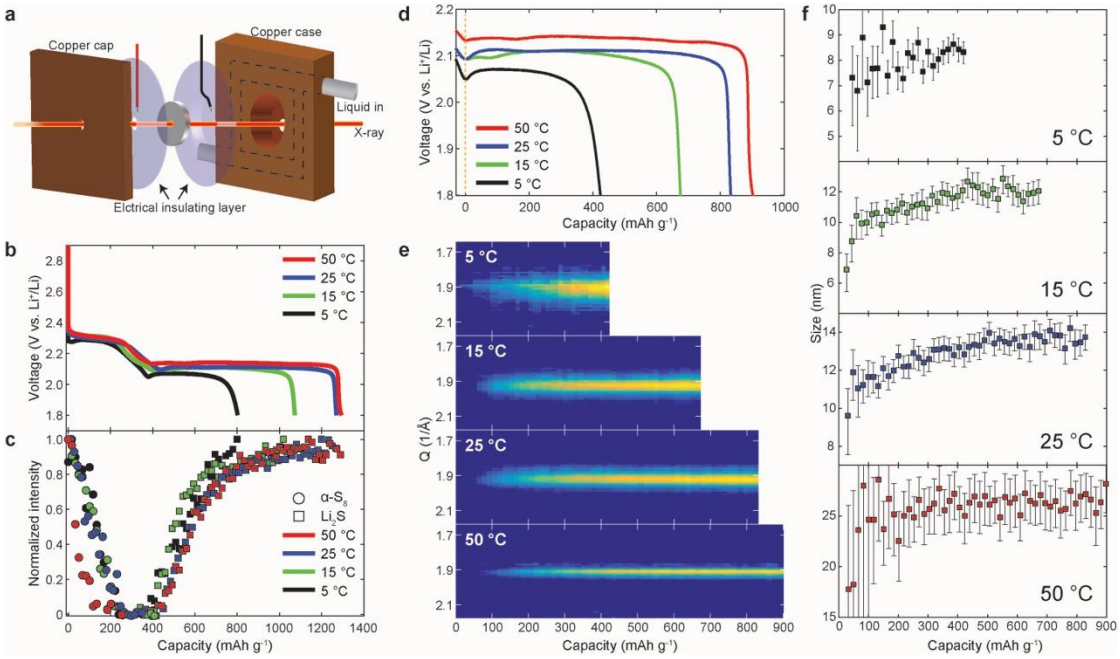

Figure 4.4 *Operando* X-ray diffraction for Li-S batteries during the initial discharge at different temperatures. (a) Schematic depiction of the temperature controlled experiment. (b) Voltage profiles, (c) normalized intensity of X-ray diffraction from α-S_8 and Li_2S of the sulfur electrodes at a rate of 0.2 C (1C = 1672 mAh g^{-1}) during discharge at different temperatures. (d) Voltage profiles, (e) *operando* X-ray

diffraction pattern and (f) particle size of Li_2S calculated from the Li_2S (111) Bragg peak of the sulfur electrodes during the lower plateau at different temperatures, after shifting the capacity to be zero at the beginning of the lower plateau.

Temperature effects on discharge and the formation of Li_2S particles. To further understand the nucleation/growth of Li_2S, we discharged lithium/sulfur cells at a rate of 0.2 C at different temperatures, while conducting *operando* XRD. Figure 4.4a shows the experimental setup of *operando* X-ray measurements with a temperature-controlled home-made cell holder. Figure 4.4b shows the voltage profiles during the first discharge at 5, 15, 25 and 50 ℃. It is evident that while the upper voltage plateau was only slightly affected, the lower plateau was significantly influenced by temperature. Figure 4.4c presents the normalized powder diffraction intensity from α-S_8 and Li_2S. For α-S_8, the intensity decreased linearly with capacity, except at 50 ℃ (red trace), where the intensity dropped rapidly. Figure 4.4d presents the voltage profile for the lower plateau at various temperatures, after shifting the capacity to be zero at the beginning of the lower plateau. As is evident, the overpotential for the formation of Li_2S increases as the temperature decreases, suggesting an activation process. In fact, if one employs the value of the discharge capacity as a proxy for the rate (since all profiles were obtained at the same C-rate (0.2 C), we feel that this is a reasonable assumption) one can glean additional information. For example, as mentioned above, the upper plateau discharge profile was minimally affected by temperature. We believe that this likely arises from the fact that the first process in the discharge is generally assumed to represent the breakage of the S_8 rings of solid sulfur, and their subsequent dissolution, and such processes are likely to be minimally affected by temperature (assuming that the temperature is well below the melting

temperature of sulfur, which was the case in these studies.) For the lower plateau, which was significantly affected by temperature, it appears that the rate reaches an asymptotic maximum value. In addition, an Arrhenius-type plot (ln k versus 1/T) for the first three points, yields a straight line with an excellent correlation (R=0.981; see Figure 4.5), again consistent with an activation process. Figure 4.4e shows the diffraction pattern of Li_2S (111) at different temperatures as a function of capacity for the lower plateau. The Li_2S particle size (obtained via the Scherrer equation) is plotted in Figure 4.4f. It is evident that the Li_2S particle size is smaller at lower temperatures, which might be due, at least in part, to the higher number of nuclei induced by the larger overpotential as well as to lower transport rates.

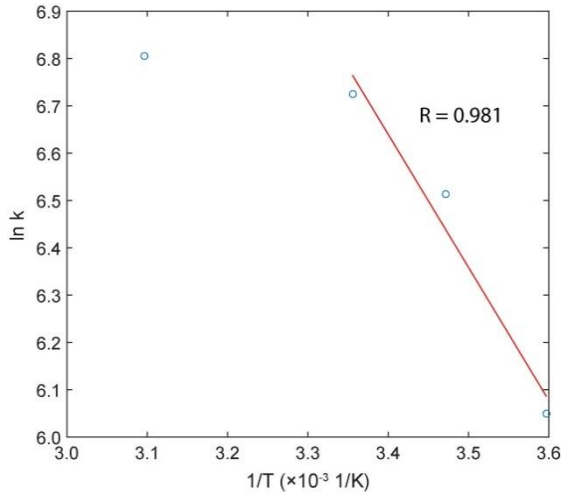

Figure 4.5 The relationship between ln k and 1/T for the formation of Li_2S.

Evolution in morphology and crystal structure during re-charge. The voltage profile, *operando* XRD patterns and XRM images of the sulfur electrode during re-charging are shown in Figure 4.6a-e. In the voltage profile (Figure 4.6a), a potential barrier is observed at the very early stages of charging, likely due to the activation energy required to oxidize the insoluble (and insulating) Li_2S to polysulfides.[26]

Subsequently, the potential increased continuously until reaching a plateau at about 2.4 V. From the XRD pattern of the sulfur electrode during charging (Figure 4.6b), the intensity of the diffraction peaks of Li_2S decreased and disappeared at about 80% state of charge (SOC). After the plateau at 2.4 V (around 90% SOC), the diffraction peaks of β-S_8 emerged. The normalized intensities of the diffraction peaks of Li_2S (111) and β-S_8 (310) are plotted as red and orange circles in Figure 4.6c, respectively.

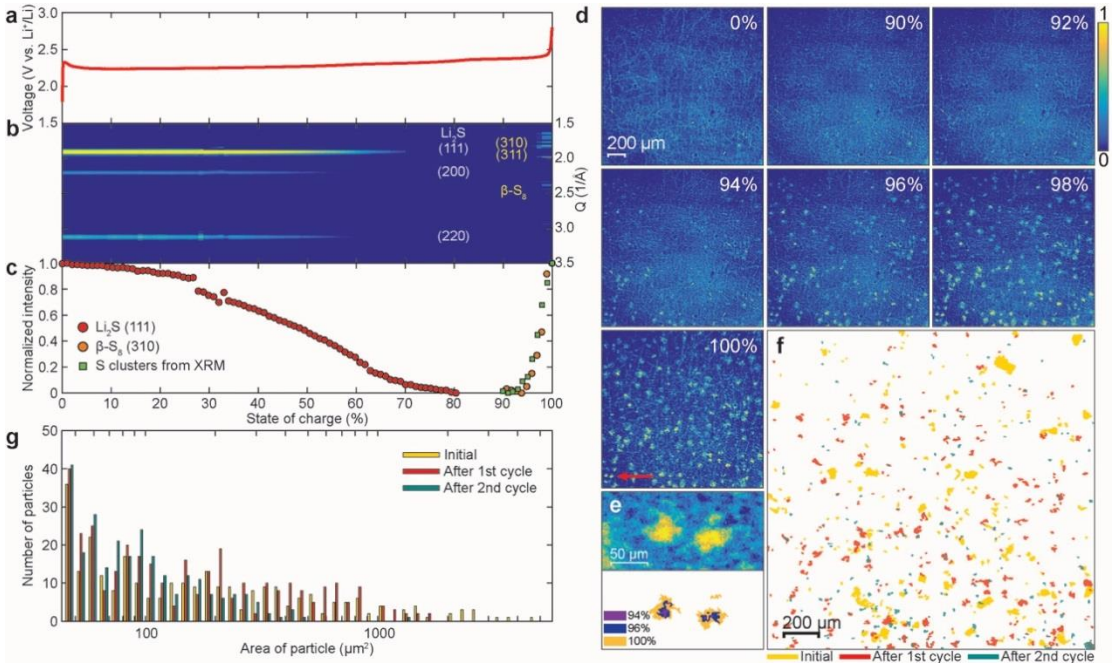

Figure 4.6 *Operando* X-ray microscopy and diffraction for Li-S batteries during charge in the initial cycle and comparison of sulfur cluster size and location between cycles. (a) Voltage profile, (b) *operando* X-ray diffraction pattern and (c) normalized intensity of Li_2S and β-S_8 of sulfur electrode at a rate of 0.1 C during charge. The red and orange circles in (c) are the normalized X-ray diffraction intensities of Li_2S (111) and β-S_8 (310), respectively. The green squares represent the normalized amount of all sulfur clusters calculated based on the total integrated signal from X-ray microscopy. (d) *Operando* X-ray microscopy images of a sulfur electrode at different states of

charge (SOCs). (e) Enlarged image of sulfur clusters formed in the region indicated by the red arrow at 100% SOC (top) and area changes of the clusters at different SOCs (bottom). (f) Shapes of sulfur clusters on the electrode before cycling (yellow), overlapped with reformed clusters after the first (red) and second (green) cycles. Images were taken at identical locations on the cathode. (g) Size histograms of sulfur clusters on the electrode before cycling (yellow), after the first cycle (red), and second cycle (green).

Figure 4.6d presents XRM images of a sulfur electrode at different SOCs. Initially, no sulfur clusters are observed. At approximately 90% SOC, the sulfur clusters emerge. The size distribution of the sulfur clusters, grown during recharge, is more homogeneous than the initial distribution. These results clearly illustrate the differences between the dissolution and reformation of sulfur clusters under *operando* conditions during full discharge/re-charge cycles. Figure 4.6e shows two sulfur clusters formed, marked by a red arrow at 100% SOC in Figure 4.6d, and their growth. The integrated intensity from all the sulfur clusters in the XRM experiment was plotted as the green squares in Figure 4.6c, and compared with the intensity of β-S_8 (310). The very good agreement between the two, suggests that the sulfur clusters shown in the XRM are, in fact, β-S_8.

Figure 4.6f presents the contour changes of the sulfur clusters on the electrode before cycling (yellow), and reformed after the 1^{st} (red) and 2^{nd} cycles (green). As can be seen, the locations of the sulfur clusters on the electrode before cycling and after subsequent cycles are different, indicating that sulfur cluster formation is independent of cycle number, including the initial configuration. A histogram of the projected area of the sulfur clusters in Figure 4.6f is presented in Figure 4.6g. The area of the sulfur

clusters becomes smaller after each cycle, including the initial one. After the 2nd cycle, the percentage of clusters with an area larger than 1000 μm^2 is only 0.4%, which is much less than the initial value (8.2%) as well as the value after the 1st cycle (3.9%) (see table S1 for details). The decrease in cluster size with cycle number is mainly attributed to the loss of active material by polysulfide dissolution into the electrolyte.

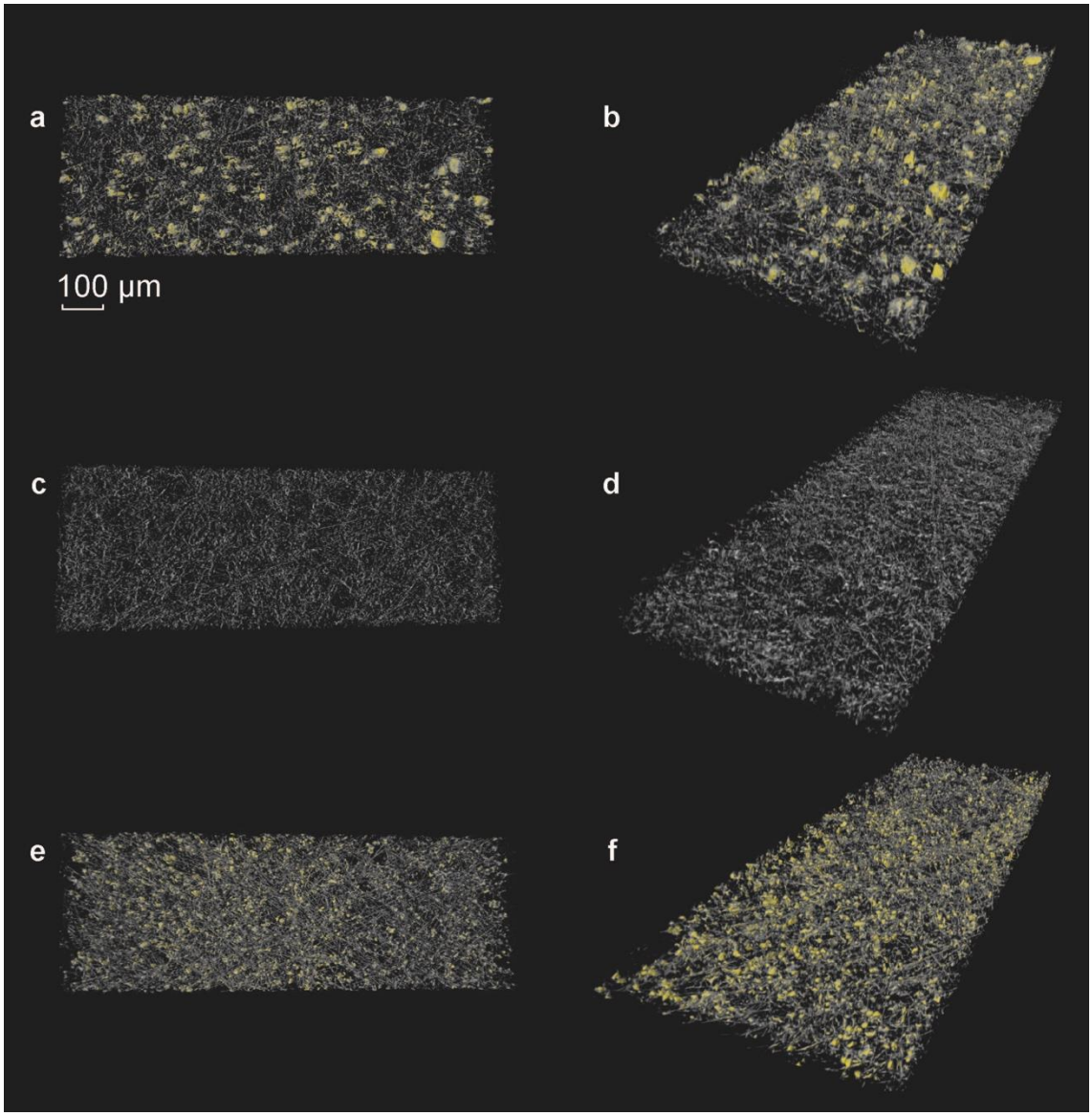

Figure 4.7 X-ray tomography of sulfur electrode before and after battery test. Front and perspective views of (a, b) pristine electrode, (c, d) after the first discharge, and (e,

f) charge, respectively. Yellow represents sulfur particles, and grey represents carbon species.

Tomography of sulfur electrodes. In order to further analyze the three-dimensional morphology of the electrode, X-ray tomography was performed. Figure 4.7 presents the reconstructed image of the pristine sulfur electrode (Figure 4.7a, b), the electrode after discharge (Figure 4.7c, d) and after re-charge (Figure 4.7e, f). The difference in the attenuation lengths of sulfur and carbon makes the respective features clearly distinguishable. The yellow features represent the sulfur clusters, and the grey, the carbon species. In general, the grey network structure is from the carbon fibers. However, note that on the pristine samples (Figure 4.7a and b), grey shells cover the sulfur clusters. These shells are from the carbon additive and/or binder. After discharge, only the carbon fibers remain (Figure 4.7c and d). After re-charge, the clusters are uniformly dispersed and their sizes are smaller and more homogeneous in size when compared to the pristine sample (Figure 4.7e and f). The reformed sulfur clusters are no longer covered with a (carbon) shell, as was initially observed in the pristine sample (*vide supra*).

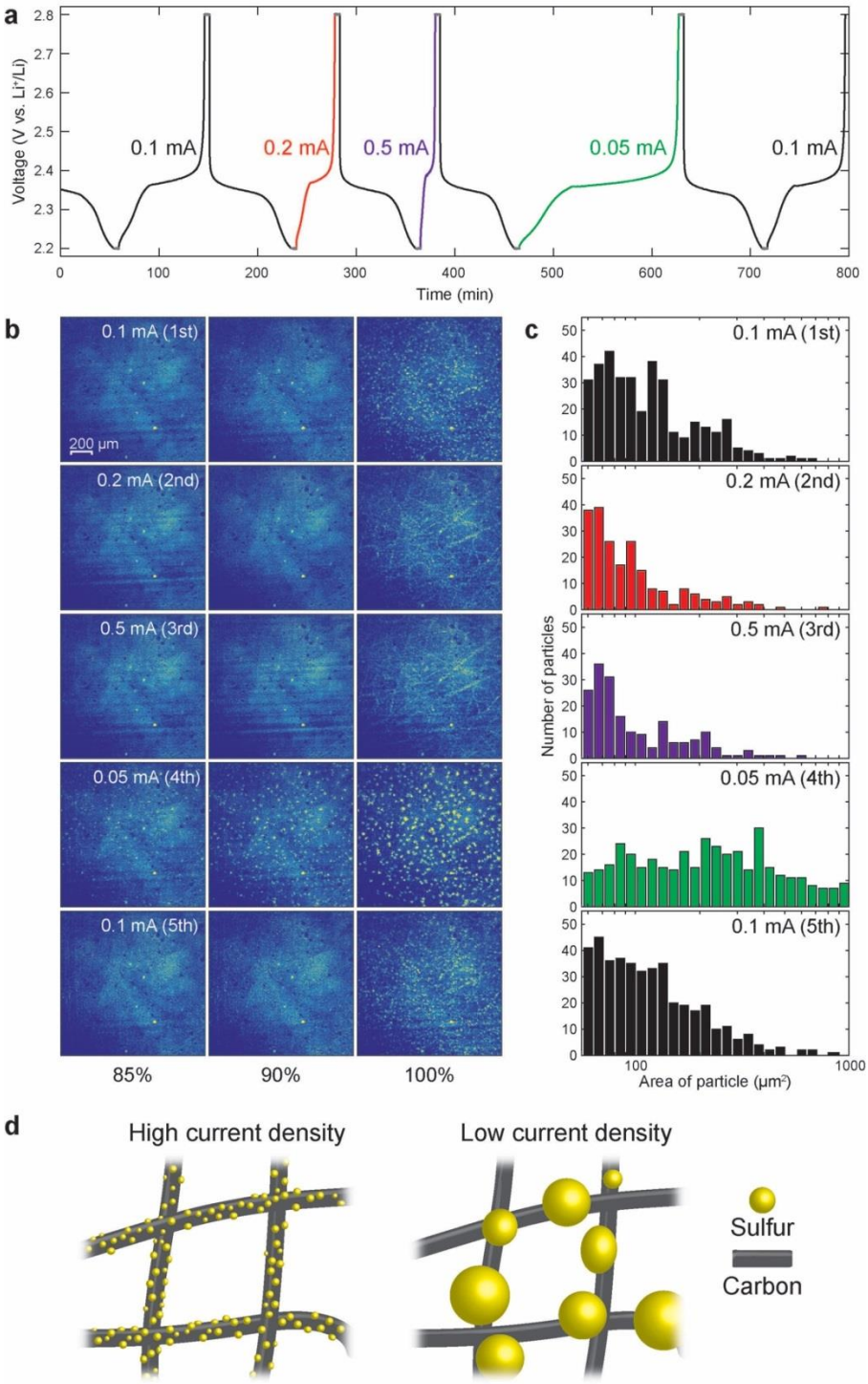

Figure 4.8 *Operando* X-ray microscopy of a lithium/polysulfide battery at different charging rates. (a) Voltage profile of lithium/polysulfide battery. The discharge rate was held constant at 0.1 mA, and charging rates were varied from 0.05 to 0.5 mA. (b)

Sequential *operando* X-ray microscopy images of the cathode at different charging rates. (c) Sulfur cluster size histograms of cathode at 100% of SOC, charged at different rates, as shown in the last column in (b). (d) Schematic picture of the morphology of sulfur clusters deposited on the carbon fibers at high and low current densities.

The effect of current density on the formation and distribution of sulfur clusters. From the above results, it is evident that the size of the sulfur clusters is strongly affected by the cycle number. In order to elucidate the effects of the current density on the formation of sulfur clusters in a single cell, we needed to mitigate (or account for) the cycle number effect. Therefore, a polysulfide catholyte, without sulfur on the electrode, was chosen, since it has been observed that a lithium/polysulfide battery can better retain capacity with cycling.[27,28] The voltage profiles of a lithium/polysulfide (Li_2S_8) cell during the first 5 cycles are shown in Figure 4.8a. While the discharging current density was held constant at 0.1 mA, the charging current density was varied between cycles. The voltage was held for 5 min at 2.2 and 2.8 V, at the end of discharge and charge, respectively. Figure 4.8b presents the XRM images of the cathode at 85%, 90% and 100% SOCs for different cycles, together with the corresponding histogram of cluster sizes at 100% SOC in Figure 4.8c. In order to better observe the effects of current density on the formation of the sulfur clusters, the absorption contrast experimental configuration was selected, since it reduces the signal from the carbon fibers, thus enhancing the signal from the sulfur clusters. As is evident in Figure 4.8b, even with the polysulfide as the starting material, the formation of sulfur clusters can be clearly observed during the charging process. Increasing the current to 0.2 and 0.5 mA for the 2nd and 3rd cycles, respectively, produced sulfur

clusters that were smaller than those formed at the lower current density of 0.1 mA. In the 4th cycle, in which the current was 0.05 mA (lowest current density employed), much larger sulfur clusters were formed. It is worth noting that the capacity delivered at the 4th cycle was comparable to that of the other cycles, indicating that the dependency of sulfur morphology on current density was not due to capacity fade. Our results suggest that the larger overpotentials, induced by the higher current densities, lead to a higher nucleation density of sulfur clusters and, therefore, the nuclei grow more uniformly on the carbon fiber, as illustrated in Figure 4.8d. After adjusting the charging current density back to 0.1 mA, at the 5th cycle, the morphology of the resulting sulfur clusters was similar to that of the 1st cycle, establishing that the size of the sulfur clusters was not influenced by the specific sequence of our experiments.

4.4 Conclusions

We have directly observed the dissolution and reformation of sulfur clusters in real time during battery operation, with *operando* XRD and XRM. The initial and final three-dimensional structure of the sulfur cathode was imaged using X-ray tomography. We find excellent agreement between crystal structure information from *operando* XRD and morphology information from XRM. The signals from XRM and XRD for sulfur dissolution and reformation also closely match each other.

We have also found that the location of reformed sulfur clusters, while independent of cycle number, is different from the initial distribution, likely reflecting the presence of specific nucleation sites on the carbon fiber current collector. Moreover, we have shown, for the first time, by comparing results from an elemental sulfur cathode and a polysulfide catholyte as the starting material, that two factors govern the size distribution of the sulfur clusters: current density and the operating

history of the cell. With a polysulfide catholyte, the main factor controlling the size of the reformed sulfur clusters is the current density, whereas with a sulfur cathode, the size of the sulfur clusters is also strongly dependent on the operating history of the cathode. From *operando* XRD, we have found that the size of the Li_2S formed is strongly dependent on the operating temperature, with smaller particles formed at lower temperatures. In addition, while the upper plateau (initial part of the discharge) was minimally influenced by temperature, the lower plateau exhibited significant changes. A preliminary analysis of the temperature dependence suggests an activation process, albeit with an upper limit. Our results expand the understanding of the reaction mechanism in Li-S batteries and demonstrate the potential of *operando* studies to unravel the complex reaction mechanisms of advanced electrode materials for electrical energy storage.

e

REFERENCES

1 Bruce, P. G., Freunberger, S. A., Hardwick, L. J. & Tarascon, J. M. Li-O_2 and Li-S Batteries with High Energy Storage. *Nature Mater.* **11**, 19-29 (2012).

2 Choi, J. W. & Aurbach, D. Promise and Reality of Post-Lithium-Ion Batteries with High Energy Densities. *Nature Rev. Mater.* **1**, 16013 (2016).

3 Dunn, B., Kamath, H. & Tarascon, J.-M. Electrical Energy Storage for the Grid: a Battery of Choices. *Science* **334**, 928-935 (2011).

4 Larcher, D. & Tarascon, J. M. Towards greener and More Sustainable Batteries for Electrical Energy Storage. *Nature Chem.* **7**, 19-29 (2015).

5 Yin, Y. X., Xin, S., Guo, Y. G. & Wan, L. J. Lithium-Sulfur Batteries: Electrochemistry, Materials, and Prospects. *Angew. Chem. Int. Ed.* **52**, 13186-13200 (2013).

6 Evers, S. & Nazar, L. F. New Approaches for High Energy Density Lithium–Sulfur Battery Cathodes. *Acc. Chem. Res.* **46**, 1135-1143 (2013).

7 Yang, Y., Zheng, G. & Cui, Y. Nanostructured Sulfur Cathodes. *Chem. Soc. Rev.* **42**, 3018-3032 (2013).

8 Manthiram, A., Fu, Y. & Su, Y.-S. Challenges and Prospects of Lithium–Sulfur Batteries. *Acc. Chem. Res.* **46**, 1125-1134 (2013).

9 Manthiram, A., Fu, Y., Chung, S. H., Zu, C. & Su, Y. S. Rechargeable Lithium-Sulfur Batteries. *Chem. Rev.* **114**, 11751-11787 (2014).

10 Ji, X., Lee, K. T. & Nazar, L. F. A Highly Ordered Nanostructured Carbon–Sulphur Cathode for Lithium–Sulphur Batteries. *Nature Mater.* **8**, 500-506 (2009).

11 Zhou, W., Yu, Y., Chen, H., DiSalvo, F. J. & Abruña, H. D. Yolk-shell Structure of Polyaniline-Coated Sulfur for Lithium-Sulfur Batteries. *J. Am. Chem. Soc.* **135**, 16736-16743 (2013).

12 Xin, S. *et al.* Smaller Sulfur Molecules Promise Better Lithium-Sulfur Batteries. *J. Am. Chem. Soc.* **134**, 18510-18513 (2012).

13 Suo, L., Hu, Y. S., Li, H., Armand, M. & Chen, L. A New Class of Solvent-In-Salt Electrolyte for High-Energy Rechargeable Metallic Lithium Batteries. *Nature Commun.* **4**, 1481 (2013).

14 Chung, W. J. *et al.* The Use of Elemental Sulfur as an Alternative Feedstock for Polymeric Materials. *Nature Chem.* **5**, 518-524 (2013).

15 Waluś, S. *et al.* Lithium/Sulfur Batteries upon Cycling: Structural Modifications and Species Quantification by In Situ and Operando X-Ray Diffraction Spectroscopy. *Adv. Energy Mater.* **5**, 1500165 (2015).

16 Nelson, J. *et al.* In Operando X-Ray Diffraction and Transmission X-Ray Microscopy of Lithium Sulfur Batteries. *J. Am. Chem. Soc.* **134**, 6337-6343 (2012).

17 Lowe, M. A., Gao, J. & Abruña, H. D. Mechanistic Insights into Operational Lithium–Sulfur Batteries by In Situ X-Ray Diffraction and Absorption Spectroscopy. *RSC Adv.* **4**, 18347 (2014).

18 Kulisch, J., Sommer, H., Brezesinski, T. & Janek, J. Simple Cathode Design for Li-S Batteries: Cell Performance and Mechanistic Insights by In Operando X-Ray Diffraction. *Phys. Chem. Chem. Phys.* **16**, 18765-18771 (2014).

19 Walus, S. *et al.* New Insight into the Working Mechanism of Lithium-Sulfur Batteries: In Situ And Operando X-Ray Diffraction Characterization. *Chem. Commun.* **49**, 7899-7901 (2013).

20 Cañas, N. A., Wolf, S., Wagner, N. & Friedrich, K. A. In-Situ X-Ray Diffraction Studies of Lithium–Sulfur Batteries. *J. Power Sources* **226**, 313-319 (2013).

21 Gorlin, Y. *et al.* Understanding the Charging Mechanism of Lithium-Sulfur Batteries using Spatially Resolved Operando X-Ray Absorption Spectroscopy. *J. Electrochem. Soc.* **163**, A930-A939 (2016).

22 Wu, H. L., Huff, L. A. & Gewirth, A. A. In Situ Raman Spectroscopy of Sulfur Speciation in Lithium-Sulfur Batteries. *ACS Appl. Mater. Interfaces* **7**, 1709-1719 (2015).

23 Yu, X. Q. *et al.* Direct Observation of the Redistribution of Sulfur and Polysufides in Li-S Batteries during the First Cycle by In Situ X-Ray Fluorescence Microscopy. *Adv. Energy Mater.* **5**, 1500072 (2015).

24 Kim, K. R., Yu, S. H. & Sung, Y. E. Enhancement of Cycle Performance of Li-S Batteries by Redistribution of Sulfur. *Chem. Commun.* **52**, 1198-1201 (2016).

25 Ren, Y. X., Zhao, T. S., Liu, M., Tan, P. & Zeng, Y. K. Modeling of Lithium-Sulfur Batteries Incorporating the Effect of Li_2S Precipitation. *J. Power Sources* **336**, 115-125 (2016).

26 Son, Y., Lee, J.-S., Son, Y., Jang, J.-H. & Cho, J. Recent Advances in Lithium Sulfide Cathode Materials and Their Use in Lithium Sulfur Batteries. *Adv. Energy Mater.* **5**, 1500110 (2015).

27 Fu, Y., Su, Y. S. & Manthiram, A. Highly Reversible Lithium/Dissolved Polysulfide Batteries with Carbon Nanotube Electrodes. *Angew. Chem. Int. Ed.* **52**, 6930-6935 (2013).

28 Zhou, G., Paek, E., Hwang, G. S. & Manthiram, A. Long-life Li/Polysulphide Batteries with High Sulphur Loading Enabled by Lightweight Three-Dimensional Nitrogen/Sulphur-Codoped Graphene Sponge. *Nat. Commun.* **6**, 7760 (2015).

CHAPTER 5

NEW INSIGHTS IN THE GROWTH MECHANISM OF LI DENDRITE THROUGH *OPERANDO* X-RAY IMAGING

5.1 Introduction

Lithium-ion batteries have been considered as the main and ideal power sources for electrical vehicles and portable electronic devices such as laptops and smartphones over 2 decades.[1] However, due to the world-wide increase in power consumption, it will become urgent to develop new high capacity electrodes. Among all the anode materials, lithium metal is an attractive choice, because it offers a very high specific capacity of 3860 mAh/g, which is more than 10 times larger than that of the state-of-art graphite anode, as well as the lowest reaction voltage.[2,3] Thus, a lithium metal anode is an essential component of most post-lithium ion battery systems, such as lithium-air and lithium-sulfur batteries.[4] However, for lithium metal anode, there exist several barriers, such as the low Coulombic efficiency and, more severely, the dendritic growth of lithium on the surface of the electrode during the plating, which can lead to the thermal runaway and even catastrophic explosion.[3,5,6]

Although there have been numerous studies focusing on materials structure modification to prevent dendrite formation,[7-11] the mechanism for dendritic growth is still not well understood. In this work, we applied *operando* X-ray imaging (XRI) to visualize the growth and dissolution of dendrites, under various conditions. The dynamics of dendritic growth was clearly observed and we have been able to establish the relationship between the morphology of the dendrite and current density, concentration, electrolyte and additives.

5.2 Methods and materials

Electrolyte: The electrolytes 1.0 M $LiPF_6$ in EC/DEC (1:1 volume ratio), 1.0 M $LiPF_6$ in PC and 1.0 M LiTFSI in DOL/DME (1:1 volume ratio) were used as received. Electrolytes with different concentrations of $LiPF_6$ (0.5 M, 0.1 M, 0.05 M and 0.02 M) in EC/DEC were prepared by diluting 1.0 M $LiPF_6$ in EC/DEC with the appropriate amount of EC and DEC. For the electrolytes 1.0 M $LiPF_6$ in PC with 5 wt% FEC and 1.0 M LiTFSI in DOL/DME with 0.2 M $LiNO_3$, 5wt% of FEC (fluoroethylene carbonate) and 0.2 M of $LiNO_3$ was directly added into the electrolyte. For the electrolyte 1.0 M $LiPF_6$ in PC with 0.05 M $CsPF_6$, we employed two methods for preparation. In the first method, we directly added $CsPF_6$ (Synquest Laboratory) into a 1.0 M $LiPF_6$ in PC solution. In the second, CsI (Aldrich) and $AgPF_6$ (Aldrich) solution in PC were combined and then precipitated AgI was filtered using a syringe filter (0.45 um). Subsequently, 1.0 M $LiPF_6$ was added to the prepared solution.

***Operando* X-ray imaging:** *Operando* XRI was performed at the F-3 station of CHESS using an incident X-ray energy of 10.0 keV. Images were collected using a Scintillator-coupled Andor camera (Neo 5.5 sCMOS), with a resolution of about 2 μm. The distance between the sample and detector was 11 cm. The Lithium metal was loaded with homemade holder. Two lithium loaded holders were further mounted into a 2032-type coin cell with a 3mm diameter hole at the center. Two holders were electrically connected to one side of the coin cell electrode respectively, and the lithium sides were inside the X-ray window.

5.3 Results and discussion

Figure 5.1a presents the schematic of the experimental setup for the X-ray microscopy of lithium dendrite growth with a symmetry cell. Two metal (Ti) plates were applied

to dip lithium metal on the very end as electrodes. With this setup, the X-ray images were taken in *operando* condition during the Li dendrite growth (at ~2 mA/cm^2 in the electrolyte of 1.0 M $LiPF_6$ dissolved in EC/DEC), as shown in Figure 5.1b. To better show the evolution of the morphology of individual dendrite, a selected area from Figure 5.1b at different growth time are displayed in Figure 5.1c. One can clearly observe that the mossy-like dendrites grow over the time[12], with the diameter of single dendrite less than 10 μm. Our results, for the first time, show more clearly the explicit structure of dendrite over the large region and, more importantly, with absorption of X-ray, the amount of the Li in the dendrite could be quantified. From the evolution of the explicit structure of dendrite, it is clearly shown that the dendrite grows mostly from top layer and the growth of the rest of dendrites slows down (Note that this does not mean the individual dendrite grows at the tip. The growth of dendrite in the top layer still follows bulk growth.), which is confirmed with the transient of total X-ray intensity within certain distances from the surface of electrode, showing that the dendrites under the top region become saturated over the growth.

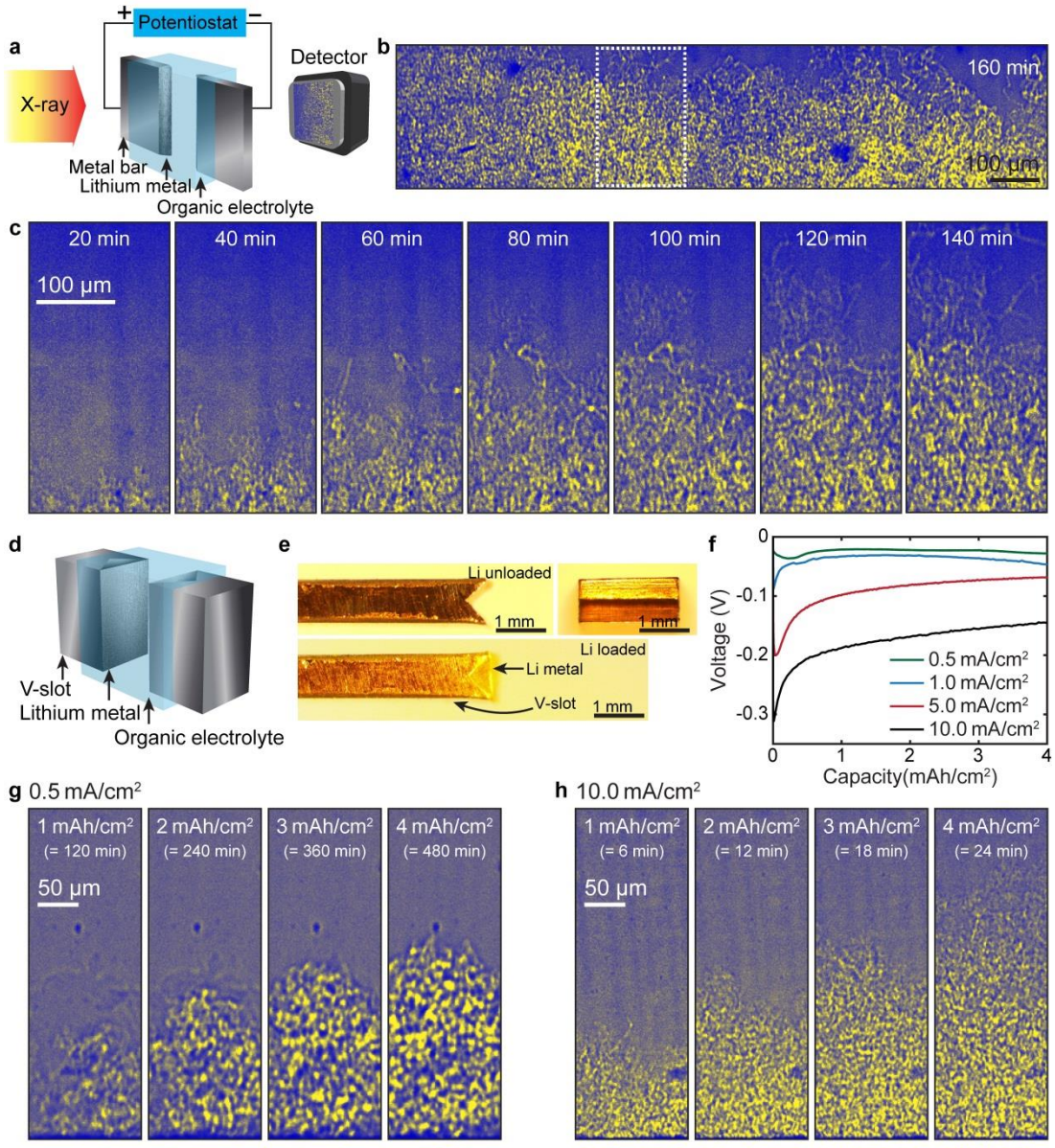

Figure 5.1. (a) Experimental setup for *operando* X-ray imaging with metal bars as Li holders. (b) X-ray imaging of Li dendrite growth at ~2 mA/cm^2 in 1 M $LiPF_6$ dissolved in EC/DEC electrolyte. (c) Images of dendrites in selected area (dotted box) in b at different times. (d) Experimental setup with V-slot Li holder. (e) Optical microscopy of V-slot before and after Li loading. (f) Voltage profiles of Li dendrite

growth at different current rates. (g), (h), Images of Li dendrite grown at (g) 0.5 and (h) 10.0 mA/cm^2.

It would be expected that the morphology of dendrites and their evolution would be affected by various factors[13-15]. In order to systematically study some of the variables that could affect dendrite growth, it is essential to precisely control areal current density[15]. However, with the setup in Figure 5.1a, we could only approximate the surface area of the lithium electrode. So as to better control the areal current density, we designed a "V-slot" Li holder which could be used to load Li, as illustrated in Figure 5.1d. Figure 5.1e presents optical microscopy images of the V-slot holder, before and after loading with Li metal. With the V-slot, Li dendrite growth at different current densities could be compared. Four different current densities, from 0.5 to 10.0 mA/cm^2, were applied and the voltage profiles were presented in Figure 5.1f. The voltage profiles show a similar trend: the voltage first reaches a maximum, due to the nucleation, and then gradually decreases, because of the increase of total surface area by forming dendrites. Figures 5.1g and h show the dendrites grow at 0.5 and 10 mA/cm^2, respectively. These values were selected because the current densities ranging from 0.5 to 10 mA/cm^2 are expected to be most relevant to practical applications and have been frequently employed in the literature.[15] It is clear that with this range, Li dendrites have a mossy-like morphology. However, the size of individual dendrites, grown at 0.5 mA/cm^2, is bigger than that of dendrites grown at 10.0 mA/cm^2, and the number of individual dendrites is smaller. The morphology change, induced by the current density, might be due to the competition of two reactions: the formation of dendrites and SEI formation. At low current densities, a thicker SEI layer was formed to accommodate dendrite expansion, whereas at high

current densities, SEI layer was not thick enough and was easier to break during the expansion of lithium. As a result, new lithium branches were more easily formed. This explanation is also supported by the voltage profile. At high current densities, the voltage quickly decreased, after reaching the maximum value, compared with that at 0.5 mA/cm^2, since the surface area increased rapidly by forming new lithium branches at high current densities.

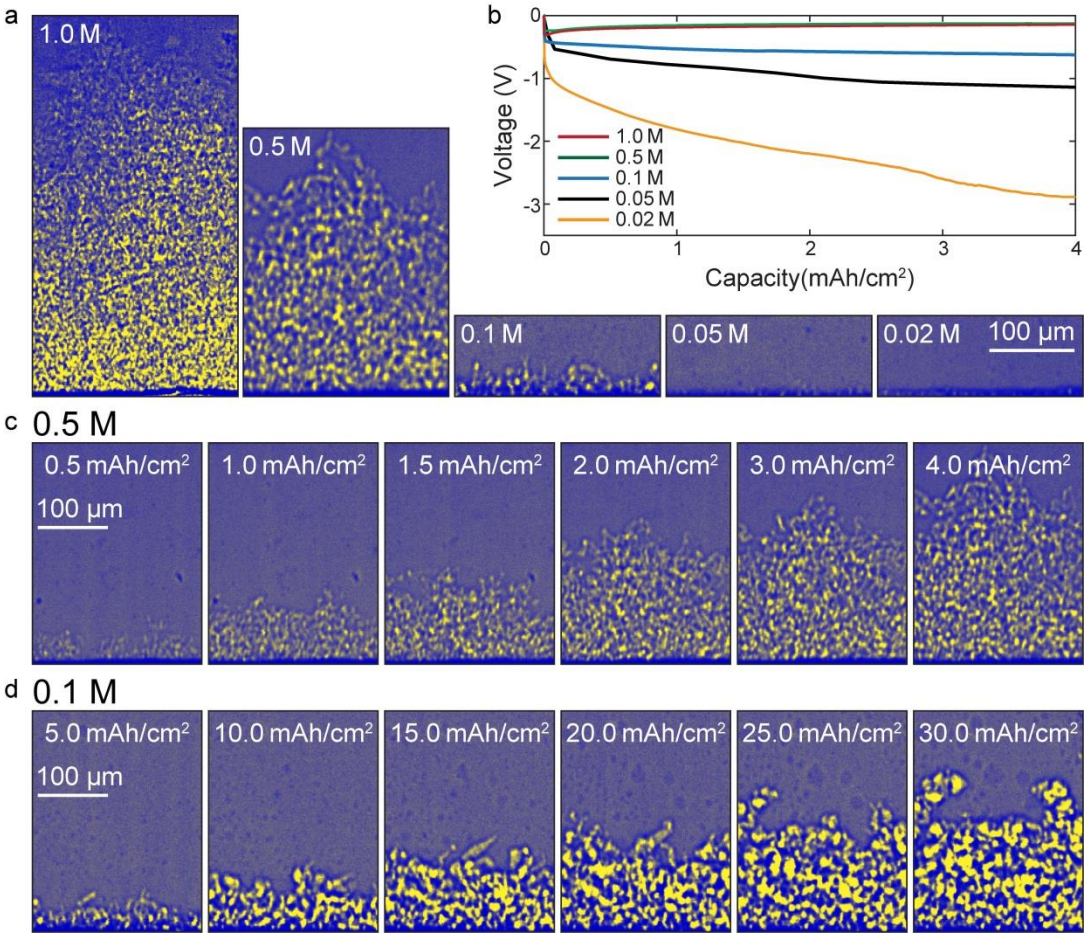

Figure 5.2. (a) Images of dendrite grown at the specific capacity of 4 mAh/cm^2 in EC/DEC containing different concentration of $LiPF_6$. (b) Voltage profiles of dendrite growth. (c), (d) Images of dendrite grown in ECDEC with (c) 0.5 M and (d) 0.1M of $LiPF_6$.

In order to evaluate the effects of the concentration of the lithium salt, lithium dendrite growth using 1.0, 0.5, 0.1, 0.05 and 0.02 M of $LiPF_6$ were conducted, and results are shown in Figure 5.2. Figure 5.2a shows the morphology of the dendrites at the specific capacity of 4 mAh/cm^2. At 0.5 M and 1.0 M, a similar morphology of dendrites was observed, but both the size of individual dendrites and pore size increased, with the total height of the dendrites decreased. At lower concentrations, this trend became stronger, with the height of the dendrites decreasing even more. The corresponding voltage profiles are shown in Figure 5.2b. The profiles are clearly divided into two groups. At 1.0 M and 0.5 M concentration, the profiles almost overlap, and the voltage decreases rapidly after reaching the maximum; similar to Figure 5.1f. However, when the concentration was 0.1 M or lower, the voltage profiles keep increasing monotonically. With lower concentration, the voltage became higher. To further characterize the voltage profile changes between 0.5 M and 0.1 M, we compare the evolution of dendrites growing at 0.5 M and 0.1 M, which are shown in Figures 5.2c and d, respectively. At a concentration of 0.1 M, the morphology of the dendrites is clearly different from mossy. The size of individual dendrites increased, and even some spherically shaped dendrites were formed. The morphology change in the dendrites was affected by many factors, and it is difficult to separate the specific effects. However, one dominant cause of the change in the morphology is the competition between SEI formation and dendrite growth. The composition and growth rate of the SEI layer are influenced by the concentration and voltage. At lower concentrations, a more negative voltage is needed to be applied in order to maintain the same current density, which makes the electrolyte easier to decompose and form more of an SEI layer to accommodate the dendrite growth. As a result, the dendrite becomes more dense and closely packed, rather than forming many branches.

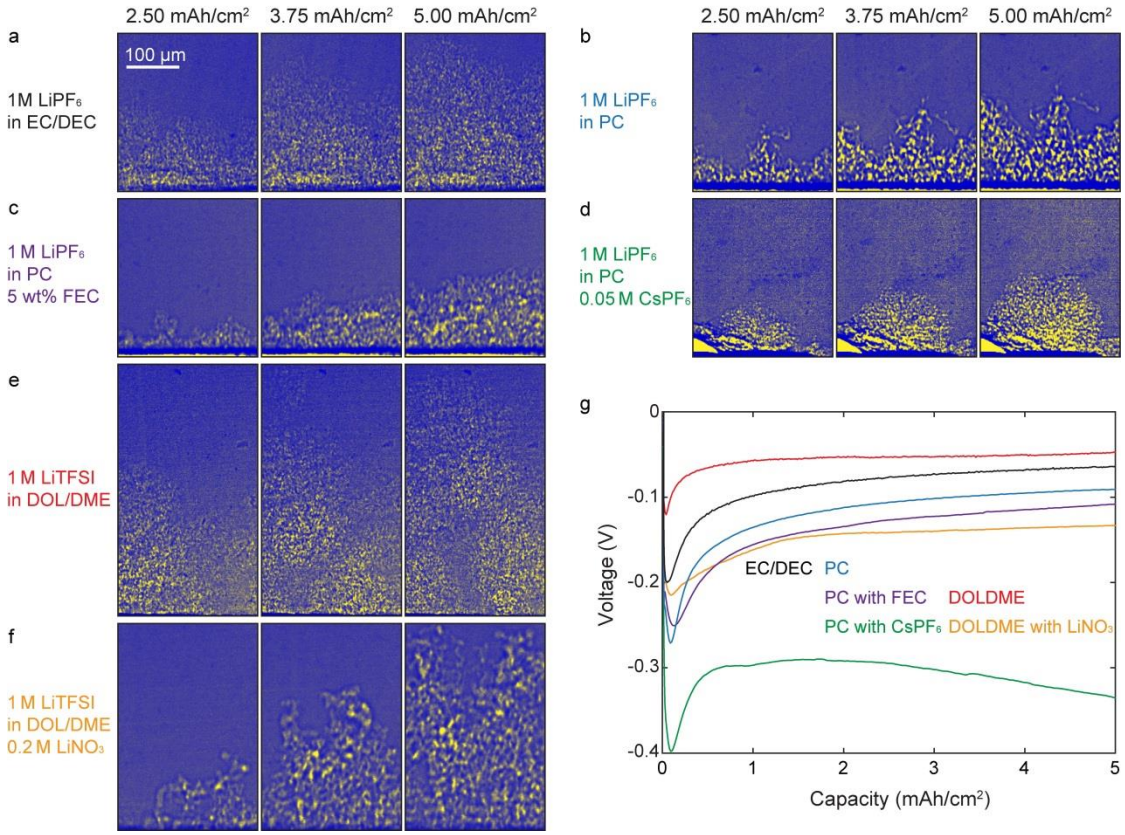

Figure 5.3. (a)-(f) Images of dendrite grown in different electrolytes at the specific capacity of 5 mAh/cm^2. (g) Corresponding voltage profiles.

Figure 5.3 compares the growth of dendrites in different electrolytes and additives. As mentioned previously, the shape of the dendrites is mossy-like in 1.0 M $LiPF_6$ in EC/DEC. 1.0 M $LiPF_6$ in PC is also one of the most commonly used carbonate-based electrolytes for Li-ion and Li metal batteries. Interestingly, by simply changing the solvent, the morphology of the dendrites is clearly changed, forming larger individual dendrites with sharp edges. By adding additives, such as 5wt% FEC, the sharp edges of the individual dendrites become "blurry". When using 0.05 M $CsPF_6$ as additive, dendrite growth is significantly delayed, and once dendrites start forming, they only

grow at some local positions, while on the other regions of the electrode surface, no dendrite growth was observed. The growth of dendrites is from the electrode surface (root growth), and form a semi-spherical shape. When replacing the electrolyte to an ether based electrolyte, DOL/DME, the morphology of the dendrites is similar to that in EC/DEC, but they are "taller", indicating that more branches were formed. A strong morphology change happens, with adding 0.2 M $LiNO_3$, in which the individual dendrites become larger. Figure 5.3g shows the corresponding voltage profiles. By combining these results, a general trend is observed, relating the maximum value of the overpotential to dendrite growth. In general, higher overpotentials generate larger individual dendrites. For example, in the DOL/DME electrolyte with and without $LiNO_3$ as additive, the voltage changes from -0.12 V to -0.215 V. Meanwhile, the size of individual dendrites increased significantly.

5.4 Conclusions

With a novel experimental setup for *operando* X-ray imaging to observe lithium plating/striping, we have systematically studied and compared effects of the growth conditions on the resulting morphology. The dynamics of dendrite growth was clearly observed and the morphology of the dendrites shows strong dependences on current density, concentration, electrolyte and additives. At higher current rates, the morphology of the lithium dendrites trends to be mossy-like. With a decrease in the current rate, the individual dendrites become larger, and form less branches. Similarly, a decrease in the concentration of the lithium salts gives rise to larger individual dendrites. Although PC is a carbonate electrolyte, as is EC/DEC, the dendrites grown in PC are larger than that in EC/DEC under the same conditions. After adding $CsPF_6$, the dendrite growth becomes extremely inhomogeneous, rather than growing over the

entire surface of the electrode, the dendrites only grow at some local positions. Once the dendrite starts to form, it grows rapidly. In DOL/DME, the morphology is similar to that in EC/DEC. However, significant morphology changes occur when adding $LiNO_3$ additives, giving rise to the largest individual dendrites, when compared to all other conditions.

REFERENCES

1 Nagaura, T. & Tozawa, K. Lithium Ion Rechargeable Battery. *Prog. Batteries Solar Cells* **9**, 209, (1990).

2 Zhang, K., Lee, G.-H., Park, M., Li, W. & Kang, Y.-M. Recent Developments of the Lithium Metal Anode for Rechargeable Non-Aqueous Batteries. *Adv. Energy Mater.* **6**, 1600811, (2016).

3 Xu, W. *et al.* Lithium Metal Anodes for Rechargeable Batteries. *Energy Environ. Sci.* **7**, 513-537, (2014).

4 Bruce, P. G., Freunberger, S. A., Hardwick, L. J. & Tarascon, J. M. Li-O_2 and Li-S Batteries with High Energy Storage. *Nat. Mater.* **11**, 19-29, (2012).

5 Zhamu, A. *et al.* Reviving Rechargeable Lithium Metal Batteries: Enabling Next-Generation High-Energy and High-Power Cells. *Energy Environ. Sci.* **5**, 5701-5707, (2012).

6 Chandrashekar, S. *et al.* ^{7}Li MRI of Li Batteries Reveals Location of Microstructural Lithium. *Nat. Mater.* **11**, 311-315, (2012).

7 Lu, D. *et al.* Failure Mechanism for Fast-Charged Lithium Metal Batteries with Liquid Electrolytes. *Adv. Energy Mater.* **5**, 1400993-n/a, (2015).

8 Qian, J. *et al.* High Rate and Stable Cycling of Lithium Metal Anode. **6**, 6362, (2015).

9 Zheng, G. *et al.* Interconnected Hollow Carbon Nanospheres for Stable Lithium Metal Anodes. *Nat. Nano.* **9**, 618-623, (2014).

10 Yang, Y. *et al.* High-Capacity Micrometer-Sized Li2S Particles as Cathode Materials for Advanced Rechargeable Lithium-Ion Batteries. *J. Am. Chem. Soc.* **134**, 15387-15394, (2012).

11 Lin, D. *et al.* Layered Reduced Graphene Oxide with Nanoscale Interlayer Gaps as A Stable Host for Lithium Metal Anodes. *Nat. Nano.* **11**, 626-632, (2016).

12 Wood, K. N. *et al.* Dendrites and Pits: Untangling the Complex Behavior of Lithium Metal Anodes through Operando Video Microscopy. *ACS Cent. Sci.* **2**, 790-801, (2016).

13 Ding, F. *et al.* Dendrite-Free Lithium Deposition via Self-Healing Electrostatic Shield Mechanism. *J. Am. Chem. Soc.* **135**, 4450-4456, (2013).

14 Bai, P., Li, J., Brushett, F. R. & Bazant, M. Z. Transition of Lithium Growth Mechanisms in Liquid Electrolytes. *Energy Environ. Sci.* **9**, 3221-3229, (2016).

15 Wood, K. N., Noked, M. & Dasgupta, N. P. Lithium Metal Anodes: Toward an Improved Understanding of Coupled Morphological, Electrochemical, and Mechanical Behavior. *ACS Energy Lett.* **2**, 664-672, (2017).

CHAPTER 6

CONCLUSIONS

6.1 Summary

In this thesis, we have demonstrated the capability of synchrotron X-ray techniques to characterize the atomic-scale structure and properties of the active materials in energy conversion and storage systems via four projects. In the first two projects, *operando* CTR measurements were applied to study the surface and bulk structure of catalysts for photo-electrochemical and fuel cells, respectively, under catalytic conditions. In the last two projects, *operando* X-ray imaging was applied to investigate microstructure evolution in the two essential components of beyond lithium ion batteries: sulfur cathodes and lithium metal electrodes. In this thesis, I have :

1. Determined the surface structure of $SrTiO_3$ in the photo-assisted water splitting condition, and established a link between surface structure and catalytic activity.
2. Determined the structure of $Pb_2Ru_2O_{6.5}/Sm_2Ti_2O_7$ thin films (a catalyst for oxygen electrocatalysis) and discovered a reversible structural reconstruction that deforms the RuO octahedral in $Pb_2Ru_2O_{6.5}$ present under oxygen reduction reaction conditions.
3. Observed the evolution of the morphology of sulfur particles as batteries cycled and discovered the factors that determine the size of both sulfur and Li_2S particles.
4. Observed the growth and dissolution of lithium dendrites on lithium metal electrodes and studied the relationship between the morphology of lithium

dendrites and the operating conditions: current rate, electrolyte composition, and chemical additives.

These experimental results expand our fundamental understanding of the reaction mechanisms involved with active energy materials. I hope this thesis will provide the framework necessary to continue to unravel the complex reaction mechanisms of advanced active materials in energy conversion and storage systems.

6.2 Outlook

First, although synchrotron X-ray techniques have been applied to electrochemical system for more than two decades, the capabilities of synchrotron X-ray techniques keeps increasing rapidly, due to continuous upgrades of synchrotron facilities worldwide, providing brighter, faster, better collimated, more coherent, X-ray sources. These enhances facilities will revolutionize X-ray methods and how they can be applied to study energy systems. For example, in chapter 2, we have characterized how the surface structure of $SrTiO_3$ is altered by the electrochemical training. So far, we have only measured the initial and final structures, we have not yet observed the reconstruction process. With the upgrades, it is expected that the time to perform CTR measurements will be greatly reduced, so that we will be able to characterize the intermediate structure to understand the dynamics of the structure evolution

Second, nowadays it becomes a trend that multiple *operando* X-ray techniques are coupled together to unravel the structure of the materials at multiple scales simultaneously. For example, in chapter 4, we have measured the microstructure change of sulfur particles during the battery operation with X-ray imaging in F-3 station, and later measured the crystal structure of sulfur and Li_2S with X-ray

diffraction in A-1 station. Theoretically, these two techniques could be coupled and the measurement could be conducted simultaneously.

Third, we selected only a few materials/systems in our experiment to observe the structure evolution both irreversibly and reversibly with the operating condition. To completely understand the link between the structure and functionality, it is necessary to explore more materials with similar structure. For example, in chapter 3, we discovered the structure of $Pb_2Ru_2O_{6.5}$ has a reversible structure that basically deforms the RuO octahedral, changing the bond length between Ru and O, in the ORR condition. It is reported that the catalytic properties in pyrochlore catalysts are correlated with the B-O bond length. So it is natural to investigate whether a similar RuO octahedral deformation will occur in the other RuO based materials. Additionally, in some of our X-ray experiments (such as the lithium dendrite growth studies in Chapter 5), we used the most basic electrochemical setup running with the most commonly used conditions, in order to generalize our findings and explain the most well-known phenomena. In fact, there are lots of modifications to the system, such as controlling the initial morphology of the electrode, that are known to significantly improve performance. In principle, X-ray imaging techniques could be applied to the modified systems to understand the origin of the improvements of performance.

APPENDIX A
RELAXATION OF ASYMMETRIC CRYSTALLOGRAPHIC TILT: *IN SITU* X-RAY DIFFRACTION STUDIES OF EPITAXIAL ELECTRODEPOSITION OF BISMUTH ON GAAS (110)

A.1 Introduction

Mechanisms to deal with the long-range stress field generated by lattice mismatch between film and substrate are critically important to heteroepitaxial growth and have been studied extensively.[1] One possible mechanism is simply to strain the pseudomorphic film. In this case, the film typically exhibits a critical thickness, beyond which the film relaxes via the creation of misfit-dislocations.[2] A second possible mechanism to relieve the strain energy is to create a low-energy tilt boundary (a coherent, periodic distribution of edge dislocations) at the substrate-film interface, reducing the lattice mismatch and, therefore, the long-range strain fields.[3-5] (The tilt boundary is called asymmetric if the two lattices have different tilts relative to the interface.) Significant efforts, both experimental and theoretical,[6-10] have been made to understand asymmetric tilt boundaries and to use them to grow strain-free films.[11] Despite the effort, the detailed structure and strain relaxation mechanism of asymmetric tilt boundaries at heteroepitaxial interfaces remains poorly understood.

Hexagonal lattice metals on cubic substrates were some of the first epitaxial systems in which lattice tilt was observed.[12-14] Tilted $(01\bar{1}L)_{HEX}$ epitaxial films exhibit two common features. First, they have the same tilt axis $[2\bar{1}\bar{1}0]$. (In hexagonal close packing metal films, the equivalent plane $(10\bar{1}L)$ and tilt axis $[1\bar{2}10]$ are usually used.[14]) Second, the tilt is caused by a slip of the (0001) basal plane at the interface. Bismuth films, for example, show a strong $(01\bar{1}8)$ texture when grown on GaAs(110),

which follows the $(01\bar{1}L)$ growth rule (See Figure A.1a).[15,16] Moreover, because bismuth exhibits high magnetoresistance,[17,18] has a long mean free path,[19,20] and the interface between bismuth and GaAs forms a Schottky barrier that prevents electrical leakage from the bismuth film into GaAs,[15,16,21] bismuth films on GaAs are attractive candidates for spintronic devices.[22-24] Therefore, we chose bismuth electrodeposition on GaAs(110) as a model system in which to study asymmetric tilt and its relaxation mechanism.

To monitor in real-time the structure of bismuth films during electrodeposition, we used *in situ* high-energy x-ray diffraction. Combining high energy x-rays (~30 keV) and a large area detector, we simultaneously monitored several Bragg reflections during electrodeposition under various deposition conditions with sufficient angular resolution to resolve the peak width both normal to the Ewald sphere.[25]

A.2 Electrochemical characterization of the system Bi^{3+}/GaAs(110)

An electrochemical characterization of the system Bi^{3+}/GaAs(110) was carried out using cyclic voltammetry (CV), with Ag/AgCl as the reference electrode (RE). We measured several consecutive scans starting at the open circuit potential (OCP ~ 100 mV vs. RE) and examining first the reduction processes. Then the potential is reversed at -200 mV vs. RE towards positive values up to 300 mV vs. RE to completely dissolve the electrodeposited bismuth. Finally, the potential is returned to the OCP. We varied the sweep rate to explore the changes in both cathodic and anodic regions. The CVs (Figure A.1b) present a cathodic and an anodic peak that correspond respectively to the deposition and dissolution of bismuth. The charge accumulated during both process only differs in a 5% for the CVs studied. When increasing the sweep rate, the cathodic peak moves to more negative value, while the anodic peak

position shifts towards positive direction. This is a signature of the irreversibility of the Bi/Bi^{3+} redox couple in this particular electrolyte due to the sluggish electron exchange[26,27]. The onset potential for bismuth deposition, obtained from the slowest sweep potential (5 mV/s), is about -60 mV vs. RE. Since the equilibrium potential for Bi^{3+}/Bi at this concentration and at room temperature is approximately 40 mV vs. RE, we can conclude that a minimum overpotential of η=100 mV is needed to nucleate bismuth onto the surface of GaAs(110).

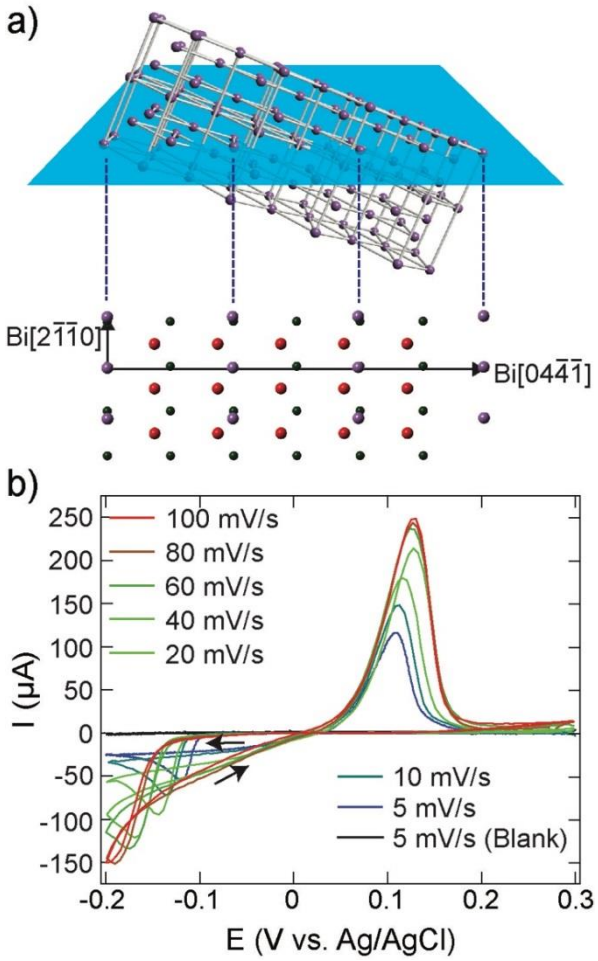

Figure A.1. (a) Scheme of the orientation of bismuth (0 1 $\bar{1}$ 8) domain (top), and the overlap between bismuth (0 1 $\bar{1}$ 8) and GaAs (110) plane (bottom). Purple represents

Bi atom, green for Ga and red for As. The blue plane indicates the (0 1 $\bar{1}$ 8) plane. (b) Cyclic voltammograms of Bi^{3+}/GaAs(110) at different sweeping rates. The arrow marks the sweeping direction.

A.3 In situ X-ray diffraction during the Bi film growth

The crystal structure of the bismuth film grown under the chronoamperometry at various overpotentials was characterized using *in situ* XRD with a custom electrochemical cell (Figure A.2a)[28]. The measurements were performed in the A2 station of the Cornell High Energy Synchrotron Source (CHESS). The X-ray energy was 30 keV and the diffracted X-rays were collected by a 41 cm × 41 cm large area detector (DXR250RT, GE Inspection Technologies), which covered an area in reciprocal space as large as 34 /Å^2. The substrate was aligned so that the projection of the incoming X-ray wavevector on the sample surface was along $[\bar{1}10]_{GaAs}$, which is parallel to the asymmetric tilt axis $[2\bar{1}\bar{1}0]_{Bi}$ in (0 1 $\bar{1}$ 8) texture.

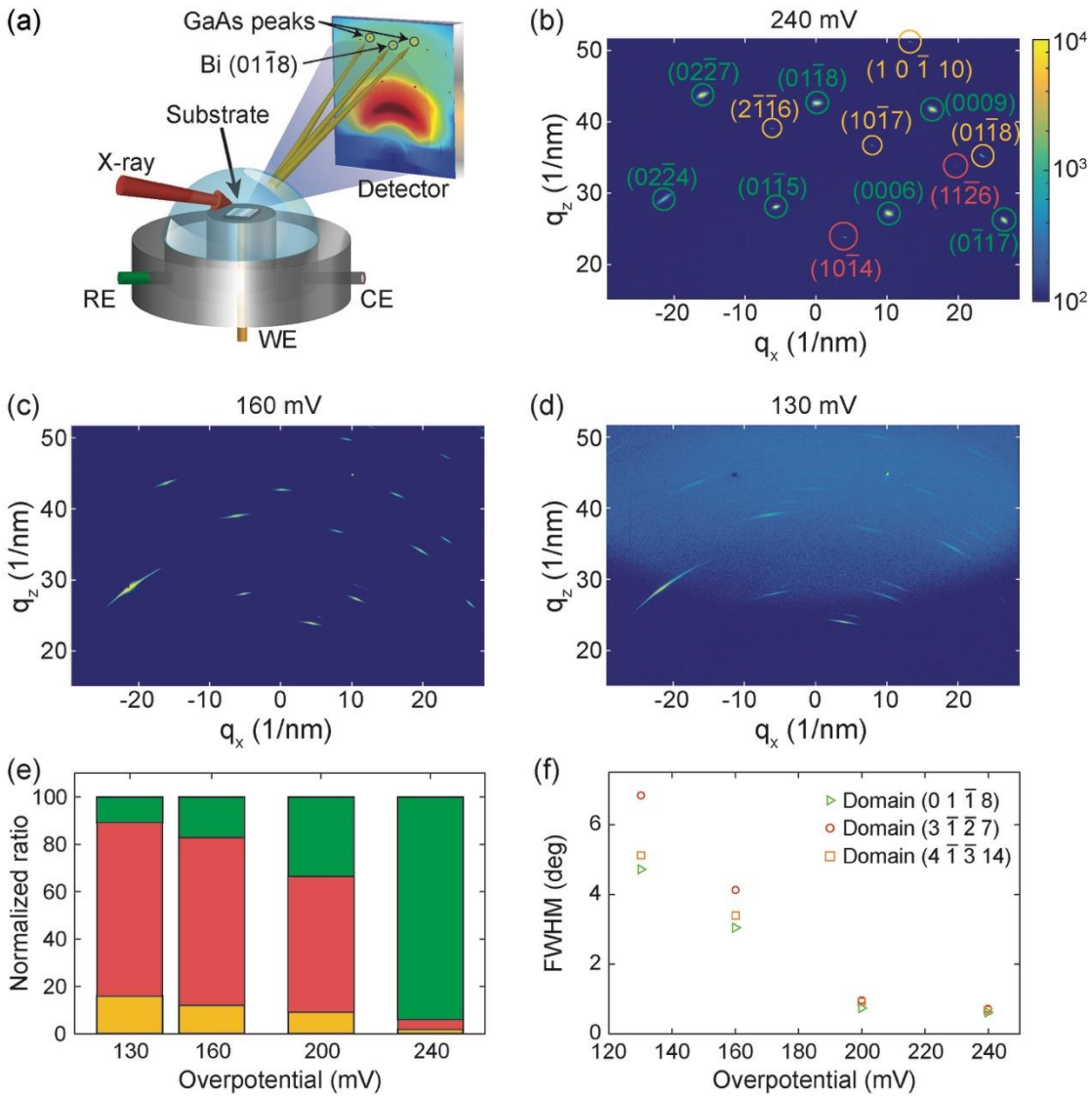

Figure A.2. (a) The schematic image of the *in situ* XRD experimental setup. Background subtracted XRD patterns of bismuth films deposited under the overpotential of (b) 240 mV, (c) 160 mV and (d) 130 mV. The color map is in logarithmic scale. The diffractions from every domain in (b) are marked with a distinctive color: (0 1 $\bar{1}$ 8) in green, (4 $\bar{1}$ $\bar{3}$ 14) in orange and (3 $\bar{1}$ $\bar{2}$ 7) in red. (e) The normalized intensity ratio of diffractions of three domains at different overpotentials. The green bar is for (0 1 $\bar{1}$ 8) domain, yellow for (4 $\bar{1}$ $\bar{3}$ 14) and red for (3 $\bar{1}$ $\bar{2}$ 7). (f)

The mean value of the angular FWHM of the diffractions in $(0\ 1\ \bar{1}\ 8)$ domain (green triangles, except $(02\bar{2}4)$), $(3\ \bar{1}\ \bar{2}\ 7)$ domain (red circles) and $(4\ \bar{1}\ \bar{3}\ 14)$ domain (orange squares), at different overpotentials.

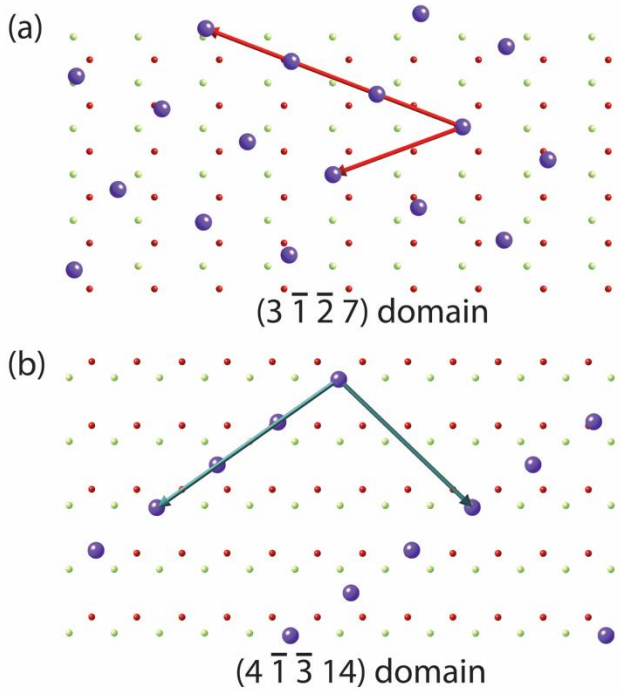

Figure A.3 (a) The in plane orientation of $(3\ \bar{1}\ \bar{2}\ 7)$ domain and (b) $(4\ \bar{1}\ \bar{3}\ 14)$ domain overlapping with $(110)_{GaAs}$ plane.

Figure A.2b to d is the background-subtracted XRD patterns of bismuth films deposited for 30 minutes at different overpotentials. Diffraction peaks were indexed calculating its corresponding interplanar distances and classified, taking into account their calculated relative orientation, into three different single crystal domains: $(0\ 1\ \bar{1}\ 8)$, $(4\ \bar{1}\ \bar{3}\ 14)$ and $(3\ \bar{1}\ \bar{2}\ 7)$. The in-plane orientations of the $(4\ \bar{1}\ \bar{3}\ 14)$ and $(3\ \bar{1}\ \bar{2}\ 7)$ domains are shown in Figure A.3. In Figure A.2b, the diffraction peaks from

every domain are marked with a distinctive color: green, yellow and red respectively. No other diffractions were clearly visible in the performed experiments. Although the $(4\,\bar{1}\,\bar{3}\,14)$ and $(3\,\bar{1}\,\bar{2}\,7)$ domains are present and coexist with $(0\,1\,\bar{1}\,8)$ domain throughout our potential window, the relative growth rate to that of $(0\,1\,\bar{1}\,8)$ domain can be significantly reduced with the overpotential. Figure A.2e shows the abundance of each domain as a function of the overpotential. To estimate the growth rate between domains, we average the integrated intensity of all diffractions from each domain. The green, red and yellow bars represent the abundance percentage of $(0\,1\,\bar{1}\,8)$, $(4\,\bar{1}\,\bar{3}\,14)$ and $(3\,\bar{1}\,\bar{2}\,7)$ domains. From this figure, we infer that increasing the overpotential promotes the $(0\,1\,\bar{1}\,8)$ over the two other orientations. The abundance of this domain rapidly grows from 11% to 94%, while the $(3\,\bar{1}\,\bar{2}\,7)$ domain decreases from more than 73% down to 4% and the $(4\,\bar{1}\,\bar{3}\,14)$ domain decreases from 16% at low overpotential to just 2% at high overpotential.

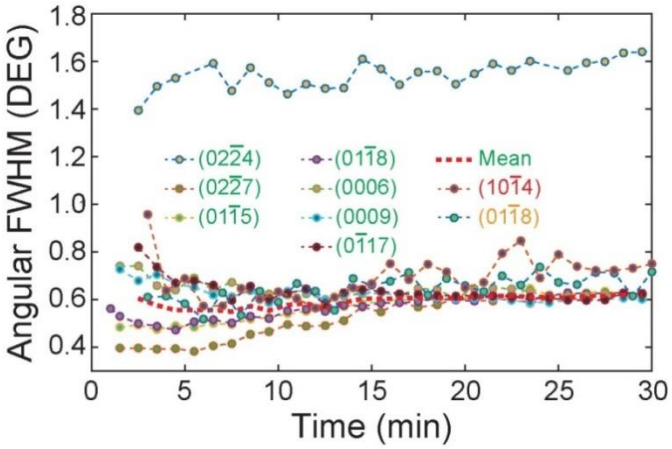

Figure A.4. Angular FWHM of several diffractions from the three domains at the overpotential of 240 mV.

Moreover, increasing the overpotential significantly reduces the mosaicity in the film. As shown earlier in Figure A.2b to d, the diffraction from domains in bismuth exhibits an angular distribution along the corresponding Debye-Scherrer ring trajectories, of which the full width at half maximum (FWHM) can be used to characterize mosaicity of the film. The mosaicity as a function of the overpotential is shown in Figure A.2f. Green triangles in the figure are the averaged FWHM of peaks from $(0\,1\,\bar{1}\,8)$ domains as a function of overpotential. At low overpotential, the averaged FWHM is about $4.71°$, whereas at the highest overpotential, it decreases down to $0.62°$, a $7\times$ decrease in mosaicity by increasing the overpotential. When we analyzed the other two domains, we also obtained a similar decrease in the FWHM with increasing overpotential (red circles and orange squares in Figure A.2f). However, it is worth noting that this difference in the mosaicity between different overpotentials is not simply caused by the thickness of the film, because the average value of angular FWHM of Bi peaks does not depend on the film thickness (see red dashed line in Figure A.4a).

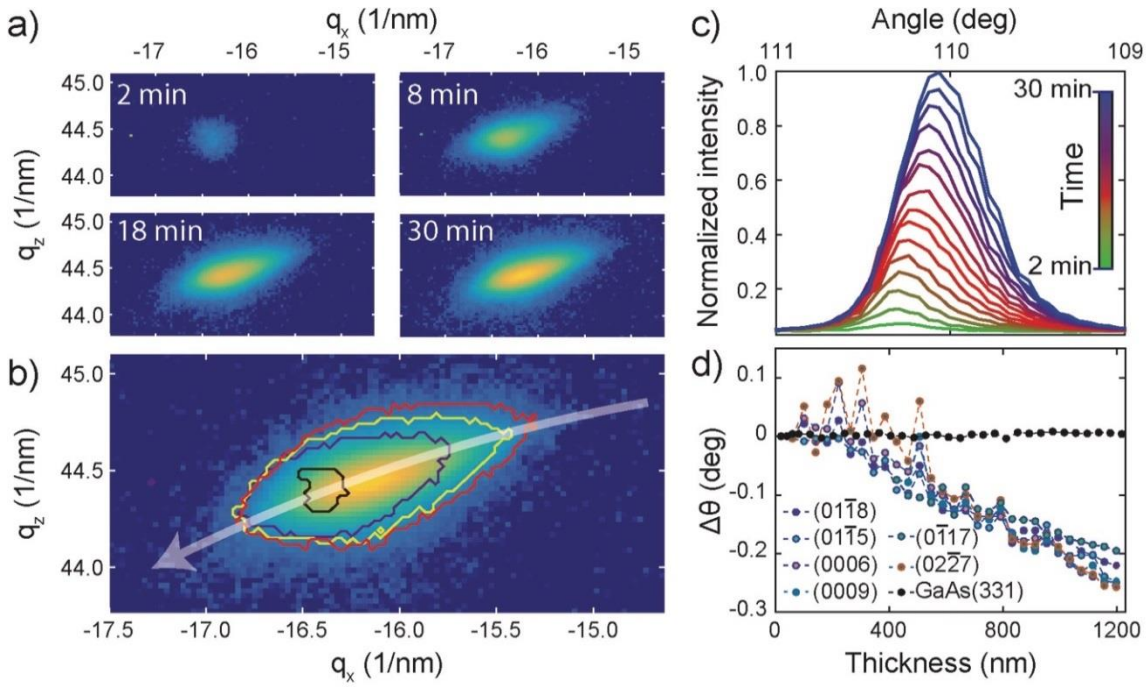

Figure A.5. (a) RSMs of the $(02\bar{2}7)_{Bi}$ diffraction from the $(0\,1\,\bar{1}\,8)$ domain at different time during the deposition. (b) Overlap of the contours of $(02\bar{2}7)_{Bi}$ diffraction at different time onto its final RSM. (c) Angular Intensity profile (as depicted at white arrow in (b)) of the $(02\bar{2}7)_{Bi}$ diffraction as a function of the deposition time. (d) Shift of angular position of the diffractions of the $(0\,1\,\bar{1}\,8)$ domain, compared with the substrate diffraction $(331)_{GaAs}$ as the function of thickness.

A.4 Evolution of the asymmetric tilt in Bi film during the growth

As mentioned previously in the experimental setup, we used 30 keV X-rays and aligned the asymmetric tilt axis $[2\bar{1}\bar{1}0]_{Bi}$ of $(0\,1\,\bar{1}\,8)$ domain with the incident X-ray wavevector. The purpose of this setup is to observe the asymmetric tilt and its evolution during the deposition. As shown in Figure A.2b, multiple diffraction peaks from $(0\,1\,\bar{1}\,8)$ domains are observed simultaneously (green indexes in Figure A.2b),

and, more importantly, all these diffraction peaks lie in the $(0K\bar{K}L)$ reciprocal lattice plane. Because the $(0K\bar{K}L)$ plane is perpendicular to the asymmetric tilt axis, if the asymmetric tilt angle about $[2\bar{1}\bar{1}0]_{Bi}$ varies during the deposition, a unique phenomenon would appear: all these diffraction peaks from bismuth $(0\ 1\ \bar{1}\ 8)$ domains will rotate in the same direction, by the same value, while the diffraction peaks from the substrate remain unaltered. For simplicity, the analysis was performed only for η=240 mV, where $(0\ 1\ \bar{1}\ 8)$ domains dominate and the mosaicity is a minimum. All the $(0\ 1\ \bar{1}\ 8)$ diffraction peaks exhibit a continuous rotation during the deposition. As representative example, in Figure A.5a, we show the reciprocal space map (RSM) in the proximity of the $(02\bar{2}7)_{Bi}$ diffraction peak as a function of deposition time. Plotting the contours of $(02\bar{2}7)_{Bi}$ the diffraction peaks obtained at different deposition times, as shown in Figure A.5b, it is clear that the radial position does not change (resolution $\approx 3 \times 10^{-3}\text{Å}^{-1}$), indicating that neither the interplanar distances nor the lattice parameters evolve as a function of thickness. Instead, the angular position continuously changes with deposition. Figure A.5c shows the intensity profile of the $(02\bar{2}7)$ diffraction peak along the trajectory of the $\{02\bar{2}7\}$ Debye-Scherrer ring during the deposition. The angular position of $(02\bar{2}7)$ diffraction peak varies by up to several tenths of degree during electrodeposition. Same procedure was applied to other diffraction peaks from the $(0\ 1\ \bar{1}\ 8)$ domains, as well as diffraction peaks from GaAs, to obtain the change of their angular position with the thickness of film, as shown in Figure A.5d. The film thickness is calculated from accumulated charge in the chronoamperometry. It is obvious that the angular position of the substrate, for instance $(331)_{GaAs}$ (The black dots in Figure A.5d), does not change. In contrast, the angular positions of all bismuth peaks show a monotonic dependence on the film thickness. For thickness less than 100 nm, the angular position does not change. Beginning at a threshold thickness lying between 100 and 200 nm, the angular

position of the bismuth peaks varies monotonically as a function of the film thickness. When the film thickness reaches 1.2 μm, the total shift of the Bi diffraction peaks is 0.23 °. This suggests the asymmetric tilt angle is constant only for thickness < 100 nm, and continuously relaxes beyond this range.

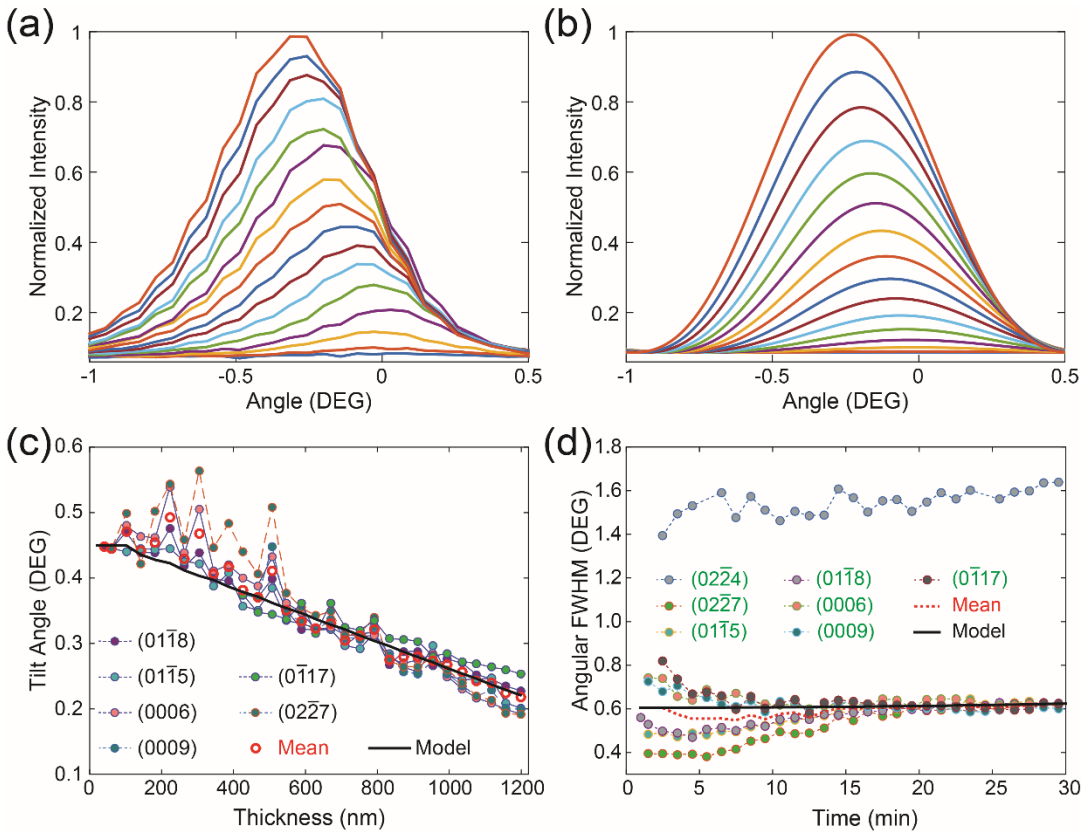

Figure A.6. (a) Angular Intensity profile of the $(01\bar{1}8)_{Bi}$ diffraction as a function of the deposition time. (b) Angular Intensity profile calculated from the model proposed in the main text. (c) The tilt angle of the diffractions from the $(0\,1\,\bar{1}\,8)$ domain, compared with the one calculated from the model. (d) Angular FWHM of diffractions from the $(0\,1\,\bar{1}\,8)$ domains, and compare with the one from the model.

The absolute value of the asymmetric tilt angle of bismuth film is calculated based on the difference of the crystallographic direction of $(0\ 1\ \bar{1}\ 8)$ and GaAs (110). Based on the asymmetric tilt model proposed in the reference only considering the lattice mismatch at the interface,[14,29] the tilt angle between the $(01\bar{1}8)_{Bi}$ and $(110)_{GaAs}$ planes should be 0.70 °. In our experiment, when the thickness of the film reaches 40 nm, the tilt angle is 0.45 °, 64% of the theoretical prediction. The angle decreases to 0.22 °, when the thickness reaches 1.2 μm. Our results suggest that the bismuth film relieves interface strain using tilt and, as the film grows, the tilt relaxes.

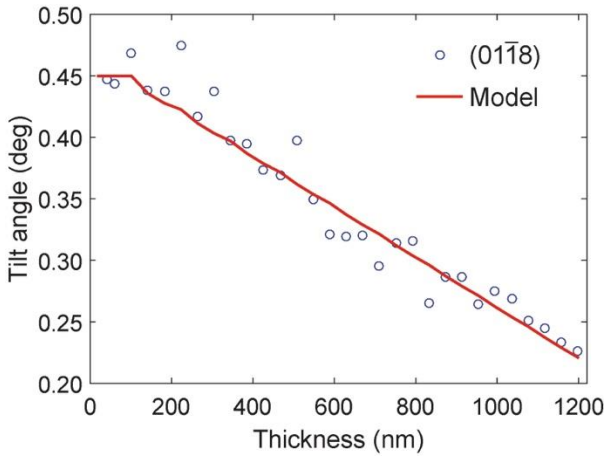

Figure A.7 The comparison between measured tilt angle from experiment and calculated one based on the model of forming low angle grain boundaries.

As shown in Figure A.5b, the peak shape at late times contains the peaks shapes obtained at earlier times, which can also be clearly seen from the intensity profiles in Figure A.5c. It suggests the decrease of the tilt angle is not caused by changing the orientation of the bismuth film that is already grown. Instead, the decrease in tilt angle is created by tuning the growth direction of bismuth back to $(01\bar{1}8)$. Microscopically, this could be realized by forming a series of low angle grain boundaries during the

film growth.[30] Using the Scherrer equation, the bismuth grain size is estimated to be about 120 nm along the surface normal. To test this hypothesis, a simplified model is proposed assuming the film is formed by equal-sized grains along the surface normal, and each grain has the same relative tilt angle $\Delta\theta$ with the neighbor. The diffraction pattern of this simple model is calculated and compared with the experimental result. Figure A.6a and b are the comparison between the experimental data of the intensity profile of $(01\bar{1}8)$ diffraction at different time and the one calculated from the model, when $\Delta\theta$ equals to 0.05° and the grain size equals to 120 nm. Under these conditions, the model exhibits the same threshold thickness and relaxation rate of the tilt angle as the experimental data, as shown in Figure A.6 and A.7. Moreover, the calculation shows that the formation of low angle grain boundaries does not influence the angular FWHM of the Bragg peak, which is consistent with the observation of constant angular FWHM of the diffraction peaks (see Figure A.6d). The driving force for the formation of the low angle grain boundaries may be the lower surface energy of the $(01\bar{1}8)$ surface. At the beginning of growth, the film is tilted to release the strain energy stored from the lattice mismatch between film and substrate. However, the side effect of this tilt is to change the surface plane of the film from $(0\,1\,\bar{1}\,8)$ to $(0\,1\,\bar{1}\,8+\Delta)$. The value of Δ is 0.2 with the initial tilt. The value of Δ for the topmost grain decreases to almost 0 after 30 min, tuning the surface plane to $(0\,1\,\bar{1}\,8)$. As demonstrated by Read and Shockley, the energy to form the low angle grain boundary becomes smaller as the relative tilt angle between grains decrease.[31] Thus, when the strain accumulates with the film growth and reaches the energy to form this low angle grain boundary, this asymmetric tilt starts relaxing. Considering the previous attempts to use this asymmetric tilt to grow strain free film, our work suggests that there exists a threshold thickness beyond which the film starts relaxing the tilt by forming a series of low angle grain boundaries along the surface normal.

A.5 Conclusions

In summary, using *in situ* XRD, we have studied the asymmetric crystallographic tilt of bismuth films during electrodeposition on GaAs(110) in real-time. By combining hard X-rays with an area detector, multiple diffraction peaks were monitored simultaneously. We found that the single crystallographic orientation $(01\bar{1}8)$ of the film can be selected by controlling the overpotential. From the angular position of the diffraction peaks from $(01\bar{1}8)$ domains, we measured the asymmetric tilt angle during deposition, and discovered that there is threshold thickness (around 120 nm) beyond which the film relaxes the tilt angle. To the best knowledge of the authors, the data in Figure A.5d is the first observation of the dynamical response of asymmetric tilt during growth.

REFERENCES

1 Koster, G., Huijben, M. & Rijnders, G. *Epitaxial Growth of Complex Metal Oxides*. (Elsevier Science, 2015).

2 Herman, M. A., Richter, W. & Sitter, H. *Epitaxy: Physical Principles and Technical Implementation*. (Springer Berlin Heidelberg, 2013).

3 Ghosh, T., Das, P., Chini, T. K., Ghosh, T. & Satpati, B. Tilt Boundary Induced Heteroepitaxy in Chemically Grown Dendritic Silver Nanostructures on Germanium and Their Optical Properties. *Phys. Chem. Chem. Phys.* **16**, 16730-16739, (2014).

4 Lo, C. F. & Sollie, R. Correlated Squeezed Phonon States. *Phys. Lett. A* **169**, 91-98, (1992).

5 Nagai, H. Structure of Vapor-Deposited $Ga_xIn_{1-x}As$ Crystals. *J. Appl. Phys.* **45**, 3789-3794, (1974).

6 Chupas, P. J., Chapman, K. W. & Lee, P. L. Applications of An Amorphous Silicon-Based Area Detector for High-Resolution, High-Sensitivity and Fast Time-Resolved Pair Distribution Function Measurements. *J. Appl. Crystallogr.* **40**, 463-470, (2007).

7 Dodson, B. W. Many-Body Surface Strain and Surface Reconstructions in Fcc Transition-Metals. *Phys. Rev. Lett.* **60**, 2288-2291, (1988).

8 Hirth, J. P., Pond, R. C., Hoagland, R. G., Liu, X. Y. & Wang, J. Interface Defects, Reference Spaces and the Frank–Bilby Equation. *Prog. Mater Sci.* **58**, 749-823, (2013).

9 Yamada, A. *et al.* Static Analysis of Off-axis Crystal Film Growth onto a Lattice-Mismatched Substrate. *Appl. Phys. Lett.* **79**, 608, (2001).

10 Hellman, E. S., Liliental-Weber, Z. & Buchanan, D. N. E. Epitaxial Growth and Orientation of GaN on (1 0 0) γ-LiAlO2. *MRS Internet J. Nitride Semicond. Res.* **2**, (2014).

11 Budai, J. D. *et al.* X-ray Microdiffraction Study of Growth Modes and Crystallographic Tilts in Oxide Films on Metal Substrates. *Nat. Mater.* **2**, 487-492, (2003).

12 Du, R. & Flynn, C. P. Asymmetric Coherent Tilt Boundaries Formed BY Molecular-Beam Epitaxy. *J. Phys. Condes. Matter* **2**, 1335-1341, (1990).

13 Huang, J. C. A., Du, R. R. & Flynn, C. P. Slip Requirements for Coherent Tilt of Hcp Epitaxial Crystals. *Phys. Rev. B* **44**, 4060-4063, (1991).

14 Huang, J. C. A., Du, R. R. & Flynn, C. P. Nucleation Processes in The Growth of HCP Titanium. *Phys. Rev. Lett.* **66**, 341-344, (1991).

15 Vereecken, P. M., Rodbell, K., Ji, C. & Searson, P. C. Electrodeposition of Bismuth Thin Films on N-GaAs (110). *Appl. Phys. Lett.* **86**, 121916, (2005).

16 Plaza, M., Abuin, M., Mascaraque, A., Gonzalez-Barrio, M. A. & Perez, L. Epitaxial Growth of Bi Ultra-Thin Films on GaAs by Electrodeposition. *Mater. Chem. Phys.* **134**, 523-530, (2012).

17 Yang, F. Y., Liu, K., Chien, C. L. & Searson, P. C. Large Magnetoresistance and Finite-Size Effects in Electrodeposited Single-Crystal Bi Thin Films. *Phys. Rev. Lett.* **82**, 3328-3331, (1999).

18 Mangez, J. H., Issi, J. P. & Heremans, J. Transport Properties of Bismuth in Quantizing Magnetic Fields. *Phys. Rev. B* **14**, 4381-4385, (1976).

19 Farhangfar, S. Quantum Size Effects in a One-Dimensional Semimetal. *Phys. Rev. B* **74**, 5, (2006).

20 Jiang, Q. & Wu, H. Magnetic Influence on Frequency of Soft-Phonon Mode in Incipient Ferroelectric $EuTiO_3$. *J. Appl. Phys.* **93**, 2121-2125, (2003).

21 Bao, Z. L. & Kavanagh, K. L. Epitaxial Bi/GaAs(111) Diodes via Electrodeposition. *Appl. Phys. Lett.* **88**, 022102, (2006).

22 Khvalkovskiy, A. V. *et al.* Matching Domain-Wall Configuration and spin-Orbit Torques for Efficient Domain-Wall Motion. *Phys. Rev. B* **87**, 020402, (2013).

23 Sánchez, J. C. R. *et al.* Spin-to-Charge Conversion using Rashba Coupling at the Interface between Non-Magnetic Materials. *Nat. Commun.* **4**, (2013).

24 Hirahara, T. *et al.* Large Surface-State Conductivity in Ultrathin Bi Films. *Appl. Phys. Lett.* **91**, 3, (2007).

25 Gustafson, J. *et al.* High-Energy Surface X-ray Diffraction for Fast Surface Structure Determination. *Science* **343**, 758-761, (2014).

26 Brauer, S. *et al.* In Situ X-ray Studies of Rapid Crystallization of Amorphous $NiZr_2$. *Phys. Rev. B: Condens. Matter Mater. Phys.* **45**, 7704-7715, (1992).

27 Sandnes, E., Williams, M. E., Bertocci, U., Vaudin, M. D. & Stafford, G. R. Electrodeposition of Bismuth from Nitric Acid Electrolyte. *Electrochim. Acta* **52**, 6221-6228, (2007).

28 Plaza, M. *et al.* Structure of the Photo-catalytically Active Surface of SrTiO3. *J. Am. Chem. Soc.* **138**, 7816-7819, (2016).

29 Krause, B. & Theis-Brohl, K. Surface Morphology and Structure of Epitaxial Yttrium on Niobium Buffer Layers with Different Orientations. *J. Phys. Condes. Matter* **12**, 4675-4686, (2000).

30 Gottstein, G. & Shvindlerman, L. S. *Grain Boundary Migration in Metals: Thermodynamics, Kinetics, Applications, Second Edition*. (CRC Press, 2011).

31 Read, W. T. & Shockley, W. Dislocation Models of Crystal Grain Boundaries. *Phys. Rev.* **78**, 275-289, (1950).